X-ray Studies
of the
Intermediate Polar PQ Gem

Cynthia Helen James

A thesis submitted to the University of London for the
degree of Master of Philosophy

Mullard Space Science Laboratory
Department of Space and Climate Physics
University College London

March 2001

Abstract

This thesis concerns an X-ray study of the intermediate polar (IP) magnetic cataclysmic variable (MCV) PQ Gem, which exhibits variable circular polarisation (indicative of a relatively high magnetic field) and a secure soft X-ray spectral component. These are unusual properties for an IP MCV. The scope of the thesis includes V405 Aur and RX J1712.6-2414, IPs which exhibit some of PQ Gem's unusual characteristics. This enables preliminary assessment of the generality of the PQ Gem's results.

The first three chapters are devoted to the introduction of the main characteristics and processes taking place in IPs, relevant previous findings about the three IPs under investigation and a description of the data, its reduction and analysis techniques employed. The focus of the analysis (Chapter 4) is to determine the role played by absorption and the changing visibility of the emission region(s) in forging the observed modulation of the light curves of PQ Gem over the spin period. It is concluded that both play a part. The phased-resolved spectroscopy shows a strong correspondence between the variation of the covering fraction of a partial absorber component and the hardness ratio. Possible accretion scenarios are examined and a modification of the accretion curtain model (Rosen et al. 1988) proposed. The mass of the white dwarf is also calculated. The analyses of V405 Aur and RX J1712.6-2414 (Chapters 5 & 6) resemble those of PQ Gem. The results are interpreted both in their own right and compared to those of PQ Gem. An explanation for the varying prominence of the double pulse in the spin folded light curves of V405 Aur is suggested.

The final chapter pulls together the results from the preceding chapters and makes a preliminary assessment as to the applicability of the findings on PQ Gem to the IP subclass of MCVs as a whole.

Contents

List of Tables

List of Figures

Chapter 1

Introducing Magnetic Cataclysmic Variables

1.1 So what are Cataclysmic Variables?

Cataclysmic variables (CVs) are close binary systems with relatively short orbital periods (generally, 3–6 hours). They are important in the study of accretion phenomena and accretion disc properties, as well as providing valuable information on the final stages of stellar evolution.

The primary star is a degenerate white dwarf, whereas the secondary is a low mass star on the lower main sequence. The usual spectroscopic classification for the secondary is a cool M-type (red dwarf) star, but other late type stars such as K-type or degenerate secondaries are also possible (Cropper et al. 1998a, Ramsay et al. 2000). Tidal effects due to gravitational and centrifugal forces distort the secondary from spherical to pear-drop shape and lead to its rotational synchronisation with the orbital period. This in turn mainly eliminates any initial eccentricity to give a circular orbit. The primary rotates asynchronously in the majority of CVs and is largely unaffected by distortion due to its compact nature. CVs are semi-detached systems (the secondary fills its Roche lobe, Section 1.2.1) which leads to stream accretion onto the primary via an accretion disc (for the majority of cases). This extends as far as the surface of the primary in those systems which have a low magnetic moment. However, a large magnetic moment in the primary can be sufficient to inhibit the formation of this disc and generate sufficient torque to ensure synchronisation (Section 1.2.2.1).

The magnetic CVs (MCVs) are those for which the magnetic moment is sufficient strong to substantially alter the accretion processes. The highest field MCVs (mainly the polars or AM Her systems) accrete directly from the stream onto the surface of the white dwarf. The lower field MCVs (the majority of intermediate polars (IPs)) possess a truncation to the inner boundary of the accretion disc, but the field is insufficient to inhibit disc formation completely.

Warner (1995) gives a comprehensive review of the several classes of CVs, many of which show a variety of eruptive behaviour.

1.2 The power source in Cataclysmic Variables

The power source in CVs is the conversion of gravitational potential energy to radiation through the transfer of mass from the secondary to the primary i.e. by stream accretion.

1.2.1 Accretion

The transfer of mass from the secondary to the primary is approximated to by Roche lobe geometry in which two objects depict Keplerian orbits around their common centre of mass due to their mutual gravitational attraction. The model assumes that these orbits are circular and that the objects are centrally condensed, i.e. they can be regarded dynamically as point sources. It then considers the behaviour of a test particle introduced into the system. The two objects are sufficiently massive that their orbits are unaffected by this test particle.

Two deep gravitational wells are centred on the point masses around which are equipotential surfaces. The shape of these surfaces depends on the mass ratio, but, in general, they are spherical at small radius and become elongated towards each

Figure 1.1: Roche equipotentials. The centres of the primary (1), secondary(2) and the centre of gravity (G) are shown for a mass ratio q=0.5. L_1 and L_2 are the inner and outer Lagrangian points respectively (Pringle 1985; Warner 1995).

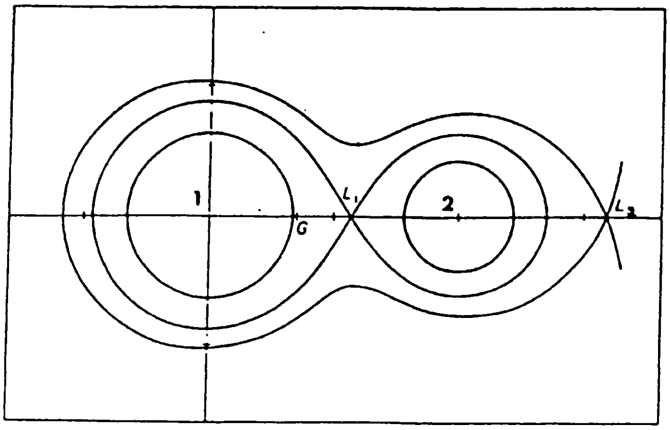

other at larger radii. The minimum equipotential to encompass both masses forms a critical surface with a saddle point, the inner Lagrangian point (L_1) separating two distorted spheres, the Roche lobes (Figure 1.1). It is easier for the test particle to pass to the other lobe through L_1 than to escape across the critical surface in general. Even so its path within the critical surface is dominated by the gravitational pull of the Roche lobe within which it is located (Frank, King & Raine 1992) .

This model forms a good approximation to the gravitational situation for CVs in which the secondary completely fills its Roche lobe. Any slight perturbation of the Roche lobe of the secondary in the vicinity of L_1 is sufficient to cause its material to pass into the Roche lobe of the primary. The stream flow makes an angle with the line of centres between the two stars due to the Coriolis effect and expands transversely at the speed of sound which allows the pressure to become negligible. The density distribution of the material within the stream is approximately Gaussian. The stream of gas particles issuing from L_1 possess considerable angular momentum and are accelerated from sonic to supersonic velocities with a ballistic trajectory which is governed by the Roche potential. This angular momentum is sufficient to ensure that the stream fails to accrete directly onto the primary, but circularises within the Roche lobe to impact on itself and thereby to form a ring of material (the distance of which, from the centre of the white dwarf, is termed the circularisation radius). Nevertheless, conservation of energy considerations ensure that the trajectory remains within the Roche lobe of the primary. The ring of material has finite extent and rotates differentially so that there is a distribution of energy loss caused by the dissipation of heat through viscous processes. Through arguments of the conservation of angular momentum, the ring of particles diffuses into a circular disc of material (Lubow & Shu 1975).

The stream impacts onto the outer rim of the established disc causing a shock heated area of complex structure due to the density distribution of the stream. This shocked area radiates strongly at optical wavelengths. The denser parts of the stream can penetrate the rim and/or overrun the surface of the disc giving rise to an extensive bulge on the outer rim and the possibility of further emission from a second impact site (Lubow & Shu 1975; Bath et al. 1983; Livio et al. 1986; Rozyzka & Schwarzenberg-Czerny 1987; Rozyzka 1988; Lubow 1989; Hirose et al. 1991; Lanzafame et al. 1992, 1993). The bulge region is thought to be the site associated with the S-wave seen in trailed optical spectra. In general there is an increase in temperature across the face of the disc toward the boundary layer at the interface between the disc and the primary. This boundary layer is a source of strong UV radiation. A further source of radiation is illumination of the concave faces of the disc (a property of thin steady state discs) by radiation from the primary and the boundary layer (Shakura & Sunyaev 1973; Frank, King & Raine 1992).

1.2.2 The Effect of a Strong Magnetic Field on Accretion

1.2.2.1 The Polar Picture

The magnetosphere is defined as that volume within which the magnetic field dominates the flow of mass, energy and angular momentum. The radius of the magnetosphere, r_μ, corresponds to the distance from the centre of the white dwarf to where the magnetic pressure is balanced by the ram pressure of the infalling material:

$$B^2/8\pi = \rho v^2$$

where $B^2/8\pi$ is the magnetic pressure, $\rho v^2 = (\dot{M}/\pi\sigma^2 v)v^2$ is the ram pressure of the material, σ is the radius of the stream, v is the velocity of the stream which is $\sim v_{ff}$, its freefall velocity (Mukai 1988). In polars this leads to a value for r_μ of $\sim$ few $\times 10^{10}$cm which is comparable to r_{L_1}, the distance to L_1 . Hence the magnetic field lines easily connect to those of the secondary, which leads to the synchronous rotation of the primary via various mechanisms (Warner 1995). It also leads to two different scenarios for the threading of material onto the magnetic field lines. If $r_\mu \geq r_{L_1}$ then the gas, which will be at least partially ionised due to irradiation from the primary, can follow the magnetic field lines for all interstar trajectories (e.g. Schneider & Young 1980a,b). However, the stream may penetrate for a long distance before threading occurs, if r_{L_1} is not included within any closed magnetic field lines. On the other hand if $r_\mu \leq r_{L_1}$ the stream follows the same trajectory as for non-magnetic CVs until r_μ is reached (Liebert & Stockman 1985). Nevertheless the shape and density of the stream is controlled by the magnetic field from the location where the magnetic pressure exceeds the thermal pressure ($r > r_\mu$). This leads to fragmentation of the stream due to the competing processes of Rayleigh-Taylor and Kelvin-Helmholtz instabilities which causes a spread in azimuth for the threading region (Burnard et al. 1983; Liebert & Stockman, 1985; Hameury et al. 1986a; Lamb & Melia 1986, 1987, 1988). This spread dictates the footprint of the threaded magnetic field lines at the surface of the white dwarf, and hence, to the formation of accretion arcs (e.g. Mukai 1988). The manner in which the stream threads the field lines may lead to a correlation of fragment size and hence to a variation in physical conditions along the length of the accretion arcs (Figure 1.2 illustrates the case where there is a variation in the density of the accreting material along the accretion arc). Single or two pole accretion is dependant on the orientation of the magnetic field to the binary geometry (e.g. Ferrario et al. 1989).

A simplification of this concept is provided by the homogeneous accretion model (also known as the standard accretion column model) in which the accretion stream is depicted as having a circular cross-section with uniform density distribution (Hoshi 1973; Fabian et al. 1976; Masters et al. 1977; Lamb & Masters 1979). The material threads the magnetic field lines smoothly at a very narrow azimuth to impact the surface of the white dwarf with a circular footprint at the magnetic pole. A strong shock forms above this area due to the need for rapid adjustment in physical conditions between the material of the accretion stream which is travelling at supersonic speeds and that of the photosphere of the white dwarf, Figure 1.3.

Ahead of the shock, the ionised particles are heated by electron conduction in a precursor. Across the shock boundary there is a factor of four increase in the gas density accompanied by a similar decrease in velocity. The structure of the postshock region is shown in Figure 1.4. The height of the shock depends on the efficiency of the cooling mechanisms provided by bremsstrahlung emission from free electrons, cyclotron emission by semi-relativistic electrons spiralling around the magnetic field lines and Compton cooling through the scattering of the relatively lower energy pho-

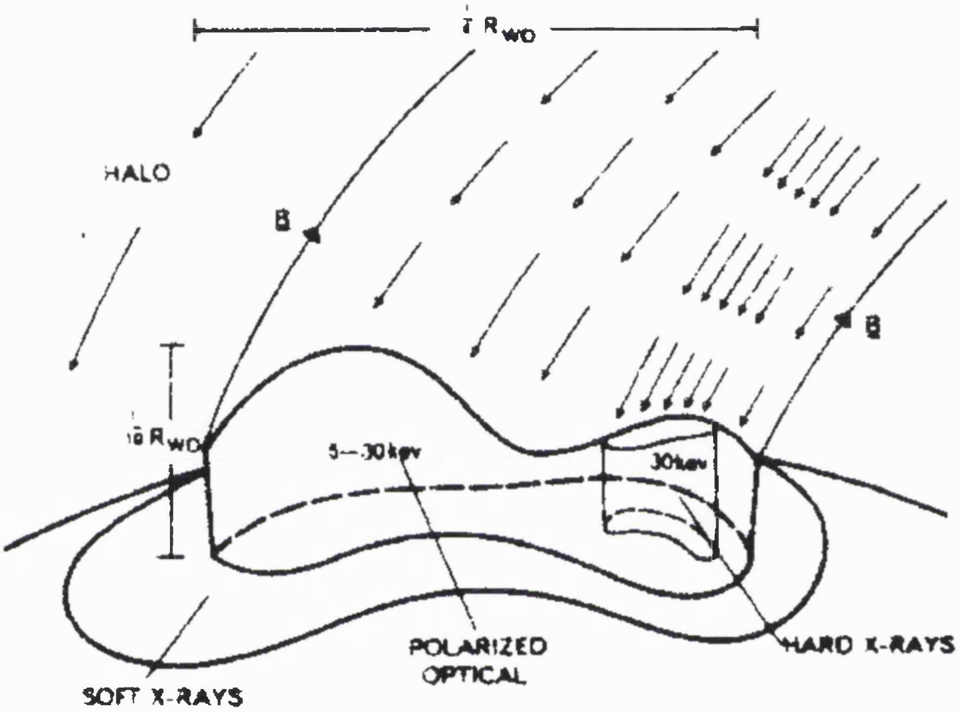

Figure 1.2: The structure of the accretion shock showing a high density compact region which is the source of the hard X-rays and a more extended lower density region which gives rise to the optical - IR polarised radiation. Reproduced from Wickramasinghe (1988).

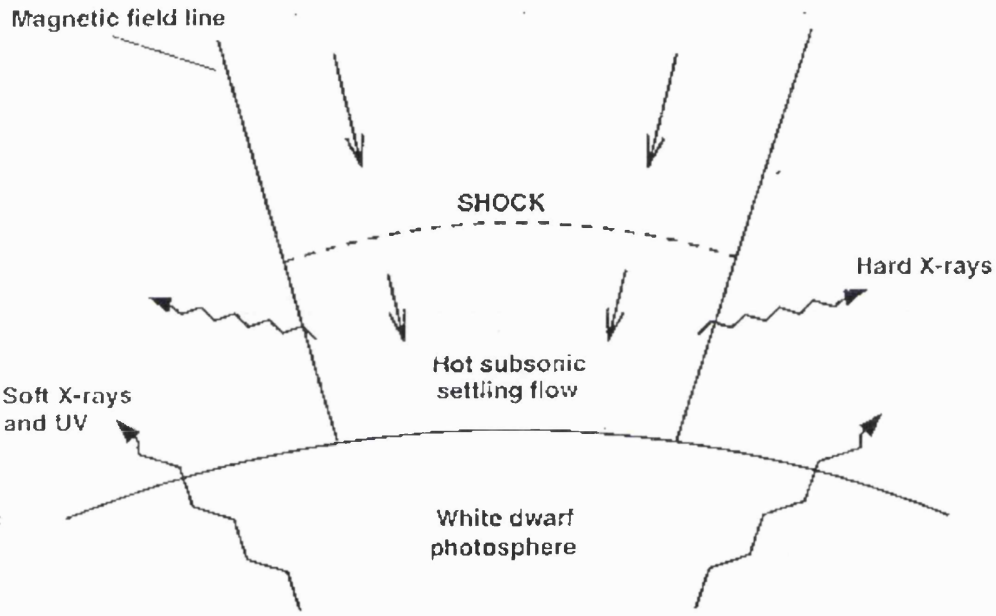

Figure 1.3: Schematic picture of a homogeneous accretion column taken from King (1995).

tons by shocked electrons. The relative importance of each of the cooling mechanisms depends on the postshock conditions, especially the magnetic field and the specific accretion rate. If bremsstrahlung cooling dominates, the ions and electrons are in equilibrium (single fluid case). On the other hand, if this equilibrium breaks down then cyclotron cooling dominates (two fluid case), which in extreme circumstances can cause the complete collapse of the shock (Masters 1978).

The spectrum is that of optically thin bremsstrahlung, (typically kT ~30keV), emitted from the accretion column; cyclotron emission, also emitted from the accretion column, which is optically thick for low harmonics, but optically thin at higher harmonics; and for reprocessed hard X-rays for that fraction which is intercepted by the surface of the white dwarf, such that those $\gtrsim$ 30keV are reflected with the remainder absorbed, thermalised and re-emitted as an approximate blackbody spectrum at UV and soft X-rays energies (usually $\simeq$40eV) (Milgrom & Salpeter 1975).

The symmetry associated with this model allows for simplification to a one-dimensional problem. Even so, a full computation requires solution of the three hydrodynamic equations of continuity, momentum conservation and energy conservation with appropriate boundary conditions (for a strong shock and a stellar photoshere temperature) including time-dependent terms (Cropper 1990). A static model for both the single and two fluid case, which takes into account bremsstrahlung, cyclotron and the reprocessed blackbody emissions, was calculated by Masters (1978). However it omitted consideration of radiation from the side of the column and assumed uniform temperature and density for the post shock region. Subsequently, the three hydrodynamic equations without the time dependent terms for the one-dimensional problem were calculated, e.g. by Imamura & Durisen (1983) (the single fluid case) and Imamura et al. (1987) (the two fluid case).

1.2.2.2 The IP Representation

Much of the accretion process in IPs is similar to that in polars, particularly with respect to the shock region. However, the braking torque from the magnetic field is insufficient to produce synchronisation. Hence, there are two distinct possible modes

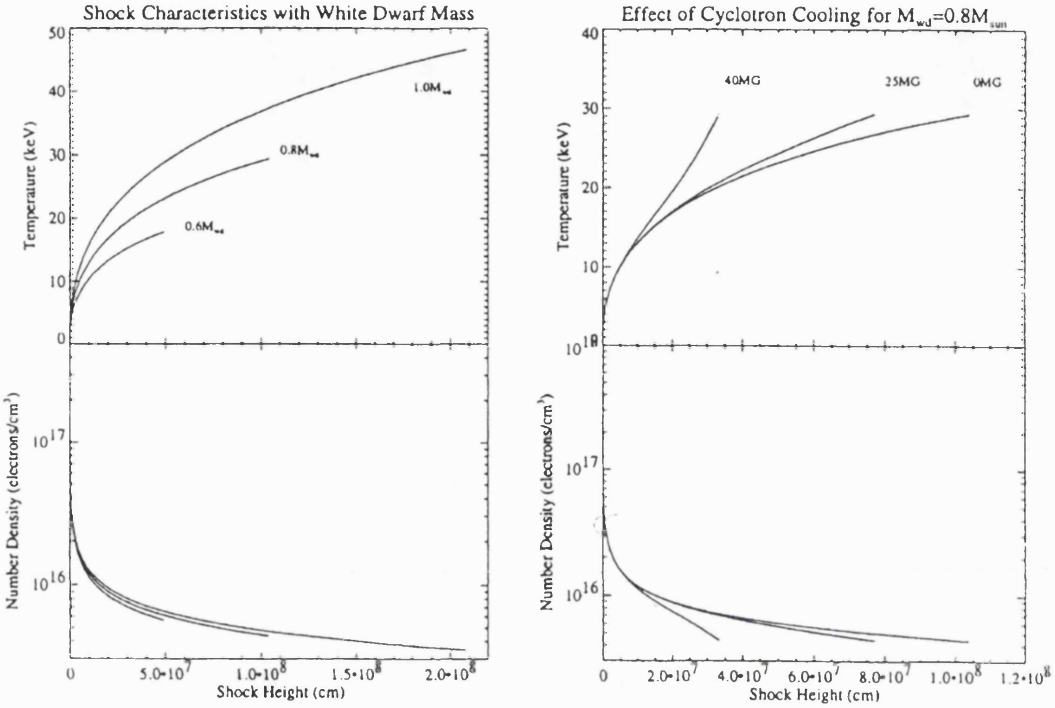

Figure 1.4: The left-hand figure shows the temperature and density profiles within the postshock flow for different mass white dwarfs accreting at 1g $s^{-1}cm^{-2}$ for a pure hydrogen plasma. The right-hand figure shows the dependence on shock height of the temperature and density profiles as a function of the magnetic field, for the same accretion rate and for a white dwarf of 0.8 $M_{\odot}$. Reproduced from figure 1, Cropper at al. 1999a.

of mass transfer depending on whether the magnetic moment is sufficiently low to allow the formation of a disc. A disc will certainly form if r_μ is less than the minimum radius depicted by the accreting particles around the primary and it will definitely not form if it is greater than than the circularisation radius (Section 1.2.1). However, the situation is very uncertain between these two extremes (Hameury et al. 1986b, Lamb & Melia 1986, 1987, 1988).

In general the magnetic axis is inclined to the spin axis which makes the asynchronous primary an oblique rotator. In other words, the accretion flow is time dependent, three dimensional and non-axisymmetric, which is a non-trivial problem, currently unsolved (e.g. Anzer & Börner 1980, 1983; Spriut & Taam 1990). The presence of a disc has profound effects on the magnetic field geometry. Convective and turbulent motions can be set up where the magnetosphere penetrates the disc, Kelvin-Hermholtz instabilities can arise at the interface between the flow within the disc and the magnetic field (Ghosh & Lamb 1978), and reconnection between the magnetic field of the primary and the disc can occur (Livio & Pringle 1992). These factors lead to a dilution of the primary's magnetic field in the midplane of the disc (Ghosh & Lamb 1979a,b) and to material and magnetic torques.

It is assumed that the disc in IPs lies in the orbital plane with the material threading onto the magnetic field lines over a range of azimuths at the onset of the magnetosphere. This situation was first modelled by Ghosh and Lamb (1978) for axisymmetric accretion, Figure 1.5, in which they predicted a narrow threading region. r_s depicts the inner limit to which the disc structure is unperturbed by the magnetic field. The co-rotation radius, r_A, is where the angular velocity of the primary and that of the disc match. r_0 marks the outer limit of the boundary layer, δ, over which the Keplerian flow in the disc is converted to a corotating flow through magnetic forces. Considerable shock heating can occur in this boundary layer if a large adjustment to the flow is required. It has been suggested that this region could be extended inward by fragmented 'blobs' of material (e.g. Arons & Lea 1980, Spruit & Taam 1990, 1993), similar to those postulated in polars. The magnetic field of the primary is able to thread the disc upto the limit r_s, due to the various dilution factors (see above) which reduce its strength in the midplane, but viscous stresses dominate in this outer transition zone of the disc. In the non-axisymmetric model it is assumed that the material accretes preferentially to the nearest magnetic pole in a time dependent manner. In this way material from the inner edge of the disc may form curtains of accreting gas to first one and then the other magnetic pole over the spin cycle (Rosen, Mason & Cordova 1988), Figure 1.6 bottom.

Discless accretion in IPs is expected to be similar to that of polars except that the material accretes alternatively to one magnetic pole and then the other with a beat period (Wynn & King 1992, Figure 1.6 top). In such a scenario it is to be expected that the material impacts the white dwarf over a 360° longitude range and would lead to a lower specific accretion rate covering ~10% of the surface of the white dwarf (Warner 1995).

Disc-overflow is a hybrid mode between disc and stream fed accretion in which the latter flows over the disc to impact directly onto the surface of the primary. Even so, some small percentage of the accretion also takes place from the inner edge of the truncated accretion disc (King & Lasota 1991).

1.2.2.3 Cyclotron Modelling

The material in the postshock region of the accretion column is highly ionised and hence the electrons (and ions) depict a helical path due to the force exerted on them by the magnetic field. In consequence, the accelerated electrons emit cyclotron radiation at their gyration frequency of $\omega_o = eB/\gamma m_e c$ plus all harmonics of this fundamental frequency. The energy of the electron determines the frequency of the radiation and its distribution across the harmonics in such a manner that the radiation from a more energetic electron is biased towards the higher harmonics. The polarisation of the radiation varies between circular (the line of sight to is parallel to the magnetic field lines) and linear (the line of sight to is perpendicular to the magnetic field lines), so, in general it is elliptical. The intensity of the radiation varies with the magnetic field strength and the harmonic so that towards high harmonics it becomes increasingly anisotropic, until it is a narrow beam centred on the

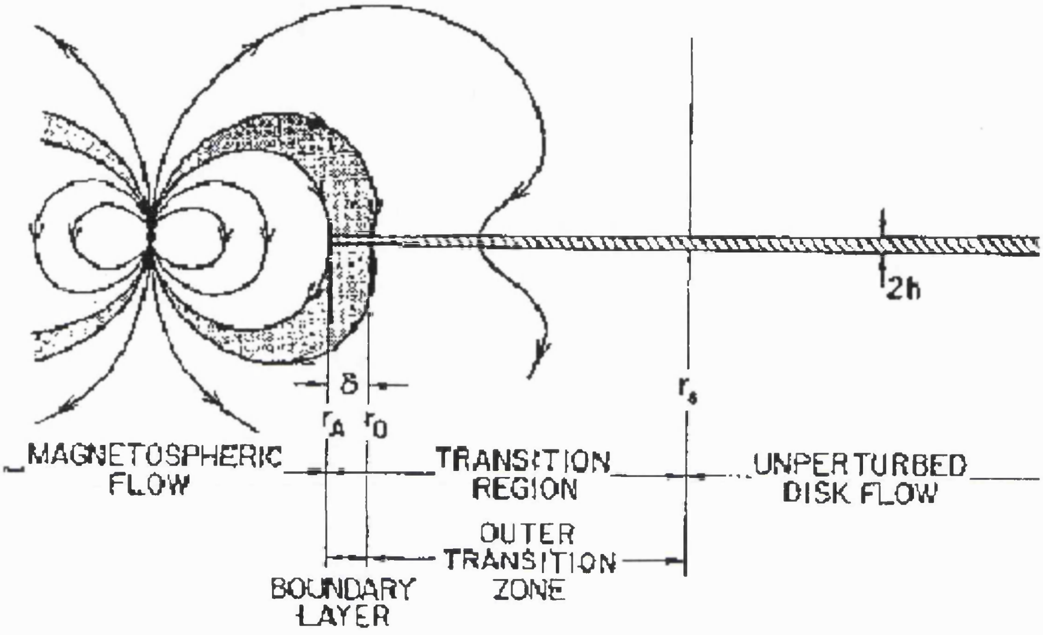

Figure 1.5: Schematic picture of disc accretion from an axisymmetric IP system taken from Ghosh & Lamb (1978). Beyond the radius, r_s, at which the stellar magnetic field is completely screened, the disc flow, of vertical thickness $2h$, is unperturbed by the magnetosphere. In the transition region between r_s and r_A the disc flow changes into magnetospheric flow. The transition region divides into two parts, an outer transition zone where viscous stresses dominate magnetic stresses, and a boundary layer of width $\delta \ll r_A$ where magnetic stresses dominate.

Figure 1.6: Schematics of the flow of material on to the white dwarf in an IP for discless accretion (top) and through an accretion curtain via an accretion disc (bottom). Reproduced from figure 1 of Ferrario (1996).

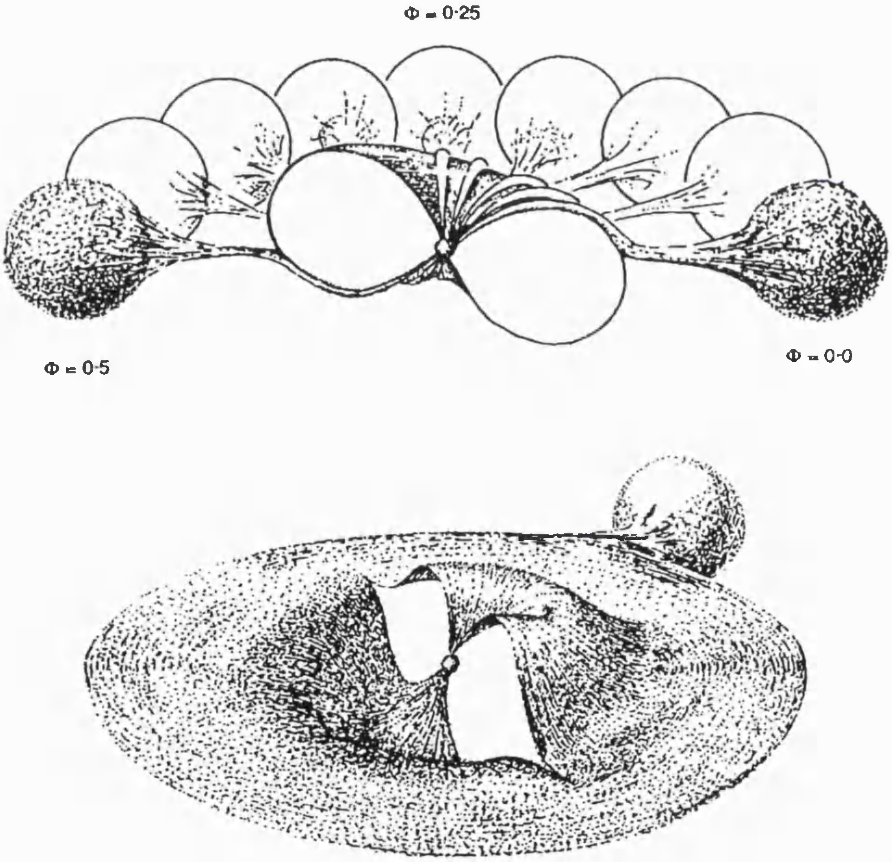

orbital plane of the electron. The observed cyclotron spectrum is created from an aggregate of electrons which possess a distribution of energies; this tends to broaden the spectrum preferentially towards the higher harmonics. The observed polarisation depends heavily on the viewing angle with respect to the magnetic field direction as well as on the effects of cyclotron opacity (decreases towards the higher harmonics) and free-free opacity (dominates where cyclotron opacity is low and as the viewing angle approaches zero). The cyclotron emission can be quantified by the Stokes parameters which are a mathematical formulation describing the radiation in terms of its intensity, percentage of circular and linear polarisation, and position angle of the linear polarisation.

The sensitivity of the observed polarised emission to the angle at which the magnetic field line is viewed makes it a very good probe for determining the structure of the postshock accretion region. Cyclotron modelling involves the use of polarisation data plus calculations of the transfer of radiation through an accretion column to model the structure of the accretion region.

Meggitt & Wickramasinghe (1982) and Wickramasinghe & Meggitt (1985) calculated the cyclotron emission from hot plasmas in terms of the electron temperature, frequency, the viewing angle with respect to the magnetic field, the electron number density (N_e), propagation path (s), and the optical depth parameter characterized by $\Lambda = 1.0 \times 10^5 (s/10^6)(N_e/10^{16}\ \mathrm{cm}^{-3})(1.8 \times 10^7 \mathrm{G}/B)$ where B is the polar magnetic field strength. Their calculations included allowance for both cyclotron and free-free opacities and were published as a grid of results for a range of values covering a large region of the parameter space.

In this thesis extensive reference is made to the cyclotron modelling of Potter et al. (1997). They used a dipole magnetic field formalism (Cropper 1989), and the results from Meggitt & Wickramasinghe (1982) and Wickramasinghe & Meggitt (1985) to derive the Stokes parameters for each emission point (at a given longitude and latitude on the surface white dwarf) for different phases of the spin cycle. The system was inclined by angle i to the viewer and the dipole was offset by an angle β to the spin axis of the white dwarf (Figure 1.7). A full radiative transfer through the

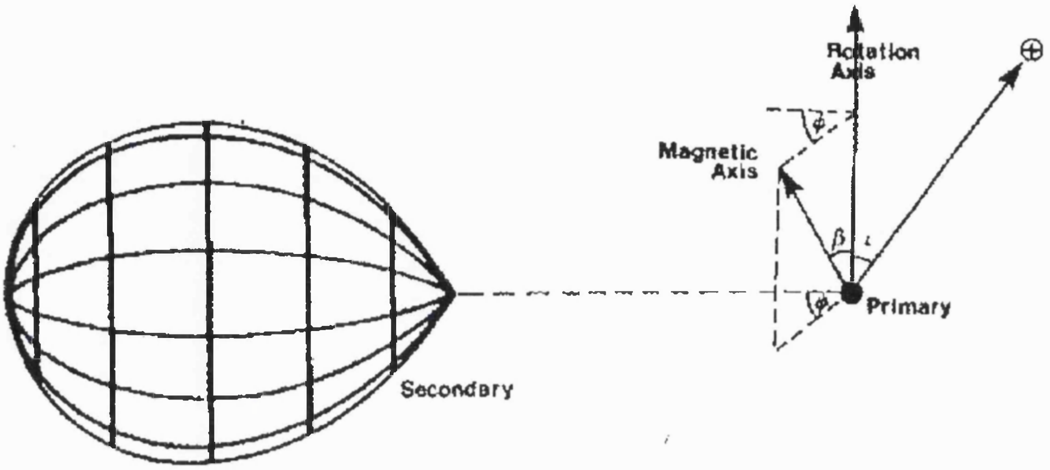

Figure 1.7: Schematic of an MCV showing i, the angle of inclination (the angle between the rotation axis and the line of sight), $\oplus$; β, the offset angle of the magnetic dipole-axis from the spin axis; ψ, the angle between the line of centres of the stellar components and the projection of the magnetic axis on the orbital plane. Reproduced from Cropper (1988).

shock was not carried out, but allowance for absorption along the shock was made by a first order approximation using a $\cos\theta$ term. The electron temperature, electron number density and the radial thickness of the emission region above the surface of the white dwarf were all kept constant during the modelling. However, locally the value of B (for a specific polar field strength) does vary and hence so did that of Λ. The best fit of the simulated data at all wavebands to the observed data was used to ascertain i and β, as well as the extent and location of the accretion regions on the surface of the white dwarf. The modelling also provided an estimate of the polar magnetic field strength.

1.3 The Properties of Intermediate Polars

The defining features of an IP are firstly that it is a strong emitter of hard X-rays and secondly that it shows multiple periods (Warner 1995). This latter property is the direct result of the asynchronous rotation of the primary with respect to the orbital cycle. These objects owe their name to their magnetic field strength which lies in a range between that of the non-MCVs and the strongly magnetic polars. As already stated in Section 1.2.2.2, the strength of the magnetic moment of in the majority of IPs (in contrast to that of the polars, Section 1.2.2.1) is not only insufficient to force the synchronisation of the primary but also to inhibit the circularisation of the accretion stream. Hence the majority of IPs accrete via a truncated accretion disc. These characteristics profoundly affect their behaviour making them observationally quite distinct from both the non-MCVs and the polars. Figure 1.8 is a schematic of an IP system showing the secondary, the accretion (mass transfer) stream, the bulge where this latter impacts on the outer edge of the accretion disc and the magnetic white dwarf. The system geometry of MCVs in general is shown in Figure 1.7.

1.3.1 Fundamental properties

The magnetic field strength, B, of most IPs is thought to be $\leq$ 2MG (Warner 1995), but some are considerably higher ($\leq$ 21MG). Although the majority of IPs are disc accretors, the evidence points to discless accretion for J1712.6-2414 (Buckley et al. 1997) and possibly TX Col (Hellier 1991). However, the latter, together with FO Aqr, may be examples of the hybrid accretion model in which the stream overflows the disc (Section 1.2.2.2).

The non-magnetic CVs show a significantly lower space density of systems with an orbital period between 2.2–2.8 hours; this interval is known as the period gap. EX Hya has the shortest orbital period at 1.633 hours and is one of only two IPs positioned below this period gap. The longest orbital period of any IP is that of GK Per at 47.923hr. The rotation rate of white dwarf varies from the very rapid 33.08s for AE Aqr to 4021.61s for EX Hya with a mean of 1143.49s (Warner 1995).

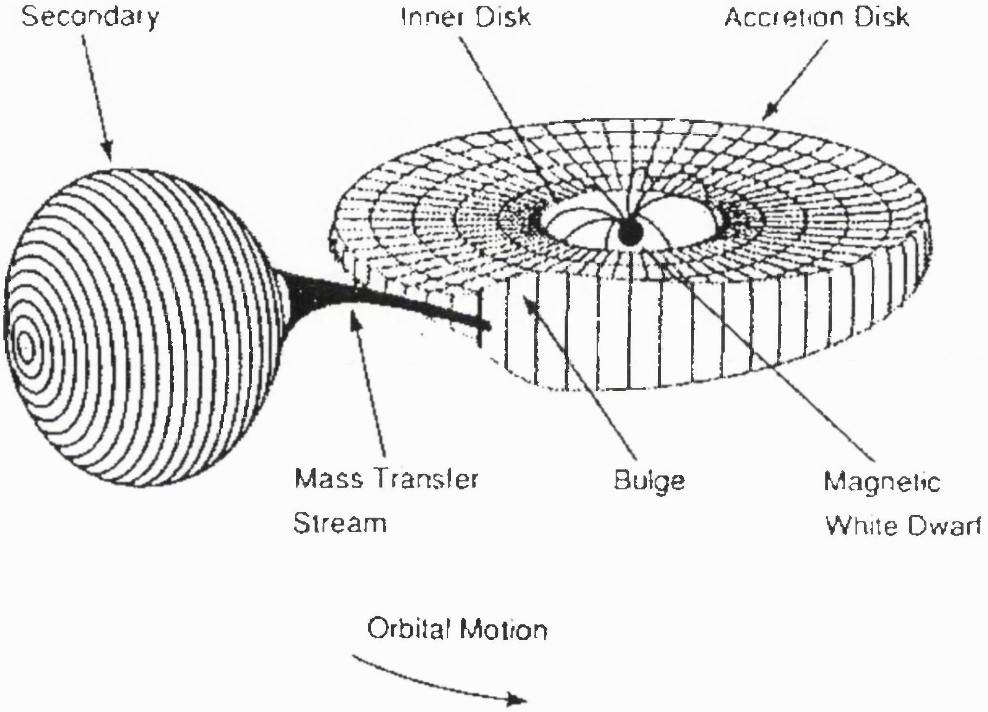

Figure 1.8: Schematic of an IP CV in which the magnetic white dwarf accretes matter from a truncated disc. Reproduced from Mason et al. 1988.

1.3.1.1 The Mass of the White Dwarf

It can be argued that the mass of the primary is the most important fundamental property of CVs, because so many of the physical processes taking place in these systems depend on this parameter. Equally, it is probably the most difficult for which to obtain an accurate estimate. Methods applicable to CVs in general require three measurements for the calculations: the radial velocities of both the secondary and primary stars, the orbital period and the inclination of the system to the line of sight. Accurate measurements are required of the last two quantities, but, in general, the angle of inclination, i (Figure 1.7), is only available in eclipsing systems, though relatively accurate measurements of i can be obtained from optical polarimetry for strongly magnetic CVs. Magnetic systems also offer the option to measure the mass of the primary from the radial free fall of gas onto the white dwarf through magnetically controlled accretion. This has been done using data from the *Ginga* satellite with code of varying levels of sophistication. Ishida (1991) deduced the mass from the spectral temperature using the X-ray continuum. This is a measure of the average temperature of the whole post-shock region rather than the higher temperature of the shock itself. Hence this estimate should be regarded as a lower limit. Wu et al. (1995) recognised the shortcoming in Ishida's method and used a closed form analytical solution (Wu et al. 1994) to improve upon his results. This readjustment neglected the density weighting and reflection from the surface of the white dwarf, caused by X-ray albedo, which leads to a further underestimation of the mass. This omission was addressed by Cropper et al. (1998b) in the first of a series of papers which used a stratified-accretion-column model, based on the closed integral solution of Wu et al. (1994), to fit the data with a temperature and density structure (Figure 1.4) which implicitly allow for bremsstrahlung and cyclotron cooling (Section 1.2.2.1). Further developments of their method changed the mean molecular mass, μ, from that of a pure hydrogen plasma to a cosmic plasma and made allowance for the gravitational variation within the shocked gas (Cropper et al. 1999b; Ramsay 2000). This final version of the model (using *RXTE* data) gives a range in the white dwarf mass from $0.45M_\odot$ for EX Hya to $1.20M_\odot$ for BG CMi with the mean of $0.85\pm0.21M_\odot$, where $M_\odot$ is the solar mass.

1.3.2 Light Curve Variations

Eruptive behaviour, such as that witnessed in many non-magnetic CVs is also observed in some IPs. In addition, IPs show large differences in the proportion of time spent in states of higher and/or lower output than normal, as well as in their general short-term variability.

1.3.2.1 X-rays

Those IPs having observational data of sufficient duration show modulation on the orbital period. The amplitude of the modulation increases towards the lower energies thus indicating that the cause is most probably due to photo-electric absorption by obscuring gas (Hellier et al. 1993).

Most IPs emit strongly in the hard X-ray band (2–20keV). In general, these light curves, folded on the spin period, are sinusoidal in profile, but overlaid with energy dependant dips (Warner 1995).

1.3.2.2 Polarised Light

The source of polarised light in MCVs is highly directional cyclotron radiation which is emitted from the accretion region due to the presence of a strong magnetic field (Section 1.2.2.1, 1.2.2.3). Its importance in determining the characteristics of these systems is mainly as a probe of the structure of the accretion region, as well as an estimator of the magnetic field strength and the angle of inclination through cyclotron modelling (Section 1.2.2.3). Polarisation has been observed in four IPs, three of which (PQ Gem, V405 Aur and RX1712.6-24) are the topics of the next chapter where their polarimetric properties will be discussed. The remaining member of the quartet, BG CMi, shows unmodulated circular polarisation at the $-4.24\pm$ 1.78% in the H band and -1.74 ± 0.26% in the J band with lesser levels in the optical and I bands (West et al. 1987).

1.3.3 X-ray Spectrometry

The majority of IPs have a much higher accretion rate than polars which leads to a hard X-ray luminosity (6×10^{31} erg s^{-1}–1×10^{33} erg s^{-1} for 2–10keV) which is greater than that of polars by a factor of 10–100 (Warner 1995). Successful model fitting usually requires an optically thin plasma component with a kT of $\gtrsim$ 30keV, a cold inhomogeneous absorber component and a component to model the Fe Kα line at 6.4–6.5keV. The upper limit of the temperature is often poorly constrained which may depend on the limited energy range covered by the detectors used, but complex absorption factors can also play a part (e.g. Duck et al. 1994). The equivalent neutral hydrogen column density (7×10^{20}cm^{-2}–25×10^{22}cm^{-2}) can vary by a factor of two around the orbit (Warner 1995).

Unlike polars the majority of IPs do not show a strong soft component (Watson 1986; Osborne 1988). However, the observed variation in the amplitude of the modulation in the optical light curves from one cycle to the next is indicative of inhomogeneous accretion at a level reminiscent to that seen in polars. Hence, the generation of EUV and soft X-rays by similar processes to those appropriated to IPs is to be expected; i.e. the reprocessing of hard X-rays (Section 1.2.2.1) and the thermalisation of submerged 'blobs' of accreting material in the photosphere of the white dwarf (Kuijpers & Pringle 1982). Their apparent absence may be due obscuration by local and interstellar absorption (Warner 1995).

1.3.4 Light Curve Modulation Scenarios

The early model of King & Shaviv (1984) for IPs invoked an oblique rotator in which the accretion footprint, located over the magnetic polecap, covered a large area ($f \gtrsim 0.25$) of the white dwarf surface. The varying visibility of the emission regions as the white dwarf rotated on its spin axis was mooted as the cause of the observed modulation for energies $\gtrsim$3keV. They considered the radiation in this energy regime to be very transparent with electron scattering the only likely source of opacity. Importantly, in this model, the minimum of the light curve modulation occurs when the emission site is pointing away from the observer and the accretion footprint covers a substantial fraction of the surface of the white dwarf.

At this time it was thought that IPs were the progenitors of polars and would evolve to polars with synchronisation of the white dwarf. Hence, the magnetic fields of the two populations must be similar, as it was difficult to propose a known physical mechanism by which they could subsequently acquire such a property. Starting from this premise, Hameury et al. (1986b) concluded that the formation of an accretion disc, in IPs with an orbital period <5hrs, was unlikely. They visualised the accretion stream impacting the rotating surface of the white dwarf like a jet from a hosepipe. Raleigh-Taylor and Kelvin-Helmholtz instabilities in the flow would lead to fragmentation into large and small blobs respectively. The accretion stream would intercept along the observers' line of sight at some orbital phases and its footprint would cover $\geq 10\%$ of the surface of the white dwarf. The expected signature for the modulation was an X-ray pulse lasting for less than half a spin cycle with profiles similar to those proposed by King & Shaviv (1984).

The oblique rotator accretion model (Section 1.2.2.2) lead Rosen et al. (1988) to propose the accretion curtain model in which the accreting material is threaded onto the magnetic field over a range of azimuths so that the footprint of these accreting field lines at the surface of the white dwarf is a narrow arc-shaped region. This description is synonymous with that of inhomogeneous accretion which also encompasses the possibility of variations in accretion rate across the accretion area. It is expected that such differences are accompanied by a variation in shock height which is minimized in those areas corresponding to the greatest accretion rate. In the upper hemisphere the curtain of material intervenes along the observer's line of sight as a function of rotational phase, and thus produces modulation of the X-ray flux at the white dwarf spin pulse. The model is a combination of self-occultation of the accretion regions combined with an optical depth effect due to photo-electric absorption and electron scattering. Maximum absorption occurs when the curtain is

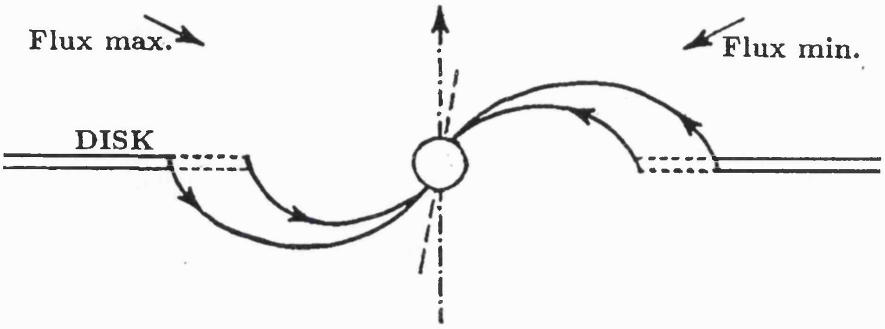

Figure 1.9: Schematic diagram showing a side view illustration of the accretion-curtain model of an IP. The maximum visibility of the emission region occurs when the upper pole points away from the observer (Flux max.), and the maximum attenuation of the radiation occurs when the upper pole points towards the observer(Flux min.). Reproduced from figure 13, Hellier et al. 1991.

viewed most nearly parallel to the direction of the magnetic field lines; i.e. when the upper hemisphere points towards the observer, Figure 1.9 (Flux min.). The visibility of the lower emission region happens 0.5 of a spin cycle later (assuming a symmetrical dipole geometry) when the absorption in the curtain is least, so that the maximum amplitude in the light curve occurs when the upper pole is pointing a way from the observer, Figure 1.9 (Flux max.). The emission region covers a small fraction of the surface of the primary in this scenario.

Rosen et al. (1988) also described what they termed a hybrid occultation/absorption model in which the emission region is located close to the surface of the white dwarf. In this case the symmetry of the emission regions must be broken in order for modulation to be observed. Heavy absorption of the emission region below the disc (e.g. by the inner edge of the accretion disc) can provide the required mechanism, since it attenuates the emission preferentially as the radiation energy decreases. In this model, the maximum amplitude of the light curve coincides with the emission region above the disc pointing most nearly towards the observer.

The weak magnetic field/fast rotator model was proposed by Allan et al.

(1996) in explanation of the observed double peak in the optical and *ROSAT* (0.1-05keV) light curves of the IP, V405 Aur. Subsequently, Norton et al. (1999) suggested that it equally applied to all IPs which have a relatively weak magnetic field, B, and a rapid rotation rate of the white dwarf. The lower B implies that the accreting material threads the magnetic field lines closer to the white dwarf; thus leading to an accretion region with a wider footprint than in those systems with a stronger B. If the width of the curtain is sufficiently large then the optical depth will be greater in the direction horizontal to the surface of the white dwarf rather than in the direction parallel to the magnetic field lines (as in the case of the accretion curtain model). A maximum in the emission pulse occurs when the observer views the system from direction A, Figure 1.10 (reproduced from Norton et al. (1999)); at which time the other emission area is occulted by the body of the white dwarf. A further emission maximum occurs 0.5 of the spin cycle later when the system is viewed from direction B (Figure 1.10).

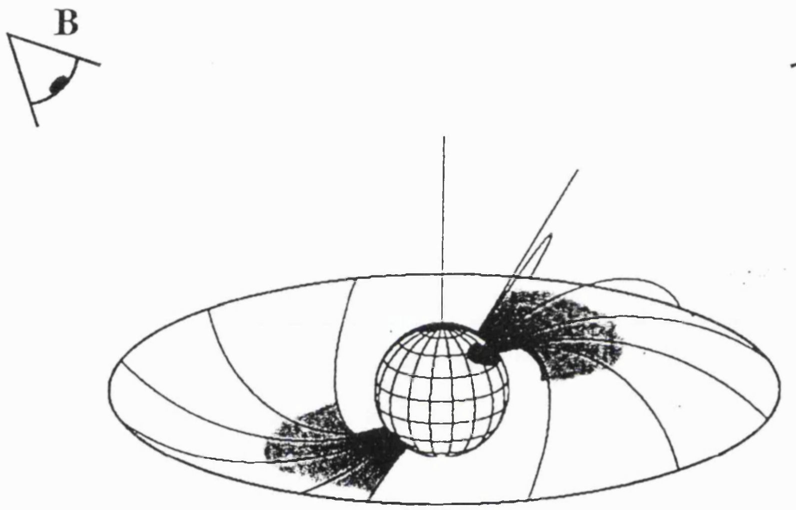

Figure 1.10: Schematic diagram showing an intermediate polar with a relatively low magnetic field. Attenuation of the X-rays is greatest parallel to the white dwarf surface (across the accretion curtains), and least along the magnetic field lines (up the accretion curtains). X-ray pulse maxima are seen when the system is viewed from both A and B. Reproduced from figure 8, Norton et al. (1999).

Chapter 2

The Participants

2.1 Introduction

PQ Gem is an IP which exhibits many unusual and intriguing properties for a MCV of this type. Two of the most notable of these characteristics are a unambiguous soft spectral component (more normally associated with the polars) and spin modulated circular polarisation. The latter implies a strong magnetic field and so, is also more usually associated with the polars. PQ Gem is the protagonist of this work, but by way of comparison, two other IPs which show some similarities to PQ Gem, V405 Aur and RX J1712.6-2414, are also covered. V405 Aur, like PQ Gem, shows a unambiguous soft component (Harberl et al. 1994), but its magnetic field strength is, in general, assumed to be low. On the other hand, RX J1712.6-2414 does not exhibit a soft spectral component, but does have the largest degree of circular polarisation observed in any IP (Buckley et al. 1995, 1997). Moreover, it is the only object of this class, apart from PQ Gem, in which periodic modulation of the polarised light is detected (Sections 1.3.2.2, 2.2.2.1).

2.2 PQ Gem or RE J0751+14

PQ Gem (RE J0751+14) is one of six IPs discovered by the *ROSAT* Galactic Plane Survey project (Haberl & Motch 1995). Its position (from the optical follow up) is RA (2000) $7^h\ 51^m\ 17.3^s$ Dec (2000) $+14^\circ\ 44'\ 23''$ (Mason et al. 1992).

PQ Gem has been classified as an IP due to the observational evidence for multiple periods and strong hard X-ray emission (Section 1.3). In addition to these characteristics it also shows unequivocal circular and linear polarisation in the infrared and R-band as well as strong EUV and soft X-ray spectral components. These properties are more usually associated with polars, which has lead to the proposition that PQ Gem is the first truly intermediate polar (Rosen et al. 1993). This section reviews those system parameters and properties which have a bearing, in some capacity, on the analysis carried out in Chapter 4.

2.2.1 System Parameters

2.2.1.1 The Mass of the Primary

The mass of PQ Gem's white dwarf has been calculated using several models based on the radial free fall of gas through magnetically controlled accretion (Section 1.3.1.1). The range of masses obtained and the relevant model parameters are given in Table 2.1. The majority of these estimates are comparable to those for other IPs derived from the same model, but high when compared to single white dwarfs (Cropper et al. 1998b). Further estimates of the mass are made in this work using the stratified-accretion-column (Section 1.3.1.1) model and data from the *ASCA* and *RXTE* satellites.

2.2.1.2 Distance

The distance estimates for PQ Gem show a wide range of values from 220 ±80 pc (Howell et al. 1997) to 3kpc (Mason 1997). Between these extremes there is the 280pc lower limit estimate of Mason (1997) and the 400pc value included in the review by Patterson (1994).

$M_{WD}(M_{\odot})$	model	Reference
1.29(>1.17)	C+G+PC+reflection	Cropper et al. (1999b)
1.21(>1.08)	C+G+IA+reflection	Cropper et al. (1999b)
1.32(>1.15)	C+IA+reflection	Cropper et al. (1999b)
1.39(>1.25)	H+IA+no reflection	Cropper et al. (1998b)
1.35(>1.05)	H+IA+reflection	Cropper et al. (1998b)
0.65	analytic solution (closed form)	Wu et al. (1995)
0.31	temp: X-ray continuum	Ishida (1991)

Table 2.1: Estimates of the mass of the white dwarf in PQ Gem using various models derived from the radial free fall of gas onto the white dwarf through magnetically controlled accretion (Section 1.3.1.1.). In all instances the data used was from the *Ginga* satellite. The errors (where provided) are to the 90% confidence level with a fixed upper limit of $1.4M_{\odot}$. The key to the parameters given in the model column are as follows: H signifies a mean molecular mass, μ, for a pure hydrogen plasma (0.5); for C, μ is representative of a cosmic plasma (0.615); G signifies that the code included allowance for gravitational variation within the shocked gas; IA is a warm partially ionised absorber (Section 3.3.2.2); and PC is a partially covering photo-electric absorber (Section 3.3.2.2).

2.2.1.3 Magnetic Field

The magnetic field, B, of PQ Gem has been estimated on three separate occasions using cyclotron modelling (Piirola et al. 1993, Potter et al. 1997, Howell et al. 1997, Section 1.2.2.3). Piirola et al. (1993) found that the observed polarised fluxes gave a best fit of B = 18MG when $\Lambda \sim 10^5$ and $kT \sim$ 10keV; and of B = 10MG when the model parameters were set at $\Lambda \sim 10^6$ and $kT \sim$ 20keV. Consideration of the calculations of Wickramasinghe et al. (1991) for ribbon-like accretion shocks lead them to their final estimate of 8–18MG. Potter et al. (1997) found that the optimal fit to their data with $\Lambda \sim 10^7$ and kT=10keV gave B = 14.0MG. However they obtained acceptable fits for the range B = 9–21MG, dependent on the initial values of Λ and T.

Väth et al. (1996) estimated the magnetic field strength by modelling the light curves taking into account the accretion shock structure, i.e. using similar principles as the calculation of the mass of the white dwarf (Section 1.3.1.1). They used a shock temperature of $kT \sim$ 20keV and assumed the structure of the upper and lower emission regions to be the same. They calculated B for a range of values for the mass of the white dwarf, M_{WD}, and accretion rate, $\dot{M}$, using the X-ray flux as constraint. They found that B = 9–21MG for a M_{WD} = 0.4–0.8$M_{\odot}$.

All three estimates give very similar ranges for the magnetic field strength. However, a higher value of M_{WD}, as indicated by Table 2.1, would result in a lower B with respect to the last estimate.

2.2.1.4 Periods

Investigations into observed photometric periods have been carried out by numerous authors from the hard X-ray to far infrared (Mason et al. 1992, Hellier et al. 1994, Duck et al. 1994, Potter et al. 1997, Piirola et al. 1993, Rosen et al. 1993, Stavroyiannopoulos et al. 1997, Hilditch et al. 1994). The spin period of 13.9 minutes has been observed in all energy bands; whereas, the beat period of 14.5 minutes has only been seen in the UV and UBV wavebands (Piirola et al. 1993, Rosen et al. 1993, Hellier et al. 1994, Potter et al. 1997, Stavroyiannopoulos et al. 1997).

Optical spectroscopy provides a rich source for system periodicities through the analysis of emission lines. PQ Gem has proved to be no exception in this respect. Radial velocity measurements gave an estimate of the orbital period at 5.18±0.01h (Mason 1995) which is very close to the implied photometric orbital period of 5.19h (Hellier et al. 1994).

An accurate ephemeris is an essential tool to all but the most elementary data analysis. It is only through its knowledge that direct comparisons can be made between the phasing of the light curves from different energy bands and different epochs. Mason (1997) addressed this problem for PQ Gem by including data from a five year period to develop a quadratic X-ray ephemeris. In the soft ($<$ 0.5keV) X-ray (*ROSAT*) light curves (Figure 2.1) there is a prominent dip with a very narrow core which varied by as little as 0.034 phase (30s) maximum per spin cycle from its mean position (Mason 1997). This notch can also be seen in the medium X-ray energy band ($\leq$6.0keV) of the *Ginga* data, Figure 2.1, at roughly the same phase, though its width is around twice that seen in the soft X-rays. Therefore, this dip was chosen as the fiducial marker. The X-ray ephemeris calculated from the *Ginga* data (Duck et al. 1994) were combined with "the dip" minimum from the *ROSAT* and *ASCA* data to give the following quadratic ephemeris (Mason 1997)

$$HJD_{X_{min}} = 2448173.95714(5) + 0.0096458718(10)N_{cyc} + 5.24(4) \times 10^{-13}N_{cyc}^2 \quad (2.1)$$

where N_{cyc} is the number of spin cycles and the numbers in parenthesis indicate the error in the last decimal places.

The evidence is that this quadratic X-ray ephemeris for the spin cycle is standing the test of time. Mason (1997) found it to be entirely consistent with prior optical ephemerides, while Hellier (1997) used I-band photometry data to confirm the necessity for a quadratic ephemeris.

The only orbital ephemeris, HJD = 2449333.984(4) + 0.216359(3)E was calculated from optical observations by Hellier (1997).

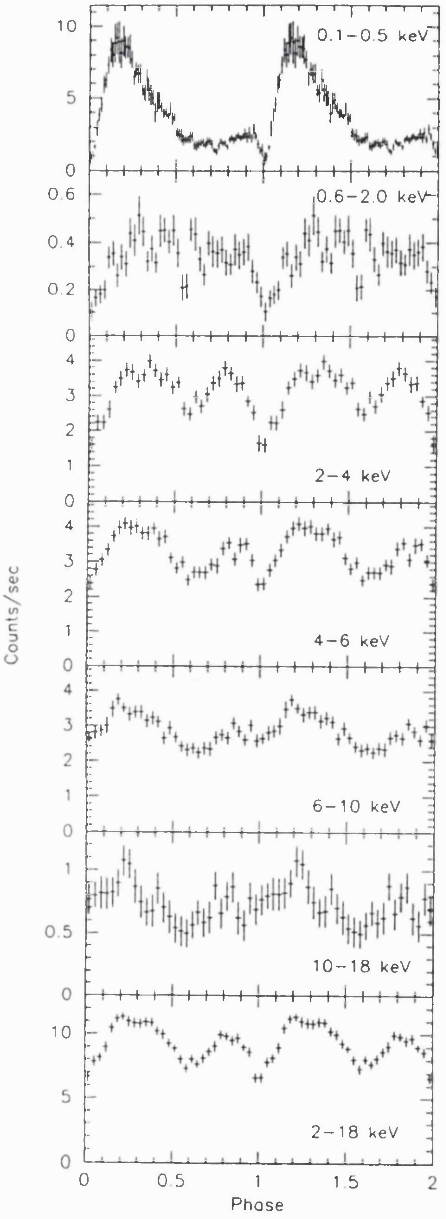

Figure 2.1: Phase-folded light curves for the 'soft' (0.1–0.5keV) and 'hard' (0.6–2.0keV) *ROSAT* PSPC spectral bands (top two panels); and five energy-resolved *Ginga* bands. Reproduced from figure 3, Duck et al. (1994).

The calculation of the quadratic spin ephemeris (Mason 1997) also provided the rate of change of the spin period, $\dot{P} = +1.1 \times 10^{-10}\mathrm{s\ s^{-1}}$ over the 5 years since 1990. The positive sign indicates that the spin period is lengthening; a finding that is endorsed by results from cyclotron modelling by Potter et al. (1997). V1223 Sge is the only other IP definitely found to be spinning down, though FO Aqr and V533 Her are borderline candidates. Period changes per se are not uncommon amongst IPs; even so, the magnitude of $P/\dot{P}$ in PQ Gem is almost twice that seen in any other IP. The I-band quadratic spin ephemeris of Hellier (1997) leads to a $P/\dot{P}$ of 2.5 × 10^5 yr which compares favourably to that of 2.4 × 10^5 yr found by Mason (1997).

2.2.1.5 Orientation

The system geometry and its presentation with respect to the line of sight of the observer is an important determinant in unravelling the observed physical phenomena. The crucial geometric parameters are the angle of inclination, i, and the offset angle of the magnetic axis from the spin axis, β (Figure 1.7). The most accurate estimates of i are provided by eclipsing systems. Nevertheless, in general, observational data can provide clues which lead to less accurate estimates.

Of the various alternative methods probably the most accurate is that of cyclotron modelling (Section 1.2.2.3). Piirola et al. (1993) measured $i = 45°–70°$ with two extended emission regions (located close to diametrically opposite magnetic poles) at $\sim$ 35°–60° from the rotational axis of the white dwarf. On the other hand, Potter et al. (1997) determined $i = 60°$ with $\beta = 30°$ (though Hellier (1997) finds that the spin-wave velocities point to $i \ll 60°$). Potter et al. (1997) associate the peak of the positive circular polarisation with phase 0.7; whereas, at phase 0.1–0.2 there is a reduction in the negative circular polarisation which, they suggest, is caused by depolarisation due to absorption. Hence, their model places the emission region in the upper hemisphere closest to the line of sight at phase 0.1–0.2. This is in the opposite sense to the model developed by Piirola et al. (1993) and which is upheld by the accretion region modelling of Vath (1996). Doppler tomograms on optical spectroscopy of emission lines provide still further support to this opposing orientation (Hellier 1997). Nevertheless, consideration of the changes in light curve modulation from the infrared to the hard X-rays indicate that the accretion region faces the observer at the phase of the maximum in the 10–20keV light curve, i.e. at phase 0.11 (Mason 1997).

2.2.2 The Light Curves

There is a remarkable constancy in PQ Gem's light curves as observed from one epoch to another, though there is considerable variation in the amplitude of the modulations from one cycle to the next. PQ Gem has not as yet shown evidence for high/low states or for outbursts such as those which characterize many other IPs and CVs in general (Section 1.3.2). This long term stability is not carried through into the results from polarimetry where there is considerable difference from one observation to the next.

2.2.2.1 X-ray

The soft *ROSAT* PSPC (0.1–0.5keV) light curve folded on the spin period (with "the dip" as fiducial marker) shows a high amplitude modulation (Figure 2.1) with the maximum estimated to occur at phase 0.19±0.05 and the width of "the dip" to be 0.09±0.03 (Duck et al. 1994). In the hard *ROSAT* PSPC (0.6–2keV) light curve, folded on the spin period, the width of "the dip" is 0.12±0.05 cycles (Figure 2.1).

The *Ginga* 2–4keV, 4–6keV, 6–10keV and 10–18 keV spin folded light curves are double-peaked with the possible exception of that for the 10–18 keV passband (Figure 2.1). The profile of the modulation decomposes into a broadly sinusoidal variation which is increasingly cut into by "the dip" as the energy decreases. The phasing of "the dip" is consistent across the wave-bands, but the depth is strongly energy dependent. The flux maximum occurs at phase 0.11±0.03. (Duck et al. 1994).

2.2.2.2 Polarised Light

Variable circular polarisation exhibiting both positive and negative signs which peaked at phases ~0.6 and ~0.4 respectively were detected by Potter et al. (1997) for the *V* through to *K* bands. The maximum amplitude occurred in the I- and J- bands at a level of ~2%. Previously, variable circular polarisation had been detected in the *R*-band (Rosen et al. 1993, Piirola et al. 1993) and in the *I*-band (Piirola et al. 1993). The results from the cyclotron modelling by Potter et al. (1997) demonstrated accretion arcs of equal size positioned diametrically opposite, but ahead of the poles. The arcs extended in magnetic longitude from 60°–200° with an elongation of 20° towards the magnetic equator. In magnetic latitude they extended from 12°(longitude 60°)–32° (longitude 200°). The orientation and phasing of these arcs within the spatial reference frame of the white dwarf is shown in Figure 2.2 (reproduced from Potter et al. 1997, figure 9).

Howell et al. (1997) used the same model with minor adjustments to analyse their polarimetry data. They needed to introduce asymmetric arcs and extend them by longitude 20° and latitude 30° to obtain good fits between the calculated and observed data. They were unable to resolve the discrepancy between the model's position angle range of 180° and their data which exhibited a position angle between 50°–60°.

Linear polarisation varying between -80° and +90° in both the I- and R- bands was detected by Piirola et al. (1993) which indicated that at least some polarisation emanated from within the system.

2.2.3 X-ray Spectroscopy

The most extensive X-ray spectral analysis of PQ Gem to date was carried out by Duck et al. (1994) using data from both the *ROSAT* and *Ginga* satellites. Their analyses included spin phase-resolved spectroscopy with the spectrum partitioned into 4 bins; the primary maximum (phase 0.09–0.49), the minimum (phase 0.49–0.71), the secondary maximum (phase 0.71–0.915) and the "dip" (phase 0.915–0.09).

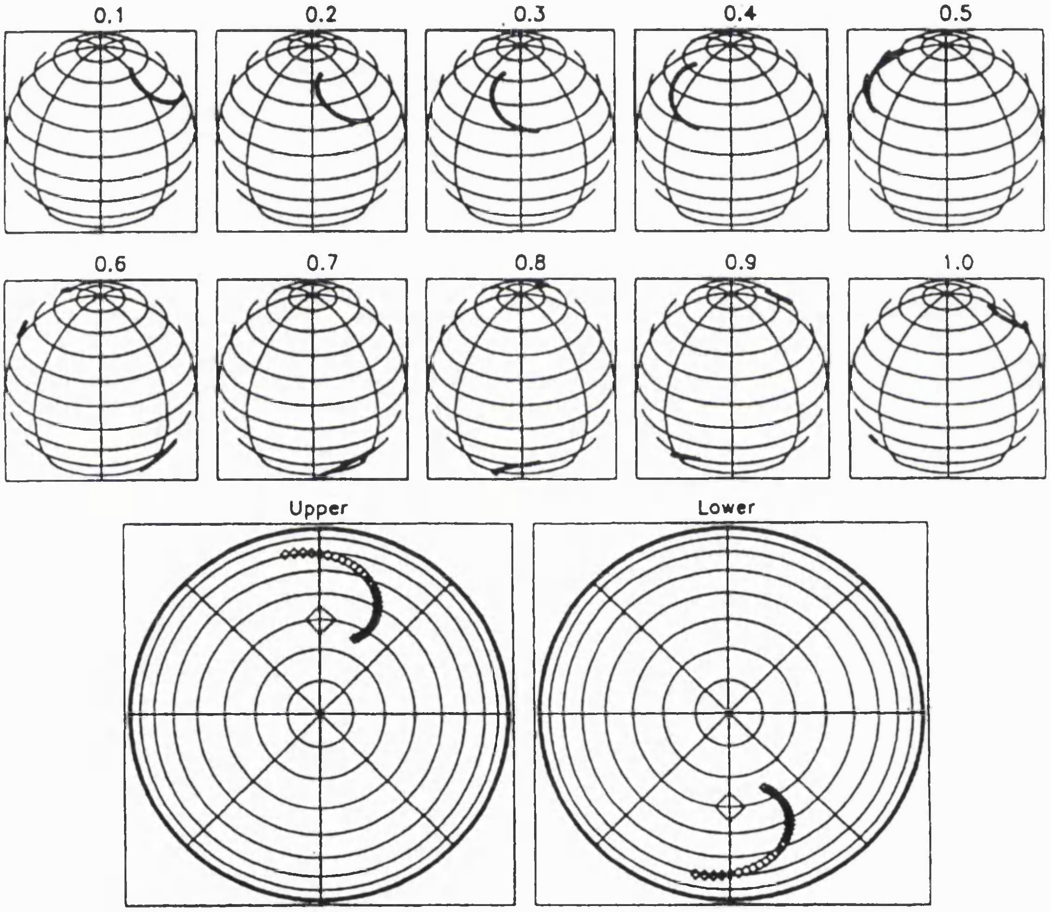

Figure 2.2: Illustration of the upper and lower accretion arcs on the surface of the white dwarf as computed from cyclotron modelling of PQ Gem (Section 2.2.2.2) at consecutive phases of the spin period. The bottom two globes give the view as seen from directly above the top and bottom poles respectively. The diamonds mark the magnetic poles. Reproduced from figure 9 of Potter et al. (1997).

Model fitting separately to the *ROSAT* (0.1–2.5 keV) data showed it to be dominated by a powerful soft component of blackbody temperature 20–60eV. This confirmed the results of Mason et al. (1992) who found an S1/S2 ratio of > 3.2 (90% confidence) indicating a soft source spectrum cut off by absorption. Nevertheless, there is no evidence for a soft excess, since the $L_{BB}/(L_{bremss} + L_{cycl}) \sim 0.55$ which is consistent with the spectral distribution of PQ Gem (Mason 1995).

It was not possible to constrain the upper limit to the temperature of the *Ginga* data during the spectral fitting, therefore they fixed it at 20.0keV. This temperature was identified during a separate model fitting exercise by restricting the spectrum to >10keV thus eliminating those energies most effected by absorption.

The spin phase-resolved spectroscopy demonstrated that the maximum emission from both the blackbody and the thermal bremsstrahlung components coincided with the light curve maximum, but were only marginally less during "the dip" phase. The N_H, column density, parameter of the cold inhomogeneous absorption component varied between 7.7×10^{22} cm^{-2}–13.6×10^{22} cm^{-2} and its covering fraction between 0.55–0.81 with maximum attenuation during the "dip". Both the emission and the absorption tended to their minimum values during the minimum and secondary maximum phases.

The authors concluded that the rotational modulation is probably due to a combination of occultation of a large emission region and absorption in the accretion flow associated solely with "the dip". The absence of a soft X-ray excess they attributed to homogeneous accretion.

2.2.4 Accretion

Measurements of the magnetic field strength of PQ Gem indicate that it lies at the lower limit of the polar range. Hence the formation of a disc will depend on whether the ram pressure from the accreting material is sufficient to counteract the magnetic forces and allow circularisation of the material. Hellier (1997) considers that the array of orbital side bands seen in the optical, when coupled with the dominant X-ray modulation being at the white dwarf spin period, are supportive of disc accretion. In addition, he suggests that the orbital S-waves arise from the impact of the accretion stream with a disc (Section 1.2.1).

The spin-down condition implies that matter is being threaded (Section 1.2.2) outside the co-rotation radius (Section 1.2.2.2) so that the resulting torques act to slow down the rotation rate of the white dwarf. If this is the case, then it runs contrary to the Ghosh and Lamb standard accretion model (Section 1.2.2 & Figure 1.5). However, as stated in Chapter 1, this model pertains to an aligned rotator; whereas there is evidence from the polarimetric analysis of Piirola et al. (1994) and Potter et al. (1997) that PQ Gem is an oblique rotator.

The width of "the dip" at 0.4 spin cycles (Duck et al. 1994) and 40° (Howell et al. 1997) favour the accretion curtain model as the means of transport for material from the inner edge of the disc to the accretion impact site. In addition the extension of the accretion arcs towards the orbital plane (cyclotron modelling results) implies that the threading takes place over a range of radii (Potter et al. 1997). Furthermore, the phase lag of 0.11 spin cycles between "the dip" and the maximum from the 10-20keV light curve indicates that the accreting material impacts the white dwarf at 35°–40°, i.e. the magnetic field lines are twisted (Figure 2.3, reproduced from figure 6, Mason 1997). Doppler tomograms of optical emission lines also show that the accretion curtain is 30°–50° ahead of the impact site (Hellier 1997) as does the cyclotron modelling of Potter et al. (1997). An extended accretion area on or near to the white dwarf surface is indicated by the lack of Lyman absorption lines and the flat continuum (FUV) (Cash et al. 1998). All these factors plus the flickering effects visible in the light curves are symptomatic of inhomogeneous accretion (Section 1.2.2.1) and hence belie the homogeneous accretion model suggested by Duck et al. (1994).

2.2.5 Why is PQ Gem so Special?

It has been suggested that PQ Gem is an intermediary between the IPs and the polars due to their shared properties of a comparable magnetic field strength and strong EUV and soft X-ray components; and hence, is the first of its class to be literially

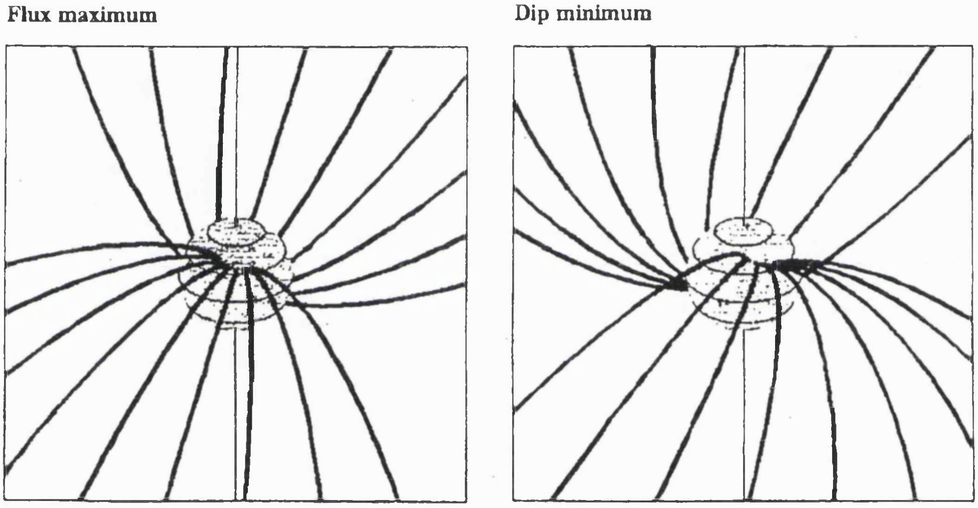

Figure 2.3: Inferred geometry of magnetic field lines along which matter is accreting in PQ Gem. The system is drawn at an orbital inclination of 60° and with a dipole offset of 30°, these being the best fit values deduced by Potter et al. (1997) from modelling the polarisation light curves. Only field lines which lie ahead of the magnetic pole in the spin cycle are shown and the star is rotating in a clockwise direction as seen from above the orbital plane. The two views are separated by 30° in spin phase and show the expected geometry at the middle of the soft X-ray dip and the phase of maximum X-ray light respectively. Reproduced from figure 6, Mason 1997

an "intermediate" polar. However, PQ Gem has many other unusual characteristics which are unrelated to typical polar attributes; for example, the double peaked spin pulse which is seen not only in the X-ray band, but also in the I- and R-bands, as well as its relatively high rate of spin-down. Nevertheless, the long list of PQ Gem's properties which map to typical IP attributes serve to emphasize the correctness of its IP classification. It is probably truer to state that it is the wide range of exceptional properties which makes PQ Gem so special rather than just its potential to bridge the IP and polar MCV classes.

2.3 V405 Aur or RX J0558+53

The IP V405 Aur (RX J0558+53) was also discovered by the *ROSAT* Galactic Plane Survey project (Haberl & Motch 1995). Its position is RA (2000.0) 05^h 58^m 0.1^s Dec (2000.0) $+53°$ $53'$ $58.9''$ with an error radius $9''$ (68% confidence) (Haberl et al. 1994).

2.3.1 System Parameters

The spin period of V405 Aur was initially identified as 272.74±0.02s from the *ROSAT* PSPC data (Haberl et al. 1994), but subsequently a pulse at half this frequency, i.e. a period of $545.4556 \pm 4.32 \times 10^{-5}$s, was discovered in optical data (Allan et al. 1996). These data were used to calculate an optical spin ephemeris of

$$HJD_{max} = 2449681.46394(6) + 0.006313143(5) \times E \qquad (2.2)$$

The epoch corresponds to the pulse maximum preceding the deeper of the two minima seen in the optical light curves (Figure 2.4). The orbital period was determined at 4.15h (Allan et al. 1996), and the beat period was calculated to be 565.8s (Harlaftis & Horne 1999).

The distance was estimated by Haberl et al. (1994) to be 300pc ±100pc which yielded an average X-ray luminosity of 1.8×10^{32}erg s^{-1} (0.1-2.4keV). Harlaftis & Horne (1999) calculated the magnetic field strength, B, at 0.5MG, though (Haberl

Figure 2.4: Spin phase-folded light curves of V405 Aur for optical waveband (left-hand figure) and the 'soft' (0.1–0.5keV) and 'hard' (0.6–2.0keV) *ROSAT* PSPC spectral bands (right-hand figure, top and bottom plots respectively). Reproduced from Allen et al. (1996), figures 2 & 4.

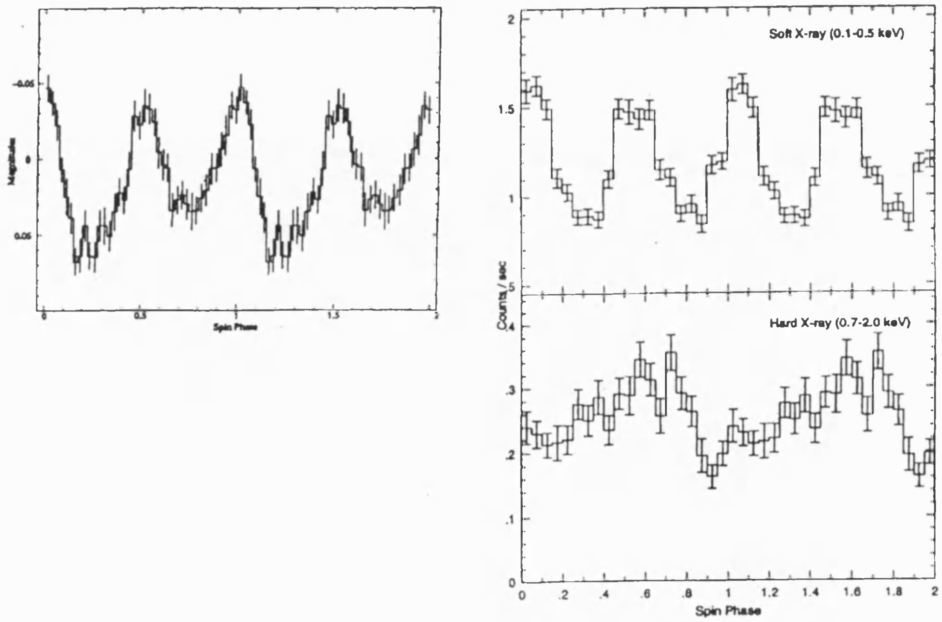

& Motch 1995) suggest that B is much closer to that of PQ Gem, because of their similar hard bremsstrahlung to soft blackbody component flux ratios (Ramsay et al. 1994). This is supported by the reported detection of periodic variations in circular polarisation on the 544.4s ± 4.8s period and possibly that corresponding to 2ω (1st harmonic of the spin frequency) by Shakhovskoj & Kolesnikov (1997). The mass of the white dwarf has been calculated at $1.1\mathrm{M}_{\odot}$ using data from *RXTE* and a stratified-accretion-column model (Ramsay 2000).

2.3.2 X-ray Light Curves

The *ROSAT* "soft" X-ray (0.1–0.5keV) light curve (Figure 2.4) shows the very distinct double peaked emission which lead to the initial misidentification of the spin period at 272s. Allan et al. (1996) proposed the weak magnetic field/fast rotator model (Section 1.3.4) as an explanation for the observed double pulse in the optical and *ROSAT* 0.1–0.5keV light curve. On the other hand, the *ROSAT* "hard" X-ray (0.7–2.0keV) light curve (Figure 2.4) is more or less single peaked (Haberl et al. 1994).

2.3.3 X-ray Spectroscopy

Phase-resolved X-ray spectroscopy using the *ROSAT* data was carried out by Haberl et al. (1994). They found that below 0.7keV the spectrum was well represented by a blackbody model with a temperature of ~57eV. This soft X-ray component varied by factor of ~2 around the 272s cycle and could be explained by a change in the normalisation alone. In other words, they found that it was possible to account for the spectral variations solely by geometric effects. This is different to PQ Gem which requires both geometric (occultation and viewing angle) and absorption effects. Haberl et al. (1994) estimated the size of the blackbody region at pulse maximum to be $4\times10^{3}\mathrm{km}^{2}$, a very small area if it corresponds to a ring around the accretion column. On the other hand it could be that only a small percentage of the area is visible. They fixed the temperature for the hard X-ray component at 10keV, since this was a typical expected temperature for an IP. Not only did the normalisation of this component vary very little over the 272s period, but it was also possible to model the absorption by a fixed column density of 6×10^{20} H cm^{-2}.

2.3.4 Accretion Scenario

Accretion via disc overflow has been suggested by two authors: by Harlaftis & Horne (1999), due to the presence in the emission lines of their optical data of the $2(\omega\text{-}\Omega)$ and 2ω pulses, but without a $(2\omega\text{-}\Omega)$ pulse (ω is the spin frequency, Ω is the orbital frequency and $(\omega\text{-}\Omega)$ is the beat frequency), and by Still et al. (1998), because their data showed double peaks in Hα line profiles together with the absence of a beat pulse. On the other hand, Allan et al. (1996) suggested that the lack of orbital modulation in their data implies a system of moderate to low inclination with accretion through a disc. Both Harlaftis & Horne (1999) and Still et al. (1998) find evidence for accretion onto both poles.

2.4 RX J1712.6-2414

RX J1712.6-2414 is one of the six IPs discovered by the *ROSAT* Galactic Plane Survey project (Haberl & Motch 1995). Its position is RA (2000.0) $17^h\ 12^m\ 35.94^s$ Dec (2000.0) -24° 14′ 41″ within a statistical error radius of 6″ (Buckley et al. 1995).

The emphasis of previous research on RX J1712.6-2414 has concentrated on distinguishing and establishing the values of the beat and spin period as well as using the results from photometry, polarimetry and spectroscopy to determine the most probable system orientation, the mode of accretion and the magnetic field strength.

2.4.1 System Parameters

Buckley et al. (1995, 1997) carried out extensive photometric and polarimetric analyses. They found that the RX J1712.6-2414 demonstrated the highest level of variable circular polarisation of any IP; this increased redwards in a manner similar to that of PQ Gem (Piirola et al. 1993) and BG CMi (West et al. 1987). The polarimetry data showed modulation on a 927.66±0.41s period which they interpreted as the spin period, since polarimetric data are most likely to be modulated by the rotation of the white dwarf. Polarimetric and photometric periods were demonstrably different with observed periods of 1003s and 1027s periods as candidates for the latter; but, the presence of "red noise" (significant power peaks at low frequencies) in the periodograms tended to mask any coherent variations. An unambiguous $1003.299 \pm 0.003s$ period was determined from *ROSAT* PSPC data which they interpreted as the beat period; the PSPC light curve is shown folded on this period in Figure 2.5. They did not find evidence for a beat pulse nor any periodicity other than at the spin period in their later filtered polarimetry, though aliases of the spin period at 918s and 938s were detected in their initial data. Also, they found very little evidence for a spin period ($\leq$4%) in the *ROSAT* data.

RXJ1712.6-2414 is the first IP in which the dominant X-ray frequency is at the beat period. They ascribe the beat pulse to "gating" of some of the accreting material to the nearest pole in such a fashion that there is an imbalance of 30%–40% in the accretion rate between the 2 poles. An orbital period of 3.42±0.02h was implied from the 1003s beat period and the 927s spin period. They concluded that the system is observed nearly pole-on so that only one of the two accreting poles is ever directly visible and that this pole is always accreting some material. They suggested that the dipole tilt angle must be quite small so as to hide large velocity variations at the synodic period though, nevertheless, sufficiently large to give the observed modulation.

Buckley et al. (1995) calculated the magnetic field strength, B, at $\geq$5MG using the cyclotron emission model of Wickramasinghe et al. (1991) with 8MG as their preferred value. Similarly, Väth (1997) determined B to be 9–27MG using a model that included the structure of accretion shock region for a system geometry in which the axis of the magnetic dipole is offset to the spin axis by angle β, i.e. a similar model to that used by the Väth et al.(1996) for PQ Gem. Nevertheless, the lack of hard X-ray observations meant that neither the mass nor the accretion rate could be

Figure 2.5: *ROSAT* PSPC X-ray light curve folded on the 1003s beat period. Reproduced from Buckley et al. (1997).

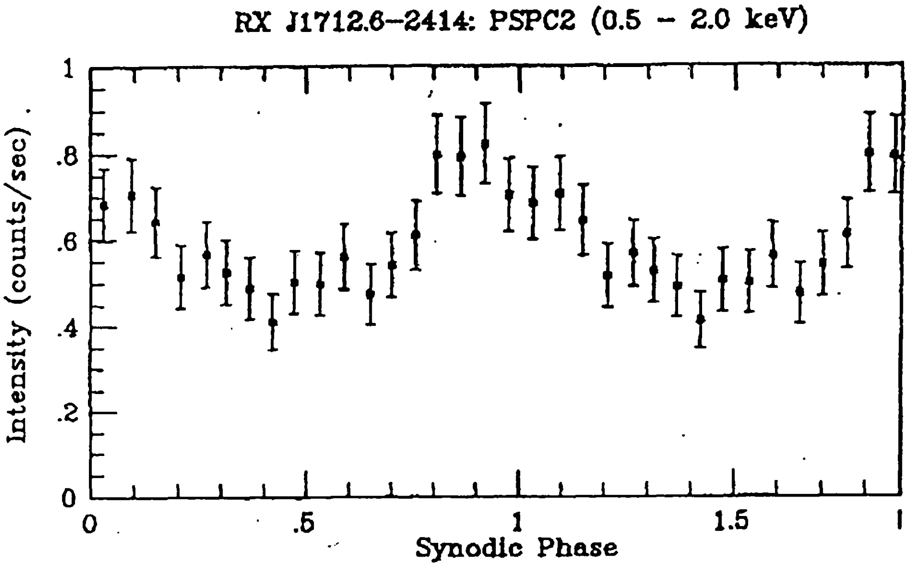

constrained. These lead to large uncertainties in his estimates of the strength of the magnetic field. The mass of the white dwarf has since been calculated at $0.71\mathrm{M}_{\odot}$ using data from *RXTE* with the stratified-accretion-column model (Ramsay 2000) and $0.62\mathrm{M}_{\odot}$ using *ASCA* data with an emission line technique (Ezuka & Ishida 1999). These are sufficient to constrain the likely range of the B to 15–26MG (by reference to table 3, Väth 1997). The corresponding range in distance is given as 590–1400pc.

The probability of a relatively high magnetic field strength, the short orbital period and the strong photometric beat period (when observed) points to discless accretion in RX J1712.6-2414 (Buckley et al. 1995, 1997). Furthermore, simulations of emission line radial velocity modulation expected from discless IPs with the parameters set for accretion onto both poles, i=0.0°±0.5° and a low valued β, replicate well those of RX J1712.6-2414 (Garlick 1996).

2.4.2 Spectroscopy

Spectral analysis of *ROSAT* data (Buckley et al. 1997) gave an unconstrained hard bremsstrahlung emission at a temperature $\geq$3keV. The absorption was modelled by an equivalent column density of neutral hydrogen of 10^{20}–10^{21} H cm^2. Phase-resolved spectral analysis with the temperature fixed at 10keV showed that the spectral variation between the maximum and minimum of the PSPC light curve (folded on the beat pulse) could be accounted for mainly by a variation in the normalisation alone though a slight decrease in the absorption at maximum phase was noted. They did not find the need to include a soft X-ray component to fit the PSPC data.

2.5 Summary

The IPs PQ Gem, V405 Aur and RX J1712.6-2414 have now been introduced. By way of comparison, their most important characteristics, with respect to the subsequent chapters, are summarized in Table 2.2.

	PQ Gem	V405 Aur	RX J1712.6-2414
System Parameters			
mass of the WD ($M_\odot$)	1.35(>1.05)	1.10 (0.88-1.14)	0.71 (0.68-0.78)
distance (pc)	400	300±100	589-1400
B (MG)	~14±5	0.5	20±5
spin period (s)	$833.4033235 \pm 8.64 \times 10^{-5}$	$545.4556 \pm 4.32 \times 10^{-5}$	927.66±0.41
beat period (s)	870	565.8	1003.299±0.003
orbital period (hr)	5.19±0.01	4.1428±.00264	3.42±0.02
dominant mod: pulse (X-ray)	spin	spin	beat
i	60°	medium to low	0.0°±0.5°
β	30°	unknown	low
accretion onto 2 poles	yes	yes	yes
accretion mode	disc	disc(+stream)	discless
Observational Properties			
circular polarisation	modulated	yes	modulated
soft component	yes	yes	no
N_H (H 10^{22} cm^{-2})	7.7-13.6	0.057±.003	0.01-0.1
temp: hard component (keV)	20	unknown	≥3
temp: soft component (eV)	20-60	57±2	n/a

Table 2.2: Table summarizing the main system and observational parameters for PQ Gem, V405 Aur and RX J1712.6-24141. The symbols used are: WD for the white dwarf, B for the magnetic field strength, i for the angle of inclination and β for the dipole offset angle.

Chapter 3

Observations, Data Reduction and Analysis

This chapter introduces the data which are subsequently used for analysis in the following chapters. It also covers the techniques used to reduce and analyse these data. *Ftools* was the standard software used throughout the former task.

All the *RXTE* and *ASCA* data used in the analysis was obtained from the "Legacy" data archive at the Goddard Space Flight Center (GSFC).

3.1 ASCA

3.1.1 ASCA Instrumentation

ASCA was Japan's fourth cosmic X-ray astronomy mission. Its instrumentation included four wide area X-ray telescopes (XRT), two gas imaging spectrometers (GIS) and two solid state imaging spectrometers (SIS). Each telescope carried one of the four instruments at its focus which enabled all of them to be deployed simultaneously. The GIS detector was a gas imaging scintillation proportional counter whereas that of the SIS was a charge coupled device (CCD) camera. The satellite was launched on February 20, 1993 and continued in service until the year 2000 when damage during

instrument	passband keV	FOV diameter	timing resolution	energy resolution	effective Area
GIS	0.7–10	50 arcmin	62.5m hbr 500ms mbr	8% at 5.9keV	$\sim$40cm^2 at 1keV $\sim$90cm^2 at 7keV
SIS	0.4–10	(22 arcmin)^2	4s per CCD readout	2% at 5.9keV	$\sim$120cm^2 at 1keV $\sim$70cm^2 at 7keV

Table 3.1: Characteristics of *ASCA*'s instrumentation (FOV is the field of view, hbr is high bitrate data and mbr = medium bitrate data). The energy resolution of the GIS and SIS are measured in terms of FWHM $\Delta E/E$.

a severe geomagnetic storm sent it into safe-hold mode. Subsequently, the battery power became exhausted and all attempts to re-establish normal operating mode failed. The spacecraft re-entered the Earth's atmosphere over the western Pacific on the 2nd March 2001. A review of the *ASCA* instrumentation is given in Tanaka et al. (1994), but a summary of the main characteristics of the detectors is provided in Table 3.1

The scientific goal of *ASCA* was to provide spectroscopy of cosmic X-ray plasmas. This was catered for by a combination of imaging, broad passband spectroscopy, good spectral resolution and a large effective area.

3.1.2 Observations from ASCA

All the *ASCA* data used for this thesis were retrieved from the *ASCA* public domain archive. PQ Gem was observed by *ASCA* in 1994 and 1999. The data from the first observation was used by Mason (1997) to determine a quadratic ephemeris (Section 2.2.5.3) and also to derive the models used in XMM RGS simulations (James et al. 1998). The data from the second was not released into the public domain until the end of the year 2000 and hence, was not available for this thesis. V405 Aur was observed in both 1996 and 1999, though the second of these observations is of relatively short duration. RX J1712.6-24 was observed in 1996. The details of these observations are given in Table 3.2.

3.1.3 Reduction of ASCA Data

Data reduction was started from the unscreened files which necessitated the elimination of those events which degrade the quality of the data. Some of this degradation originates from instrumental effects whereas some is due to the location of the satellite at the time the data was collected. One such local effect is the South Atlantic Anomaly (SAA) which is a "hole" in the geomagnetic field that leads to a higher than average level of background particles. The GIS, but not the SIS, instruments were switched off during SAA passage; therefore these times were also removed from the SIS data. The cut-off rigidity (COR) is a local measure of the ability of the geomagnetic field to repel cosmic rays. SIS and GIS events with COR $>$ 6 and $>$ 4, respectively, were excluded from the data. All data within 10° of the Earth's limb were removed, so as to eliminate source data contaminated by the Earth's atmosphere (absorption and scattering by the atmosphere leads to distortion of the spectra). The SIS CCDs were also sensitive to UV and optical radiation; therefore all data within 15° of the Earth's illuminated face were discarded. The radiation belt monitor (GIS) and pixel rejection (SIS) thresholds were set to 250 and 75 respectively so as to reject high particle count data. Hot/flickering pixels were also removed. Deviation from the true pointing position was limited to 0.01° and the option to remove the ring (the majority of non-X-ray events occur in the outer ring of the FOV) and calibration source events from the GIS data was implemented.

Further selection was then performed based on the location of the source in the image area together with energy and timing considerations. Region files of 4 arcmin (38 pixels) and 6 arcmin (24 pixels) radius from the centre of the source image were created from the SIS and GIS screened data respectively, so as to include as much as

object	date	ObsID	instru -ment	bit rate	integ: time s	obs: cts/s	CCDs	data mode
PQ Gem	04/11/94	32000000	SIS0	high	26786	0.3497±.0034	2	bright
				medium	36910	0.3785±.0038	1	bright
			SIS1	high	24732	0.2873±.0035	2	bright
				medium	34734	0.3132±.0031	1	bright
			GIS2	high	27771	0.2493±.0056	n/a	PH
V405 Aur	05/10/96	34005000	SIS0	high	44233	0.3067±.0029	1	faint
			SIS1	high	42059	0.2719±.0026	1	faint
			GIS2	high	45592	0.2203±.0050	n/a	PH
	21/03/99	37005000	SIS0	high	16623	0.3755±.0049	1	faint
			SIS1	high	16539	0.3020±.0045	1	faint
			GIS2	high	17601	0.2428±.0058	n/a	PH
			GIS3	high	17587	0.2944±.0060	n/a	PH
RX J1712.6-24	18/03/96	34011000	SIS0	high	42349	0.7958±.0047	2	faint
			SIS1	high	42657	0.6595±.0043	2	faint
			GIS2	high	45395	0.5772±.0037	n/a	PH
			GIS3	high	45377	0.7231±.0041	n/a	PH

Table 3.2: Details of the *ASCA* observations and data used in the analysis for this thesis. Technical difficulties inhibited the extraction of phase-resolved spectra from the GIS3 data of PQ Gem and that of V405 Aur was too noisy to be used. Hence, details of these data are not included in this table. Those data integrated in faint mode were converted to bright mode on the ground prior to distribution.

possible of the point spread function (PSF) across the energy range. These region files were then used to limit the spatial extent of selected events during the extraction of all light curves and spectra. In addition, a phase filter was applied to extract phase-resolved spectra, whereas a PHA cut filter was used when it was required to limit the energy range of the light curves. The former filter requires an epoch and period as well as the targeted fraction of the period (phase). The epoch for both PQ Gem and V405 Aur was identified by calculating the integral number of cycles from a previously calculated ephemeris to the initial phase 0.0 within the data. For PQ Gem the quadratic ephemeris of Mason (1997) was used and for V405 Aur the 545.4556s period ephemeris of Allan et al. (1996). A previously calculated ephemeris was not available for the beat cycle of RX J1712.6-24, therefore an arbitrary epoch was chosen. These same epochs were used to fold the light curves using code which optionally enables the specification of a quadratic ephemeris.

There are two recommended ways to create background spectra. The Guest Observer Facility (GOF) accumulated separate files of background events from blank field observations corresponding to different COR conditions at the start of the mission. The source region file can be used on the background file with matching COR to create a background spectrum. Otherwise one can extract a spectrum from a source-free part of the same observation to which identical screening criteria have been applied. Spectral background files for PQ Gem were made from the GOF files, because deviation from the instrumental conditions pertaining to their production were expected to be minimal, given the closeness of the observation to mission start. In the case of V405 Aur, background files were created by both methods and their effectiveness compared. It was found that the GOF background files resulted in a less noisy background-subtracted spectrum for observation 34005000, but otherwise there was no apparent disparity. The difference was less marked for observation 37005000, even so the GOF-produced background files were marginally less noisy, so they were chosen in both instances. Since carrying out the analysis on the V405 Aur data it has been recognised by the GOF that the deterioration in the SIS CCDs after the end of 1994 has lead to reduced efficiency in both the SIS1 and SIS0 instruments below 1keV which can be roughly characterized as an excess absorption (T.Yaqoob et al. 2000, ASCA GOF 2000). In turn this means that the blank-sky observations are no longer an appropriate source from which to create spectral background files after this date. Hence, this must be taken into account when interpreting the results from the spectral analysis of this object. However, the minimal differences between the background-subtracted spectra obtained by the two methods suggest that the results of the analysis are still valid. The spectral background files for RX J1712.6-24 were created from a source-free area of the CCD chip. The GOF also produced blank-sky observations sorted by COR values for use as GIS spectral background.

Background light curves were created from a source-free region of the same observation and subjected to identical screening criteria as for the source light curves. These were subtracted from the appropriate screened source files.

The response files for SIS data were created using the standard *ASCA* subpackage of the FTOOLS software whereas those for GIS were provided by GOF. In both instances the ancillary response files were created using the standard software. The GOF-noted decrease in the efficiency of the CCDs below 1keV for those observations after the end of 1994 was allowed for during the data analysis of V405 Aur and RX J1712.6-2414 by excluding those events with energies < 1keV.

3.2 RXTE

3.2.1 The RXTE Satellite

The Rossi X-ray Timing Explorer (*RXTE*) was developed by NASA. It carries three instruments: the proportional counter array (PCA) operating at low X-ray energies (2–60keV); the high energy X-ray timing experiment (HEXTE, 20-200keV); and the All-Sky monitor (ASM, 2–10keV) which covers approximately 80% of the sky every orbit. The PCA and HEXTE instruments are co-aligned and have the same field of view of 1° (FWHM). Data from both the PCA and ASM are processed on board the satellite by the experiment data system (EDS). The satellite was designed for

parameter	specification
Energy range	2–60 keV
Energy resolution	$< 18\%$ at 6 keV (FWHM $\Delta E/E$)
Time resolution	1μs
FOV/Spatial resolution	collimator with 1° FWHM
Detectors	5 Proportional Counter Units (PCU)
Collecting area	6500cm^2
Layers	1 Propane electron veto
	3 xenon
	1 xenon veto detector for charged particles

Table 3.3: The main characteristics of the PCA instrument on board the *RXTE* satellite.

a required lifetime of two years, but with a target of five years. It was launched into low-Earth orbit on December 30, 1995 and is still functioning well. Its scientific aims are to provide information on the variability of X-ray sources on timescales of a few seconds to several months with moderate spectral resolution. A review of the available instrumentation and scientific results of the first couple years are given in Swank (1998). The three IPs studied here are fairly faint objects which radiate mainly below 30keV. Hence the analysis was restricted to data from the PCA instrument. A summary of its main characteristics is given in Table 3.3.

3.2.2 Observations using RXTE

Both V405 Aur and RX J1712.6-2414 were observed using the *RXTE* satellite in 1996 (these data were used by Ramsay (2000) to determine the white dwarfs masses). The observation of PQ Gem was made in 1997. Details of the observations are included in Table 3.4.

3.2.3 Reduction of RXTE Data

As with *ASCA* it was necessary to purge the data by eliminating those events which diminish its quality, e.g. data following passage through the SAA and data contaminated by the Earth's atmosphere (Section 3.1.3). It was also necessary to eliminate data accumulated while the spacecraft was slewing as well as any events recorded while less than 5 PCUs were active. In addition, anti-coincidence recorded events caused by high energy electrons were discarded. The data selection criteria were as recommended by the XTE GOF with the exception that the recommended allowed offset to the true pointing position was halved to 0.01° so as to eliminate the majority of any vignetting effects from the collimators. Relevant housekeeping data for each ObsID (a single "observation" which is a temporally contiguous set of data from a single pointing, Table 3.4) of an observation was accumulated into a filter file in order to facilitate the rejection of unwanted events. The filter files for a complete observation were then combined together. These two sets of information (selection criteria and filter file) were then used to create a good timing interval (GTI) file.

The GTI file enabled the extraction of an integrated spectrum and light curve. During this procedure it was also possible to limit the energy channels chosen, thus enabling the production of light curves for specific energy ranges. These light curves were folded in the same manner as those from *ASCA* (Section 3.1.3)

The *RXTE* GOF provide separate background models for bright and faint sources for different gain epochs (currently 4) during the lifetime of the *RXTE* satellite. The three IPs discussed in this thesis are classified as faint sources since they have a count rate of less than 40cts s^{-1} per PCU. The observations, of PQ Gem and V405 Aur both fell within gain epoch 3, whereas RX J1712.6-2414 straddled gain epochs 1 and 3. Hence data reduction for the last object was limited to the longer portion of the observation which corresponded to epoch 3. A separate synthetic background file was created for each source file from the appropriate model files. Background spectra and light curves were then extracted from the synthetic

object	date	ObsID	Integration Time s	obs: cts/s
PQ Gem	1997-01-27	20021-02-01-00	51216	13.91±0.05
		20021-02-01-000		
	1997-01-28	20021-02-01-01		
		20021-02-01-010		
	1997-01-29	20021-02-01-02		
		20021-02-01-020		
	1997-01-30	20021-02-01-03		
		20021-02-01-030		
V405 Aur	1996-04-26	10027-04-01-00	19232	13.89±0.09
		10027-04-01-01		
		10027-04-01-02		
		10027-04-01-03		
RX J1712.6-24	1996-03-12	10037-01-01-00		
	1996-03-13	10037-01-03-00		
		10037-01-06-00		
	1996-05-13	10037-01-07-00	40016	41.47±0.06
	1996-05-14	10037-01-08-00		
	1996-05-15	10037-01-09-00		
	1996-05-17	10037-01-11-00		
	1996-05-18	10037-01-10-00		
		10037-01-12-00		
		10037-01-13-00		
	1996-05-19	10037-01-14-00		
		10037-01-15-00		
		10037-01-16-00		

Table 3.4: Details of the *RXTE* observations and data used in the analysis for this thesis. ObsIDs refers to a single "observation" which is a temporally contiguous set of data from a single pointing. The integration time and observed count-rate is for the merged ObsIds for the complete observation of the target object except for RX J1712.6-24 data with respect to 1996-03-12/13 which is excluded, because it belongs to a different gain epoch to the remainder of the observation.

background files using standard software.

A response file for the specified PCA layers was created using standard software together with the GTI and pha files.

3.3 Data Analysis

3.3.1 Searching for Periodic Signals

Time-series analysis is the standard technique used to look for the presence of periodic signals in CV data. The majority of the data is unevenly sampled, hence an appropriate mathematical tool for this analysis is a form of the Discrete Fourier Transform (DFT) called the periodogram (Deeming 1975). The DFT for unevenly sampled data set (X(t$_i$,i=1,2,...,N_0) can be defined as

$$FT_X(\omega) = \sum_{j=1}^{N_0} X(t_j) exp(-i\omega t_j) \tag{3.1}$$

The *classical* periodogram (Scargle 1982) is customarily defined as $P_X(\omega) = 1/N_0|FT_X(\omega)|^2$ which can then be re-expressed as

$$P_X(\omega) = 1/N_0[(\sum_j X_j \cos\omega t_j)^2 + (\sum_j X_j \sin\omega t_j)^2] \tag{3.2}$$

The benefit of this formulation is that if the data contains a sinusoidal component of frequency ω_0 then the factors exp($-iwt$) and $X(t)$ are in phase when $\omega \sim\omega_0$ and hence make a large contribution to the DFT sum. Conversely when ω is not close to ω_0 then the two factors tend to cancel and make a very small contribution to the DFT sum.

A power peak in a periodogram is not necessarily due to a genuine periodic signal; yet it is essential to be able to distinguish the genuine signals from those that are spurious. This can be difficult since the inspection of many frequencies gives an expectation of a large peak power even in the absence of a periodic signal (Scargle 1982). The *classical* periodogram (with a few minor modifications) is exactly equivalent to the least-squares fitting of sine waves of various periods to the data.

Therefore it is possible to define a power level, z_0, such that false alarm probability, p_0, is acceptably low;

$$z_0 = \ln[1 - (1 - p_0)^{1/N}] \qquad (3.3)$$

where N = the number of frequencies searched (Scargle 1982). Kurtz (1985) showed that for large datasets the differences between this "modified" periodogram and the *classical* periodogram (equation 3.2) were insignificant. He also derived a technique to reduce the DFT computation time by a factor of 4 – 6.

Spectral leakage is a phenomenum caused partially by the finite total interval over which the data is sampled (leakage of power to nearby frequencies) and partially by the finite size of the intervals between samples (leakage of power to distant frequencies). Also, regularity in the spacing of the arbitrary sampling can lead to spurious periods. The window function is an expression of the effect of such contamination on the ideal.

3.3.2 Modelling and Fitting of X-ray Spectrum

3.3.2.1 Spectral Fitting

During an observation of a cosmic X-ray source, photons with a range of X-ray energies, interact with one or more instrument components whose performance characteristics determine the observed spectrum. Consideration of the instrumental response has two aspects, the energy dependence of the spectral resolution and the sensitivity (effective area) over the energy range of the instrument. Hence, the recorded data is a convolution of the properties of the source photons with the response of the instrument(s) expressed as the number of counts per energy channel over the range of energy channels. The energy resolution and effective area of imaging instruments can be further complicated by spatial dependency due to uneven response across the field of view (also, the mirror introduces spatial dependencies). The calibration of the instrumental response is realized as one or more software response matrices.

Spectral fitting of X-ray data is accomplished by defining a parameterised model which is physically realistic given the current state of knowledge of the object under investigation and the specific aims of the analysis. This model is then convolved with the instrument response matrices and fitted to the observed data by varying the parameter values to the model. Prior to the spectral fitting process a background spectrum (an spectrum representative of the background particle and X-ray components) is subtracted from the observed data.

It is normal that the best fit model is determined using the χ^2 statistic,

$$\chi^2 = \sum((y_i - y(x_i))/\sigma_i)^2$$

where y_i is the data, $y(x_i)$ is the fitting function and σ_i^2 are the variances, (Bevington & Robinson 1992) . The goodness-of-fit criterion, $\chi^2_\nu = \chi^2/\nu$ (where ν is the number of degrees of freedom) needs to be as close as possible to unity. A value greatly exceeding this indicates that the model is a poor fit to the data whereas a value much less than 1 suggests that the errors are large, probably, because of the low statistical quality of the data.

The spectral fitting software package *xspec* (Arnaud 1996) was used in the spectral analysis throughout this thesis.

3.3.2.2 The Models

The generally accepted physical models for homogeneous and inhomogeneous accretion were discussed in Section 1.2.2 and are illustrated in Figures 1.3 and 1.2 respectively. The hard X-ray emission is considered to be optically thin, i.e. the photons can escape from the vicinity of the column without any intermediate interactions; hence, the observed flux is isotropic. This means that an optically thin plasma model is appropriate, so the MEKAL code (Mewe et al. 1995) was used in this work. The normalisation parameter, K, for this model is defined by the expression:

$$K = (10^{-14}/(4\pi D^2)) \int n_e n_H dV$$

where D is the distance to the source (cm), n_e and n_H are the electron and H densities (cm^{-3}).

The MEKAL code includes emission lines for the main energy transitions, but the Fe fluorescent line at 6.4keV is not included. In those instances where the data requires it, a Gaussian component is added to the model at this energy. In this thesis its width has been limited to 0.05keV, because the complex Fe emission in the 6.0-7.5keV energy band tends to cause it to spread to a physically unrealistic width. The normalisation parameter of the Gaussian model is given as: K = total photons cm^{-2}s^{-1} in the line.

The soft component is believed to owe its origin to a combination of reprocessing of hard X-rays and thermalisation of material deposited sub-photospherically. Normally, a blackbody model (optically thick) is used to model the soft X-ray emission; however, it gives a rather poor physical approximation because the lower opacity of the atmosphere of the white dwarf allows observation into deeper, hotter layers of the stellar atmosphere. Comparison with an irradiated stellar atmosphere model shows that, over all, the blackbody model overestimates the effective temperature by a factor of 2–5. Any additional accretion energy deposited at large optical depths (e.g. blobs) effectively augments the intrinsic stellar flux. On the other hand, the greater the contribution from reprocessing of hard X-rays, the closer the flux becomes to a black body distribution (Williams et al. 1987). The normalisation parameter, K, of the blackbody model is defined as:

$$K = L_{39}/D_{10}^2$$

where L_{39} is the source luminosity in units of 10^{39} erg s^{-1} and D_{10} is the distance to the source in units of 10kpc.

X-ray emission from the source can be attenuated by the interception of absorbing material along the line of sight. Sources of such material in IPs are the interstellar medium (ISM, cool gas), the accretion stream (cool, partially ionised gas), the accretion disc (which has a temperature gradient from the cooler outer edge to the warmer inner edge) and the accretion curtain (cool, partially ionised gas). The boundary layer and impact regions which have higher local temperatures are exceptions to the general temperature structure of the accretion disc. Photoelectric (bound-free) absorption in which an X-ray photon is absorbed by an atom with the ensuing emission of a K-electron (of kinetic energy $h\nu - P_{ai}$, where h is Plank's constant, ν is the frequency of the photon and P_{ai} is the atomic ionisation potential) is the dominant absorption process in cool (strictly speaking, neutral) gas. Photoelectric absorption increases exponentially with decreasing emission energy such that its effect is most apparent for radiation below 3keV and is characterised by edges at energies P_{ai} for the various elements present in the absorber. It can be expressed by:

$$I(h\nu) = I_0(h\nu)\exp(-\sigma(h\nu)N_H$$

where I is the observed intensity, I_0 is the initial intensity, h is Plank's constant, ν is the frequency of the photon, σ is the effective absorption cross-section (i.e. the sum of the photoelectric cross-sections of relevant elements, weighted by their cosmic abundance) and N_H is the number of H atoms along the line of sight (Ryter et al. 1975). A homogeneous photoelectric absorption model is most appropriate for the interstellar medium and constant intra-system absorption components. On the other hand, an inhomogeneous model has been found to be particularly suited to situations where the characteristics of the attenuating material vary, such as in inhomogeneous accretion (Norton & Watson 1989). The inhomogeneous or partial covering fraction absorber is expressed as a multiplicative factor, $M(E)$, such that

$$M(E) = (f\exp(-C\sigma(E)) + (1-f) \tag{3.4}$$

where f is the covering fraction, σ is the photoelectric cross-section, C is the equivalent hydrogen column in units of 10^{22} atoms cm^{-2} and E is the energy. Hence, it is normal to combine this with a homogeneous absorber which accounts singly for the attenuation over the lesser absorbed areas, $(1-f)$, but amalgamates with the expression $(f\exp(-C\sigma(E))$, Equation 3.4, over the areas of greater absorption.

The accreting material immediately prior to the shock is warm and partially ionised due to heating from postshock radiation (see also section 1.2.2.1). Done et al. (1992, appendix B) developed a model for a warm absorber which assumed a power-law for the photoionising spectrum. This model was made generally available in the spectral fitting software package, *xspec*, through the work of Zdziarski & Magdziarz (1996). Cropper et al. (1998b) adapted this model so that it accepted any photoionising spectrum. Therefore, the spectrum calculated from fitting the stratified-accretion-column model (Section 1.3.1.1) can be input to this warm absorber model. In so doing it assumes that the radiation originates from the midpoint point of the postshock accretion column. This adapted model is the warm absorber model used in this thesis (a detailed description can be found in Cropper et al. 1998b). However, it must be noticed that these models do not deal with radiative transfer in a fully consistent manner.

The applicability of some these model components to IPs in general is commented on in Section 1.3.3.

There are several issues in the stratified-accretion-column model for calculating the mass of the white dwarf (Section 1.3.1.1.) which need to be introduced. Firstly, the underlying physical model represents a solitary, cylindrical emission region and hence, ideally, the data should be restricted to those spin phases which correspond to the visibility of a single emission region. The importance of the reflection component within the model is governed by the viewing angle to the emission region. Equation 35, $\cos\alpha = \cos i \cos\beta - \sin i \sin\beta \cos\phi$ (where i, β are as defined in Figure 1.7 and ϕ is the phase) from Imamura & Durisen (1983) was used in this thesis to estimate an average of the viewing angle, α, for those cases where the data could be restricted in this fashion. Otherwise, where it is not feasible to implement this restriction, the white dwarf mass lies somewhere between the value estimated with the reflection effect at a maximum and at a minimum; i.e. between a viewing angle of 0° and 90° respectively. The parameter for the ratio of the cooling timescale for bremsstrahlung cooling to that for cyclotron cooling is ϵ_{s_0}.

3.3.3 The Approach

Norton and Watson (1989) carried out a survey of IPs using spectral analysis of *EXOSAT* data to probe the possible origin(s) of the light curve modulation. To investigate the role of absorption they held the emission components fixed while allowing the absorption to vary between the 2 phases (corresponding to flux minimum and flux maximum) during the spectral fitting. Similarly, the contribution from fluctuations in the visibility of the emission region(s) was explored by permitting the emission normalisation to vary while the absorption and emission temperature parameters were held constant. They obtained the best fits with models in which both the emission normalisation and the absorption were allowed to vary from that used to fit the integrated spectrum. They concluded that the origin for the light curve modulation involved both self-occultation of the emission regions and varying photo-electric absorption. These two effects acted in phase and the emission region covered at least 25% of the white dwarf surface. Their preferred explanation was the inhomogeneous discless accretion model of Hameury et al. (1986b) (Section 1.3.4).

In this thesis a similar approach was taken to that of Norton and Watson (1989) with the aim of ascertaining the contribution from self-occultation of the emission regions and/or absorption in the modulation of the light curves of the 3 IPs, PQ Gem, V405 Aur and RX J1712.6-2414. The energy resolution and effective area of X-ray detectors had much improved since the era of the *EXOSAT* satellite. Hence, it was expected that the characteristics of *ASCA* (Table 3.1) would facilitate a greater depth of understanding. The *RXTE* data with its moderate energy and good timing resolution (Table 3.3) was identified as providing the additional information required at higher X-ray energies.

Chapter 4

X-ray Analysis of PQ Gem

4.1 Preamble

The historical aspects of PQ Gem were introduced in Section 2.2. It has been observed twice by the *ASCA* (Table 3.2) and once by the *RXTE* (Table 3.4) satellites. Details of the data reduction performed is supplied in Sections 3.1.3 and 3.2.3, respectively; whereas Section 3.3 examines the data analysis techniques. For this thesis and James et al. (in preparation), phase-resolved spectral analysis of the *ASCA* observation from 27/11/94 was carried out to ascertain the contribution from absorption and the visibility of the emission regions in shaping the observed modulation of the X-ray light curves. Corroborating evidence is provided by the *RXTE* data which is also used to calculate the mass of the white dwarf.

4.2 The Light Curves

The quadratic spin ephemeris of Mason (1997) was used in the analysis of the light curves (Equation 2.1).

4.2.1 Period Analysis

The variability in the *RXTE* and *ASCA* light curves was analysed using a standard discrete Fourier transform (DFT) code (Deeming 1975, Kurtz 1985). Equation 3.3 (Section 3.3.1) with p_0 set to 0.1, i.e. 90% confidence, was used to determine the signal-to-noise level below which the amplitude of a power peak was judged to be insignificant. The noise level of the periodogram was taken to be the mean of the amplitude spectrum after it had been prewhitened with frequencies found to be significant (Table 4.1). The error in each such frequency was taken to be the standard deviation, σ, from the least squares fitting procedure determined during the prewhitening of the power spectrum.

The *RXTE* data showed a single power peak with an amplitude $\geq z_0$, Equation 3.3 (Section 3.3.1). This occurred at $1.199803\times10^{-3}\pm8.1\times10^{-8}$ Hz which corresponds to a period of 833.540±0.056s, i.e. the spin period (Section 2.2.1.4) . The *ASCA* data gave the maximum amplitude peak at frequency 1.19981×10^{-3}Hz$\pm2.5\times10^{-7}$Hz, i.e. a period of 833.464±0.176s. The 1st and 2nd harmonics of this frequency were also present as significant peaks.

The complete results are given in Table 4.1 for those signals identified as significant at the 90% confidence level. The amplitude spectra, and window functions for the *RXTE* and *ASCA* are shown in Figure 4.1 along with the spectra prewhitened with the frequencies of the significant power peaks. The residual power peaks in the prewhitened *RXTE* periodogram pertain to the 3rd harmonic of the spin period ($>$ 68% confidence level) and the 1st and 2nd harmonics (<68% confidence level).

The rate of change in the spin period, $\dot{P} = +1.1 \times 10^{-10}\text{s s}^{-1}$, (Section 2.2.1.4) derived from the quadratic spin ephemeris, was used to check the consistency of these periods with that calculated by Mason (1997). The maximum amplitude peaks from both sets of data were found to be entirely consistent.

From the relationship $1/P_{beat} = 1/P_{spin} - 1/P_{orb}$ (Patterson, 1994) and using an orbital period of 5.19hrs (Hellier et al. 1994) a beat period at 14.54 min was to be expected. However, there was no significant evidence for a strong amplitude at

satellite	instrument	passband keV	frequency mHz	period s	S/N
ASCA	SIS1	0.7-10.0	$1.19981 \pm 2.5 \times 10^{-4}$	833.464±0.176	7.996
			$2.39994 \pm 3.2 \times 10^{-4}$	416.678±0.056	7.095
			$3.60019 \pm 3.2 \times 10^{-4}$	277.763±0.025	6.561
RXTE	PCA	2.0-25.0	$1.199703 \pm 8.1 \times 10^{-5}$	833.540±0.056	12.761

Table 4.1: The details of the significant power peaks found from period analysis of *ASCA* SIS1 data and *RXTE* pca data. The signal-to-noise ratio was taken as the amplitude of power peak to the mean of the prewhitened spectrum. The details of the analysis are given in Sections 3.3.1 and 4.2.1.

the frequencies corresponding to the orbital or beat periods in either the *RXTE* or the *ASCA* data.

4.2.2 Modulation

4.2.2.1 ASCA light curves

Light curves of the *ASCA* data were first presented in Mason (1997) and also in James et al. (1998). Their spin phase folded profiles for the passbands 0.7–1.0 keV, 1.0–2.0keV and 4–10keV are very similar to those from the 'hard' *ROSAT* band and the softer end of the *Ginga* bands (Figure 2.1); i.e. they show a asymmetric quasi-sinusoidal variation at higher energies, comparable to that seen in the *Ginga* 10–18 keV light curve, which becomes increasingly distorted towards lower energies due to the interception of "the dip" (Mason 1997). Light curves using data from the SIS0 detector for energy bands 0.7–1.0keV, 1.0–2.0keV, 2.0–4.0keV, 4.0–10.0keV and 0.5–10.0keV folded (Section 3.1.3) on spin period (Equation 2.1, Section 2.2.1.4) are

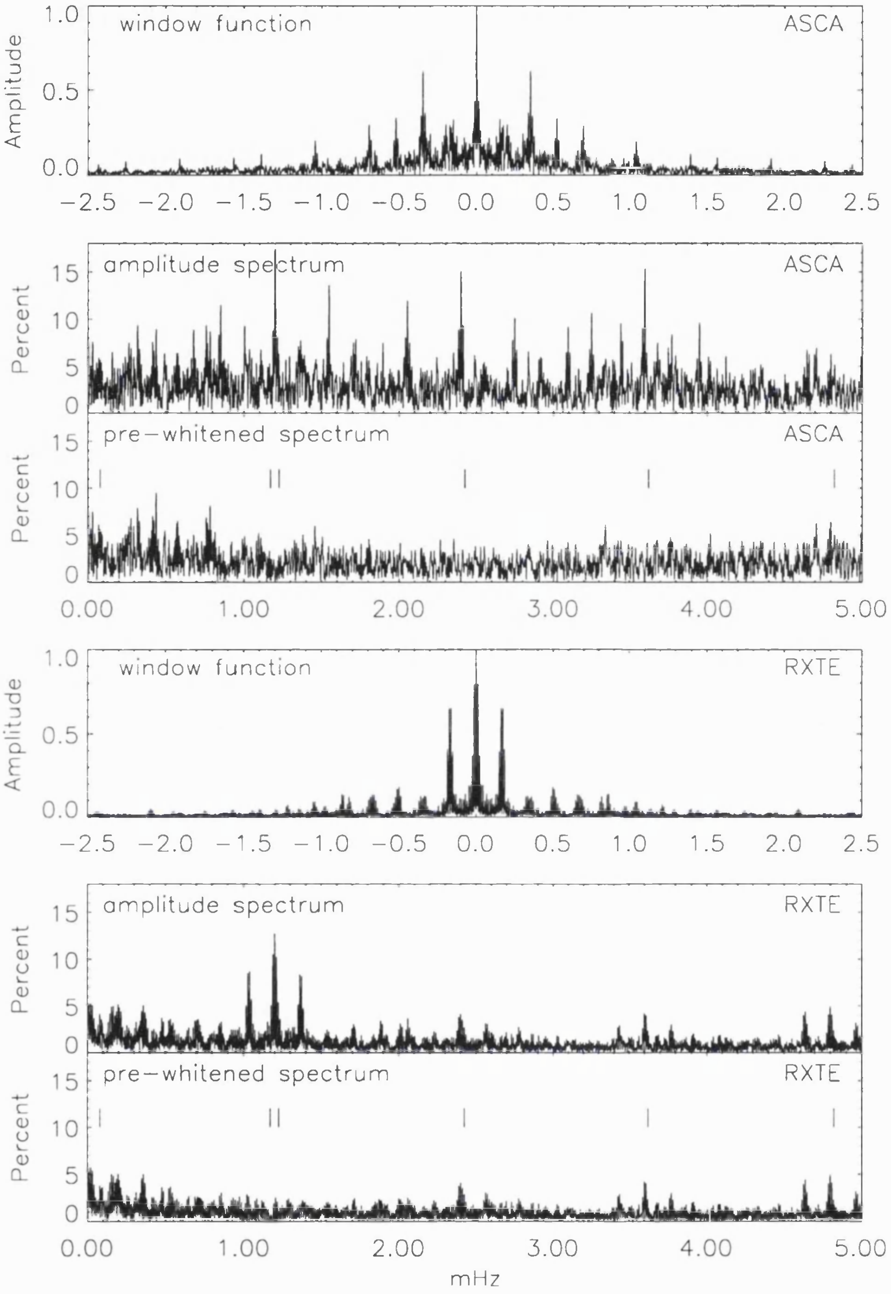

Figure 4.1: Periodograms calculated from the *ASCA* 0.5–10.0keV light curve (upper half) and *RXTE* 2.0–25.0keV light curve (lower half) of PQ Gem. In each case the plot shows (at the top) the window function for the amplitude spectrum (middle plot) and the spectrum pre-whitened with the frequencies of the significant peaks (bottom plot). The vertical bars (from left to right) mark the position of the orbital, beat and spin (ω) frequencies plus the 1st, 2nd and 3rd harmonics of ω, respectively. The relevant details are given in Section 4.2.1 and Table 4.1.

shown on the left-hand side of Figure 4.2.

4.2.2.2 RXTE light curves

Light curves were extracted for the energy bands 2.0–4.0keV, 4.0–10.0keV, 8.0–25.0keV and 2.0–25.0keV of the *RXTE* data and folded (Section 3.2.3) on the spin period (Section 3.1.3). These are shown on the right-hand side of Figure 4.2. The first two can be compared directly with the plots using the *ASCA* data in the same energy bands.

4.2.2.3 Comparison between the ASCA and RXTE folded light curves

The *RXTE* PCA instrument overlaps the *ASCA* SIS instruments across the 2–10keV energy band. Hence this energy band from both instruments was used to look for differences in the light curve modulation between the two observations (Figure 4.2). The light curves of these 2 bandpasses were found to be very similar, each with two maxima separated by a minimum at phase ~ 0.0 (referred to as "the dip", Mason et al. 1992) and a second minimum at ~ 0.6. In the 4.0-10.0keV light curves the minima are relatively shallow in both the *ASCA* and the *RXTE* light curves, but the 2.0-4.0keV light curves show well defined "dips" at phase 0.0, with a broader minimum at phase ~ 0.6. There is some evidence that the amplitude of the variation in the *RXTE* folded light curve is less than that in the *ASCA* SIS data. The shape of "the dip" in the 2.0-4.0keV band is V-shaped in the *RXTE* compared to a more U-shape in the *ASCA* light curve and its depth appears greater in the latter. This may be due to a higher level of absorption at the earlier epoch of the *ASCA* observation (although it might also be due to the difference in the effective efficiencies of the two detectors).

4.2.2.4 RXTE hardness ratios

A plot of the hardness ratio 8.0–25.0keV/2.0–8.0keV over the spin period is shown in Figure 4.3. The lower limit of the 8.0–25.0keV energy band was chosen so as to be above the main absorption edges, the highest of which is the Fe I K edge at 7.111keV

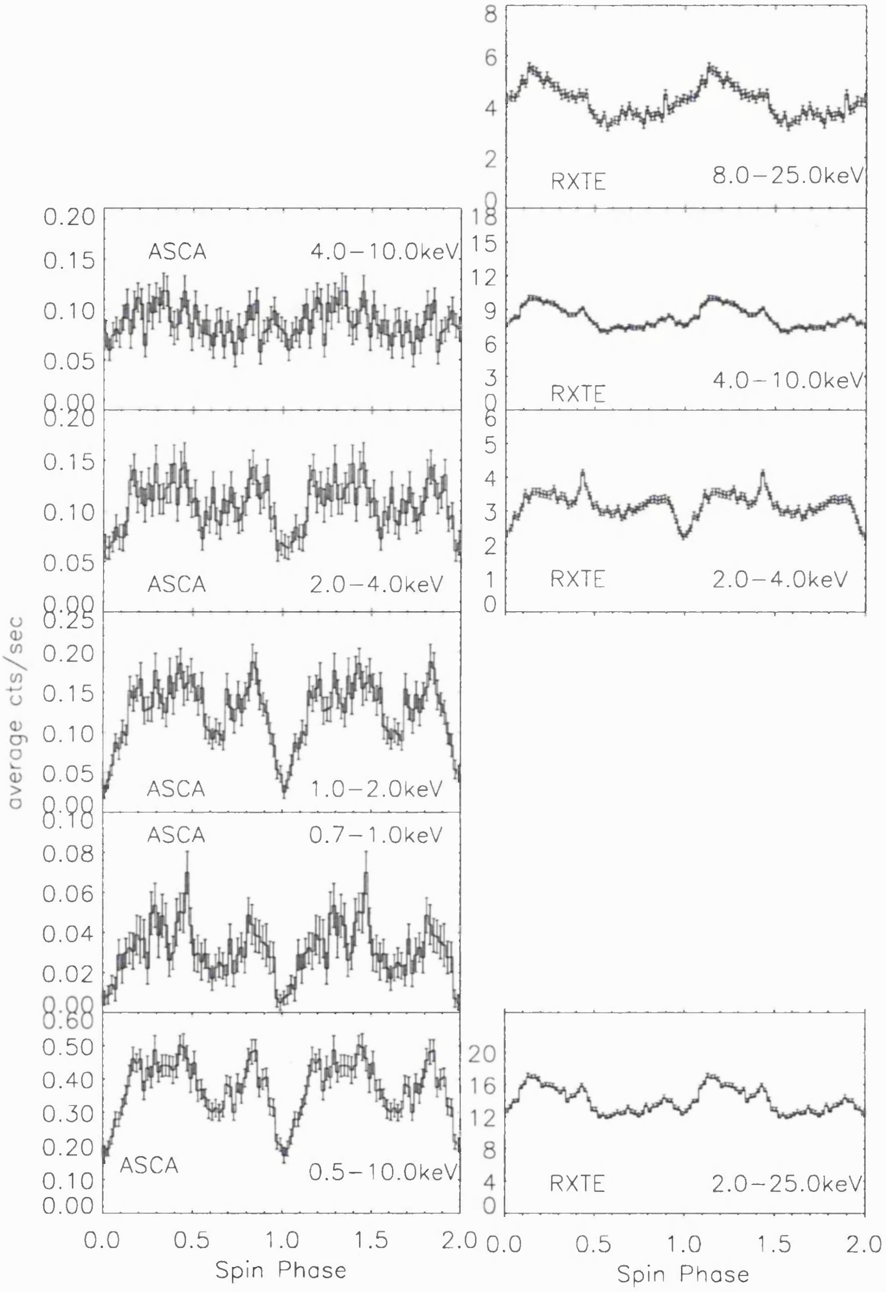

Figure 4.2: Background subtracted light curves of PQ Gem using *ASCA* SIS0 and *RXTE* PCA data folded on the spin period. On the left-hand side are the *ASCA* light curves for energy bandwidths 4.0–10keV (top), 2.0–4.0keV (second from top), 1.0–2.0 keV (middle) and 0.7–1.0keV (second from bottom) 0.5–10.0keV (bottom). On the right-hand side are the *RXTE* light curves for energy bandwidths 8.0–25.0keV (top), 4.0–10.0keV (second to top), 2.0–4.0keV (third from top) and 2.0–25.0keV (bottom).

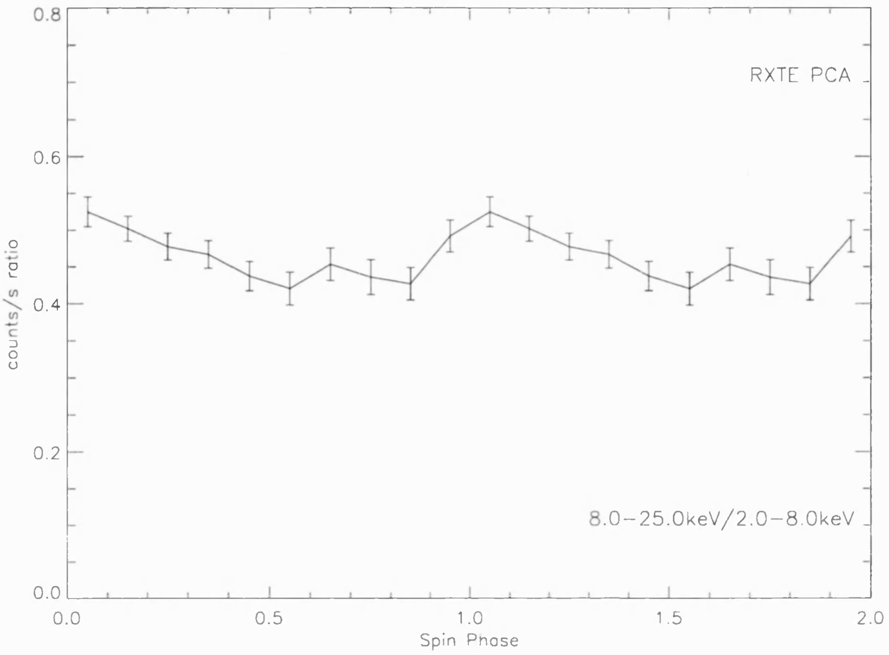

Figure 4.3: Plot of the *RXTE* 8.0–25.0keV/2.0–8.0keV hardness ratio for PQ Gem folded on the spin period. The errors are calculated to the 1σ level.

(Zombeck 1990). A higher value of the ratio indicates those positions in the spin cycle which are more affected by absorption. The variation in the hardness ratio over the spin cycle matches well that of the covering fraction of the partial absorber illustrated in Figure 4.5 (Section 4.3.2.2).

4.3 Spectral Analysis

4.3.1 The Integrated Spectrum

The emission of the integrated spectrum was analysed using an optically thin emission model for the hard X-ray spectrum and a blackbody model for the soft X-ray continuum (Section 3.3.2.2). The temperature of the former was difficult to constrain, a typical IP problem (Section 1.3.4) which was similarly experienced by Duck et al. (1994) with the *ROSAT* data (Section 2.2.3). Therefore the temperature was fixed at 20keV in line with the results from their analysis. The passband of *ROSAT*

N_{H_1} 10^{22} cm^{-2}	N_{H_2} (fraction) 10^{22} cm^{-2}	BB norm: 10^{-3}	MEKAL norm: 10^{-2}	Gaussian norm: 10^{-5}	Abundance Solar	flux(obs) 2-10keV 10^{-11}erg cm^{-2} s^{-1}	χ^2_ν (dof)
$0.13^{0.16}_{0.11}$	$10^{12}_{9.1}$ ($0.55^{0.57}_{0.54}$)	$2.9^{4.3}_{1.6}$	$2.0^{2.1}_{1.9}$	$4.7^{5.8}_{3.7}$	$0.31^{0.44}_{0.17}$	2.12	1.02 (1069)

Table 4.2: Results from spectral analysis of the *ASCA* integrated spectrum of PQ Gem including the error range at 90% confidence level. The optically thin plasma and blackbody temperatures were fixed at 20keV and 55eV respectively. N_{H_1} corresponds to the homogeneous absorber (wabs) whereas N_{H_2} applies to the inhomogeneous (partial covering) absorber. The normalisations are as the standard for the blackbody, Mekal and Gaussian *xspec* models used (Section 3.3.2.2) and the flux is not corrected for absorption. The model was fitted simultaneously to the medium and high bit rate data from the SIS1 and SIS0 instruments and the high bit rate data from the GIS2 instrument.

extends to soft X-rays (0.1–2.0keV), hence the temperature of the blackbody component was fixed at 55eV, in line with the results of Duck et al. (1994) (Section 2.2.3). The flourescent iron line at 6.4keV was modelled using a Gaussian component the width of which was fixed at 0.05keV (Section 3.3.2.2). Two components were used to model attenuation of the X-rays, a homogeneous (wabs) and an inhomogeneous (partial covering) photoelectric absorbers(Section 3.3.2.2).

During the spectral analysis the medium and high bitrate SIS data from both instruments and the GIS data were linked through the models and fitted simultaneously. A good fit to the data was achieved with this model ($\chi^2_\nu = 1.02$). The values of those parameters allowed to vary during the fitting are given in Table 4.2 and the integrated spectra are plotted in Figure 4.4.

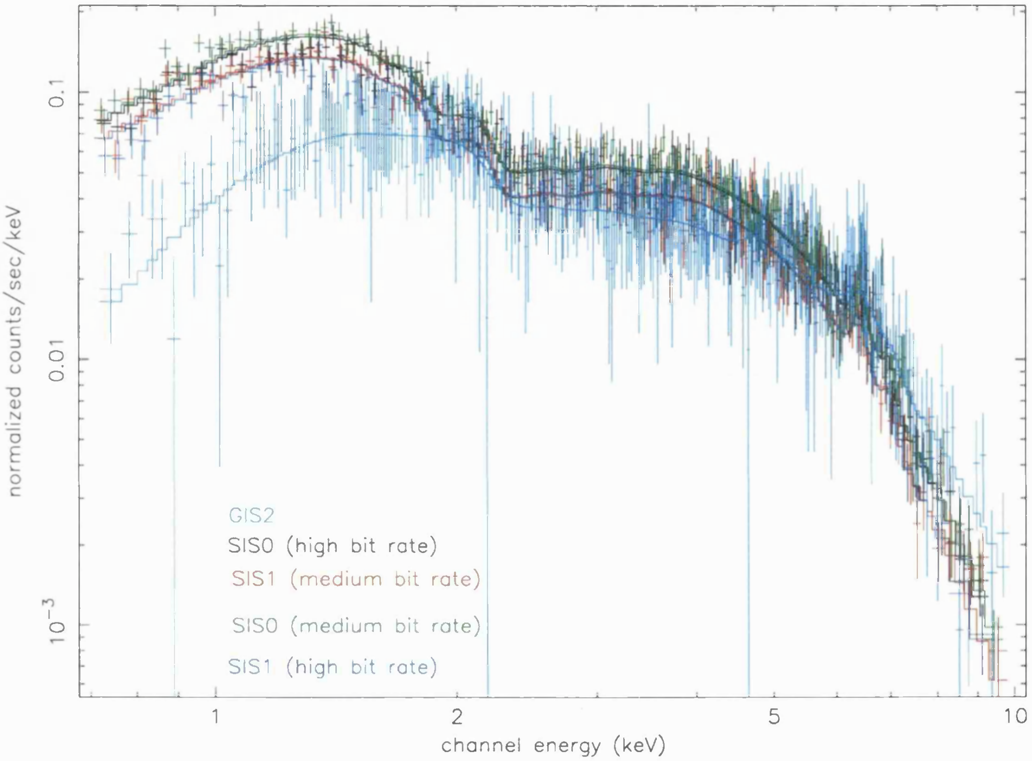

Figure 4.4: Integrated spectra of PQ Gem. Data from the medium and high bit rate data from the SIS1 and SIS0 instruments and the high bit rate data from the GIS2 instrument with the fitted model (Table 4.2).

Because the energy resolution of the *RXTE* PCA data (18% @ 6.0keV) is much poorer than that of the *ASCA* SIS (2%), spectral analysis was restricted to the *ASCA* data.

4.3.2 Phase-resolved spectroscopy

4.3.2.1 4 Bins

Phase-resolved spectral analysis was carried out using the *ASCA* data. A similar stategy to that of Duck et al. (1994) was adopted, in anticipation that the increase in spectral resolution and effective area of *ASCA* over other instrumentation would be sufficient to clarify the previous ambiguities (Section 2.2.3).

Data was extracted (Section 3.1.3) for spin phases 0.12–0.54 (maximum) , 0.54–0.77 (minimum), 0.77–0.91 (2nd maximum) and 0.91–1.12 ("the dip"). A model (similar components to that derived from the analysis of the integrated spectrum) was fitted to the data for phase 0.12–0.54 and the best fit parameters obtained to provide a reference model. The hard and soft X-ray temperatures were fixed at 20keV and 55eV, respectively (as for the integrated spectrum) and attenuation of the X-rays was modelled by both a homogeneous (wabs) and inhomogeneous (partial covering) absorption components. Spectral fitting of this model to the data gave a $\chi^2_\nu = 1.14$ with relative solar abundance at $0.67^{0.93}_{0.44}$ and the wabs column density at $\mathrm{N}_{H_2} = 5.76^{7.95}_{3.52} \times 10^{20}$ cm^{-2}. The remainder of the fitted parameter values are given in the first row of Tables 4.3–4.4. The addition of a Gaussian at 6.4keV had a detrimental effect on the fit so it was omitted from the final model. This reference model was fitted to the remaining 3 phases in a series of 3 spectral fits during which all the parameters except those pertaining to normalisation and/or inhomogeneous absorption were fixed; thus representing the scenarios of light curve modulation by self-occultation of the emission regions alone, by absorption alone or by a combination of the two (Section 3.3.3). These results are given in Tables 4.3 to 4.5. Taken in isolation the results are no more conclusive than those of Duck et al. (1994) as judged from a comparison of the χ^2_ν obtained. It is clear, though, that "the dip"

phase	BB norm: 10^{-4}	MEKAL norm: 10^{-2}	flux 2–10keV 10^{11}erg cm^{-2} s^{-1}	χ^2_ν (dof)
max:flux (ϕ 0.12–0.54)	$6.0^{7.1}_{4.8}$	$2.17^{2.33}_{2.03}$	2.46	1.14 (725)
minimum flux (ϕ 0.54–0.77)	$6.5^{8.0}_{4.7}$	$1.97^{2.00}_{1.94}$	2.23	1.05 (434)
2nd maximum flux (ϕ 0.77–0.91)	$6.7^{8.9}_{4.0}$	$2.20^{2.25}_{2.16}$	2.50	1.35 (331)
"the dip" (ϕ 0.91–1.12)	$4.2^{6.1}_{1.6}$	$1.60^{1.64}_{1.57}$	1.82	1.82 (353)

Table 4.3: Results from simultaneously fitting medium and high bitrate data from both SIS instruments and the medium bitrate data from the GIS2 instrument. The normalisation alone was allowed to vary from the values obtained from the spectral fits to the spin phase maximum data. The blackbody and Mekal normalisations are standard for the *xspec* models (Section 3.3.2.2) and the flux is not corrected for absorption.

phase requires absorption.

In Section 4.2.2.3 it was established that the folded light curves of *ASCA* and *RXTE* data for their overlapping energy range (2.0–10.0keV) showed great similarity. Hence it is reasonable to assume that the *RXTE* 8.0–25.0keV light curve which lies above the main absorption edges is also a good representation of PQ Gem's high energy light curve at the time of the *ASCA* observation. In addition, the probability of a variation in absorption over the spin cycle is indicated by the *RXTE* hardness ratio (Section 4.2.2.4) which shows a notable level of fluctuation during the spin period (Figure 4.3). Hence it was credible that the correct interpretation of the spectral analysis results was an interplay between varying absorption and visibility of the emission region, i.e. Table 4.5.

phase	N_{H_2} 10^{22} cm^{-2}	fraction	flux 2–10keV 10^{11}erg cm^{-2} s^{-1}	χ^2_ν (dof)
maximum flux (ϕ 0.12-0.54)	$7.6^{9.0}_{6.4}$	$0.56^{0.58}_{0.54}$	2.46	1.14 (725)
minimum flux (ϕ 0.54-0.77)	11^{13}_{10}	$0.58^{0.59}_{0.57}$	2.27	1.05 (434)
2nd maximum flux (ϕ 0.77-0.91)	$7.9^{9.2}_{6.8}$	$0.54^{0.56}_{0.53}$	2.47	1.34 (331)
"the dip" (ϕ 0.91-1.12)	$6.7^{7.6}_{6.4}$	$0.72^{0.73}_{0.72}$	2.31	1.19 (353)

Table 4.4: Results from simultaneously fitting medium and high bitrate data from both SIS instruments and the medium bitrate data from the GIS 2 instrument. The absorption alone was allowed to vary from the values obtained from the spectral fits to the spin phase maximum data. The blackbody and Mekal normalisations are standard for the *xspec* models (Section 3.3.2.2) and the flux is not corrected for absorption.

4.3.2.2 10 Bins

The possibility of a more complex variation in absorption over the spin cycle prompted further spin phase-resolved spectroscopy. The spin period was divided into 10 equal time bins and spectra extracted for each using data from both the SIS and GIS2 instruments. Only a single set of spectra were viable from the GIS instruments due to a technical problem. During all subsequent spectral fitting the medium and high bit rate data from both SIS and the GIS2 instruments were linked through the models and fitted simultaneously.

A similar approach to that used for the 4-bin phase-resolved spectroscopy was adopted. Spin phase 0.4–0.5 was chosen as the reference phase, since it had marginally the greatest number of counts. A similar model to that derived from the integrated spectrum was fitted to the data for this phase to determine the reference model, but with the difference that, in this case, the blackbody temperature was fitted. The final best fit parameters comprised of blackbody and optically thin plasma emission components with temperatures of 83eV and 20keV (fixed), respectively,

phase	N_H 10^{22} cm^{-2}	fraction	BB norm: 10^{-4}	MEKAL norm: 10^{-2}	flux 2–10keV 10^{-11}erg cm^{-2}s^{-1}	χ^2_ν (dof)
maximum flux (ϕ 0.12-0.54)	$7.6^{9.0}_{6.4}$	$0.56^{0.58}_{0.54}$	$6.00^{7.14}_{4.85}$	$2.17^{2.33}_{2.03}$	2.46	1.14 (725)
minimum flux (ϕ 0.54-0.77)	$8.1^{10}_{6.2}$	$0.54^{0.57}_{0.51}$	$5.99^{7.47}_{4.21}$	$1.93^{2.07}_{1.80}$	2.18	1.04 (432)
2nd maximum flux (ϕ 0.77-0.91)	$5.8^{7.9}_{4.3}$	$0.51^{0.54}_{0.47}$	$5.37^{7.89}_{3.41}$	$1.99^{2.14}_{1.86}$	2.38	1.34 (329)
"the dip" (ϕ 0.91-1.12)	$6.3^{7.3}_{5.4}$	$0.72^{0.73}_{0.70}$	$10.3^{13.8}_{6.40}$	$2.08^{2.21}_{1.97}$	2.27	1.18 (351)

Table 4.5: Results from simultaneously fitting medium and high bitrate data from both SIS instruments and the medium bitrate data from the GIS 2 instrument. Both the normalisation and the absorption factors were allowed to vary from the values obtained from the spectral fits to the spin phase maximum data. The blackbody and Mekal normalisations are standard for the *xspec* models (Section 3.3.2.2) and the flux is not corrected for absorption.

a Gaussian at 6.4keV (fixed) with a fixed width at 0.05keV (Section 3.3.2.2), a metal abundance of 0.34 relative to the solar abundance, a cold inhomogeneous (partial covering) and a homogeneous (wabs) absorption components; this latter gave an equivalent hydrogen column density = 6.84×10^{20} cm^{-2}. The parameters of this reference model were fixed during the spectral fitting of the 9 remaining phase bins with exception of the inhomogeneous absorber (partial covering) and the normalisations for the hard X-ray, blackbody and emission line components.

The resulting best fit parameter values from this analysis are shown in Table 4.6 from which the variations in the optically thin plasma normalisation, the column density and partial covering fraction are plotted in Figure 4.5 as well as the folded light curve for the 0.5–10.0keV energy band of the *ASCA* data. It can be seen that the column density (within its rather large error bounds) does not vary over the whole spin cycle. The normalisation parameter of the hard X-ray component shows a maximum over spin phases 0.2–0.4, decreasing to a minimum at phase 0.7. The covering fraction of the partial absorber component shows a steady decline from its maximum value at phase 0.0 to a minimum value at spin phase 0.5. This pattern and phasing closely follows that of the *RXTE* 8.0–25.0keV/2.0–8.0keV hardness ratio, Figure 4.3.

Relating this back to the main features of the modulation of the light curve shows that the maximum countrate (spin phases 0.1–0.4) is due to a combination of increasing normalisation coupled with a decreasing level of absorption. It would appear that an increase in the normalisation factor is probably the main cause of the second maximum (phases 0.75–0.85) of the light curve, but a contribution from a decrease in the covering fraction may also play a part. The secondary minimum (spin phases 0.55–0.75) is mainly due to a lower normalisation factor. Finally, "the dip" can be accounted for by the maximum value of the covering fraction, although, again, a contribution from a slight decrease in the normalisation factor cannot be ruled out. Nevertheless, the interpretation of these results does depend, to some extent, on the correctness of the conclusion drawn at the end of Section 4.2.2.1 that the light curve modulation is due to a combination of absorption and visibility of the emission regions (refer to Section 4.5.3 for a fuller discussion).

4.4 The Mass of the White Dwarf

4.4.1 The Technique

Both the *ASCA* and the *RXTE* data were used to estimate the mass of the white dwarf using the stratified-accretion-column model of Cropper et al. 1999b, i.e. the version of their model which took into account the effects of gravitational variation within the shocked gas and a mean molecular mass of the plasma appropriate to a cosmic abundance rather than that of hydrogen. Each estimate was confined to data from a single instrument due to the reported sensitivity of the model to instrumental bias (Ramsay et al. 1998).

The parameter, ϵ_{s_0} (the ratio of the bremsstralung to cyclotron cooling, Section 3.3.2.2), was fixed at 0.5, because this figure approximated to a magnetic field strength of 15MG (Section 2.2.1.3) at a specific accretion rate of 1.0 g cm^{-2} s^{-1} and a white dwarf mass of 1M$_\odot$ (figure 1b, Wu et al. 1995). Where feasible the data was restricted to spin phase 0.1–0.5 inclusive; this selection was based on consideration of that part of the spin cycle which corresponded to the visibility of a single emission site as depicted in Figure 4.6. The viability of this choice was supported by the strong similarities found between the *RXTE* and *ASCA* light curves (Section 4.2.2.3) and the correspondence in phasing of the *RXTE* hard X-ray light curves with the results from the cyclotron modelling of Potter et al. (1997) for these spin phases (Section 4.5.3). This situation also lead to an estimate for the viewing angle of 64° (Section 3.3.2.2). A distance of 400pc (Section 2.2.1.2) was adopted and the number of stratifications between the white dwarf surface and the level of the shock front was set to 100. The free parameters during the spectral fitting were the accretion rate, the radius of the accretion column and the mass of the white dwarf. The abundance

spin phase	N_{H_2} 10^{22} cm^{-2}	covering fraction	BB norm: 10^{-4}	MEKAL norm: 10^{-2}	Gaussian: norm: 10^{-5}	flux(obs) 2–10keV 10^{-11}erg cm^{-2} s^{-1}	χ^2_ν (dof)
0.0-0.1	$7.4^{8.9}_{5.9}$	$0.80^{0.82}_{0.78}$	$0.48^{1.51}_{0.00}$	$1.88^{2.09}_{1.70}$	$7.96^{10.9}_{1.63}$	1.86	1.09 (149)
0.1-0.2	$8.6^{11}_{6.4}$	$0.70^{0.73}_{0.66}$	$1.62^{2.19}_{1.02}$	$2.10^{2.36}_{1.88}$	$11.9^{15.1}_{6.26}$	2.17	1.00 (198)
0.2-0.3	$5.4^{7.9}_{4.1}$	$0.59^{0.62}_{0.56}$	$1.24^{1.75}_{0.70}$	$2.22^{2.42}_{2.06}$	$12.7^{15.9}_{7.01}$	2.59	1.11 (248)
0.3-0.4	$5.7^{7.9}_{4.2}$	$0.55^{0.58}_{0.51}$	$1.63^{2.08}_{0.99}$	$2.21^{2.42}_{2.04}$	$7.77^{12.3}_{3.56}$	2.55	0.91 (245)
0.4-0.5	$8.1^{12}_{5.4}$	$0.47^{0.53}_{0.42}$	$1.16^{1.71}_{0.78}$	$2.18^{2.46}_{1.98}$	$8.00^{11.5}_{2.91}$	2.49	1.12 (253)
0.5-0.6	$3.8^{5.8}_{2.3}$	$0.43^{0.47}_{0.39}$	$1.47^{2.02}_{1.04}$	$1.79^{1.96}_{1.65}$	$7.02^{9.70}_{1.08}$	2.23	1.08 (241)
0.6-0.7	$6.9^{11}_{4.3}$	$0.54^{0.59}_{0.48}$	$0.58^{1.06}_{0.23}$	$1.69^{1.92}_{1.52}$	$11.7^{15.0}_{6.28}$	1.96	0.98 (202)
0.7-0.8	$4.0^{5.9}_{2.7}$	$0.52^{0.55}_{0.48}$	$0.65^{1.14}_{0.29}$	$1.61^{1.74}_{1.49}$	$6.69^{10.2}_{2.80}$	1.96	0.99 (209)
0.8-0.9	$8.1^{12}_{5.36}$	$0.50^{0.55}_{0.45}$	$0.52^{0.99}_{0.06}$	$1.99^{2.19}_{1.81}$	$4.21^{8.19}_{0.15}$	2.23	1.04 (231)
0.9-0.0	$4.8^{6.3}_{3.7}$	$0.58^{0.61}_{0.55}$	$1.42^{1.90}_{0.87}$	$1.87^{2.03}_{1.75}$	$11.8^{15.0}_{6.56}$	2.2	0.95 (218)

Table 4.6: The variable parameter values from spin phase-resolved spectral analysis over 10 phase-bins. The reference model (phase 0.4–0.5) was simultaneously fitted to the medium and high bitrate data from both of the SIS instruments and high bitrate data from the GIS2 instrument on the *ASCA* satellite. The normalisation and absorption parameters only were varied from those of the reference model. The blackbody, bremssstralung normalisations and absorption include the error range at the 90% confidence level. The blackbody, Mekal and Gaussian normalisations are standard for the *xspec* models (Section 3.3.2.2). Also included are the χ^2_ν and observed flux (i.e. not corrected for absorption) for the 10 phases.

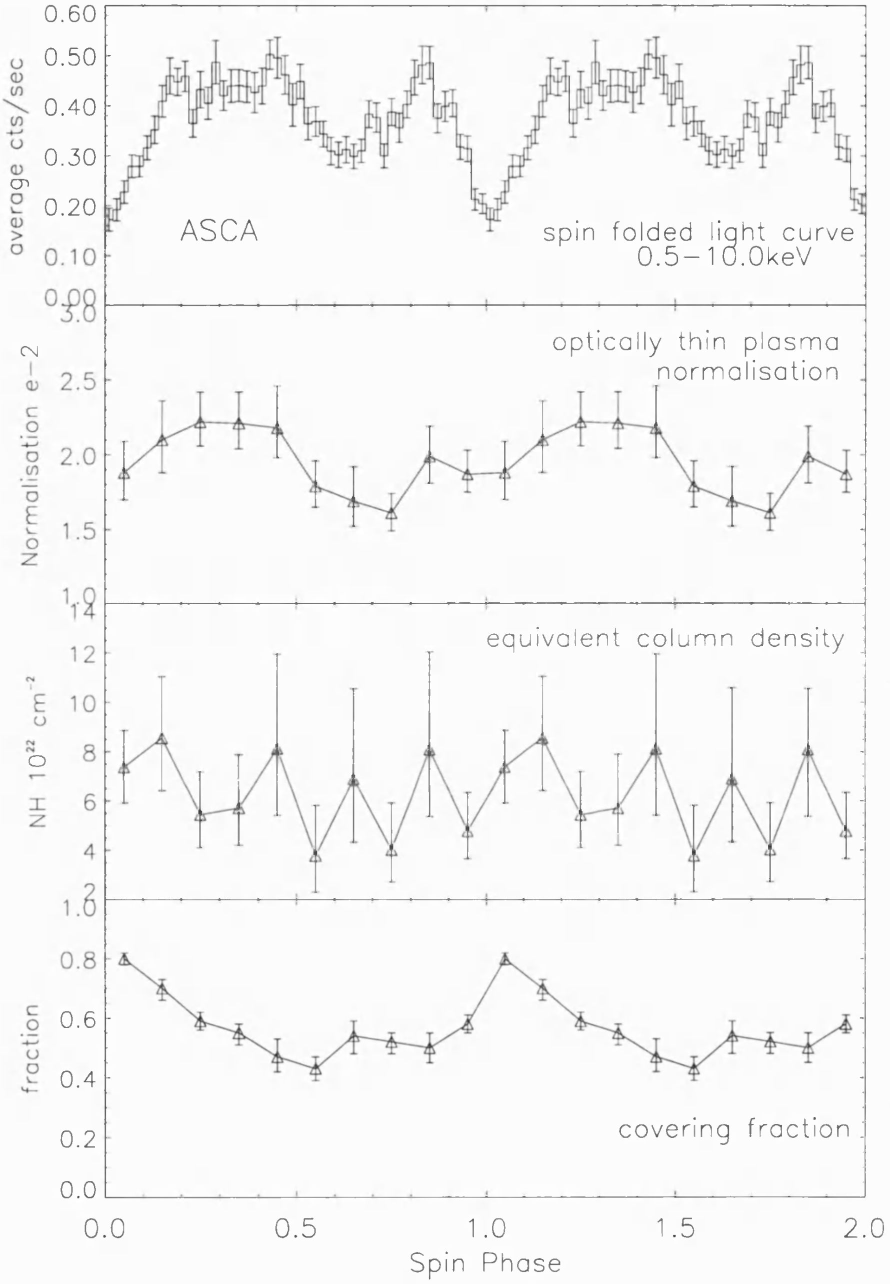

Figure 4.5: Plots showing the results from 10-bin spin phased-resolved spectroscopy of *ASCA* data. Phase 0.4–0.5 is the reference spin phase. The plots from the top are the spin folded light curve included for clarity, the variation in the hard X-ray normalisation, the column density of the partial covering absorber and its covering fraction.

was allowed to vary from a solar profile in the final stages of the fitting.

A range of absorption components were added to the emission model. These were homogeneous and inhomogeneous photoelectric absorbers and a partially ionised warm absorber (Section 3.3.2.2). The equivalent column density of the homogeneous absorber (wabs) was fixed at 7.0×10^{20} cm^{-2} (in line with the fitted value from the reference model for the 10-bin phase-resolved spectroscopy) for those models involving multiple absorber components. For the warm absorber the electron density was fixed at $\sim 10^{14}$cm^{-3} (Cropper 1990) and the temperature at 10^6K with the abundance and distance parameters linked with those of the emission model. Thus, for the warm absorber, the equivalent column density and the height of absorption above the white dwarf were left as free parameters.

4.4.2 The Results

The final model fitted to the *ASCA* data consisted of homogeneous (wabs) and inhomogeneous (partial covering) absorption components together with that of the stratified-accretion-column emission. Some of the parameters were fixed, as stated in Section 4.4.1. A successful fit could be obtained only if the data was restricted to energies $\geq$4.0keV: this was probably due to the complex absorption characteristics of the source (Cropper et al. 1999b). Therefore, it was not possible to restrict the data to phase 0.1–0.5, because of insufficient statistics. Even so the values obtained for the mass of the white dwarf were highly unconstrained (Table 4.7).

The final model for the *RXTE* data consisted of a homogeneous absorber (wabs) plus the stratified-accretion-column emission component with the data restricted to phase 0.1–0.5. Estimates for the white dwarf mass with reflection effects set for a viewing angle of 64° and at both maximum and minimum (for completeness) are given in Table 4.7. The entries in this Table also cover the values of those model parameters which were free to vary during the spectral fitting.

Other models which incorporated different absorption components were evaluated by fitting them to the *ASCA* and the *RXTE* data, but these gave poor results. Those models which included the warm absorber (Section 3.3.2.2) gave inadequate

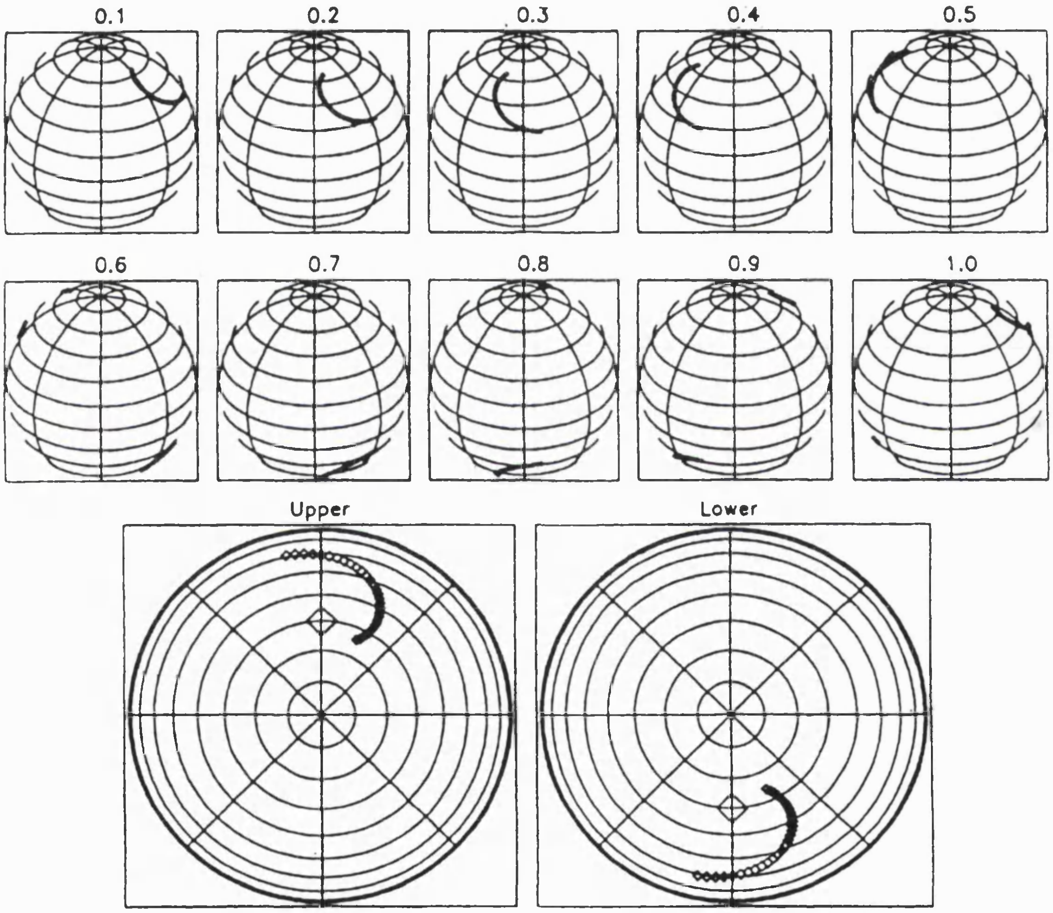

Figure 4.6: Figure 2.2 repeated here for the convenience of the reader. Illustration of the upper and lower accretion arcs on the surface of the white dwarf as computed from cyclotron modelling of PQ Gem (Section 2.2.2.2) at consecutive phases of the spin period. The bottom two globes give the view as seen from directly above the top and bottom poles respectively. The diamonds mark the magnetic poles. Reproduced from figure 9 of Potter et al. (1997).

outcomes when fitted to the *ASCA* SIS data (χ^2_ν at 1.27–1.43) and the *RXTE* data (χ^2_ν ~1.8). In this latter case data was included from the whole spin cycle, but those in the 6.0–7.5keV energy band were excluded. This was found to be necessary due to poor fits of the model to the data around the Fe Kα emission line complex. Elimination of these energies was not expected to have a detrimental effect on the estimate of the M_{WD} (Ramsay 2000). This data selection was also fitted to a model comprising of a cold homogeneous absorption (wabs) component and the stratified-accretion-column emission component, i.e. similar to the successful model (Table 4.6). Again the results were unacceptable with $\chi^2_\nu = 2.35$ and 1.99 for viewing angles of 90° and 0° respectively.

The unconstrained values obtained for the white dwarf mass using the *ASCA* SIS data can probably be accounted for by the lack of spectral response of *ASCA* instrumentation in the energy band corresponding to the temperature of the shock in PQ Gem (Ramsay 2000). Complex absorption effects were thought to be a contributary factor to the predominance of poor fits to this data when energies below 4.0keV were included in the fitting process (Ramsay 2000). Trials with the data limited to spin phases 0.21–0.91 (i.e. excluding "the dip") gave unacceptably high χ^2_ν (1.27–1.7) when fitted to a model consisting of a partial covering absorption and a stratified-accretion-column emission components. On the other hand, fitting the GIS data to a model which included both cold inhomogeneous and a warm absorbers gave very low χ^2_ν (~0.55–0.7) with unconstrained values for the mass, which is indicative that the errors were probably dominating (Section 3.3.2.2); so in consequence the GIS data was excluded from further estimates.

4.5 Discussion

The aim of this work has been to use the results from X-ray spectroscopy to throw further light on the origin(s) of the modulation demonstrated in the X-ray light curves. However, prior to considering the spectroscopy, an outstanding aspect related to the light curves is examined. This is preceded by a discussion of the results from

Satellite	detector	angle °	$N_{H_1,cold}$ 10^{22} cm^{-2}	$N_{H_2,cold}$(fraction) 10^{22} cm^{-2}	mdot gcm^{-2}s^{-1}	WD mass $M_\odot$	χ^2_ν (dof)
ASCA	SIS1	90	0.07 (fixed)	88 (0.69)	2.42	1.24 ($>$ 0.69)	1.04 (84)
		0	0.07 (fixed)	86 (0.69)	2.41	1.20 ($>$ 0.69)	1.03 (85)
	SIS0	90	0.07 (fixed)	35 (0.49)	2.08	1.24 ($>$ 0.79)	1.20 (99)
		0	0.07 (fixed)	35 (0.49)	2.40	1.23 ($>$ 0.76)	1.19 (100)
RXTE	PCA	90	4.6		2.08	1.27 (1.20-1.32)	1.04 (46)
		64	5.2		2.32	1.21 (1.16-1.28)	0.89 (46)
		0	5.2		2.29	1.18 (1.10-1.24)	0.81 (46)

Table 4.7: Results from fitting the stratified-accretion-column model of Cropper et al. (1999b) to both SIS data from the *ASCA* satellite and PCA data from the *RXTE* satellite. An integrated spectrum was extracted from the *ASCA* data, but restricted to the energy band 4.0–10.0keV; the spectrum extracted from the *RXTE* data covers spin phase 0.1–0.5. In this latter case the results encompass not only those with the reflection effects set to a maximum (0°) and a minimum (90°), but also from the preferred average viewing angle of 64°. Details of the spectral fitting process are given in Section 4.4.

the calculations of the mass of the white dwarf. Finally, the likelihood that the accretion stream continues over the accretion disc is appraised.

4.5.1 The Mass of the White Dwarf

The mass of the PQ Gem's white dwarf has been previously calculated using a stratified-accretion-column model fitted to *Ginga* data (Section 2.2.1.1). Ramsay et al. (1998) found that there was a good correspondence between the estimates given by *RXTE* data and those from eclipse mapping for the IP, XY Ari. This was thought to be due to the sensitivity of *RXTE* to a higher energy range than either *Ginga* or *ASCA* and hence was more compatible with the expected shock temperatures. In the work for this thesis it is found that the *RXTE* data give estimates which are very much better constrained than those made with the *ASCA* SIS data. The preferred estimate is $M_{WD} = 1.21\ M_{\odot}$ for PQ Gem, since this was obtained by specifying the average viewing angle to the site of reflection of 64°, based on other observational evidence. This value of M_{WD} corresponds well to that obtained with the *Ginga* data, fitted with the same emission model plus the warm ionised absorber component and allowing for maximum reflection effects. However, the estimate from *RXTE* data does have a much tighter constraint though it is still high in comparison to the mean mass of $M_{WD} = 0.85 \pm 0.21$ (Ramsay 2000).

4.5.2 Spin Pulse Modulation

The justification for the 10-bin phase-resolved spectroscopy was based on the similarity between the *ASCA* and *RXTE* 2–10keV spin-folded light curves (Section 4.2.2.3). and the *RXTE* hardness-ratio (Section 4.2.2.4). It was assumed that the former indicated that the *RXTE* light curves >10keV were also representative of PQ Gem at the time of the *ASCA* observations. The mapping of the emission regions to the rotational frame of the white dwarf through the cyclotron modelling of Potter et al. (1997) (Figure 4.6) makes this conjecture very much more robust: The spin folded 8.0-25.0keV *RXTE* light curve (Figure 4.2) is quasi-sinusoidal with a maximum countrate occuring at phase 0.1–0.2 and a minimum at phase ~ 0.5; this is entirely consistent with Figure 4.6 if one takes into account an augmented accretion rate at the leading edge of the emission region, as indicated by the plots of the upper and lower magnetic poles (the polar plots).

Comparison of the 8.0–25.0keV *RXTE* light curve and the variation in the normalisation (Figure 4.5) between phases 0.5 and 1.0 could be interpreted as a slight phase shift between the two. An explanation might be a minor change in the pattern of accretion between the two observations. On the other hand the slight differences may be due to comparison between disparate energy bands and/or spectroscopy accounting for spectral response of the instrument which is lacking in the light curves. Nevertheless, it is fair to say that not only is there a correspondence between the 2–10keV light curves of the *ASCA* and *RXTE* data (Section 4.2.2.3), but also that the hard X-ray light curve from the latter is consistent with the results of Potter et al. (1997) and the spectral analysis of the *ASCA* data, thus justifying the assumption made at the end of Section 4.3.2.1 that the modulation of the light curves of PQ Gem are caused by the combination of self-occultation of the emission regions and photoelectric absorption.

4.5.3 Accretion Model

The 10-bin phase-resolved spectroscopy begs the question as to a possible model to account for the results. The existence of variation in both absorption and normalisation is indicative that a standalone King and Shaviv model (Section 1.3.4) is inappropriate. The lack of evidence for either a beat or orbital X-ray pulse and the observed S-waves attributed to the impact of the stream onto the disc (Hellier 1997) renders the discless accretion model of Hameury et al. (1986b) (Section 1.3.4) unlikely. The hybrid occultation/absorption model (Section 1.3.4) could be applicable, except that it demands heavy absorption during the visibility of the lower emission region, phase 0.6–0.8; whereas, the results from the analysis for this thesis show reduced absorption at this phase (refer below and Section 4.5.4 for further discussion on absorption at this phase). In Section 4.2.1 it was shown that the fundamental and multiple harmonics of the spin period were present, at differing relative powers, at a significant level in the *ASCA* data; thus lending support to the accretion curtain model (Section 1.3.4) (Wynn & King 1992). However, Figure 4.5 shows the maximum of the covering fraction (absorption) to lead that of the normalisation by ~0.2 of the spin period whereas the accretion curtain model (Section 1.3.4) requires that an emission maximum and the absorption maximum are antiphased. Nevertheless, the work of Potter at al. (1997) also supports an accretion curtain (Figure 1.6) model along the lines suggested by Rosen et al. (1988) for the IP, EX Hya. Hence, the plausibility of this model is scrutinised further.

A summary description of the accretion curtain model as propounded by Rosen et al. (1988) is given in Section 1.3.4 and depicted in Figure 1.9. Whereas, Figures 1.8 & 1.6 illustrate the structure of an IP system with its truncated accretion disc and the curtain of accreting material from the inner edge of this truncated disc, respectively. The essential arguments for the development of the accretion curtain model hinged on the expected consequences of the oblique rotator accretion model on the changing optical depth of the accreting gas over the spin cycle. In this thesis, the modelling of the attenuation of the X-rays due to the opacity of the gas (Section 3.3.2.2) was accomplished through the equivalent neutral hydrogen column parameter of the absorption components. The lack of variation in this parameter of the partial covering absorber over the spin cycle of PQ Gem, together with the strong cyclic variation in the covering fraction of this component, means that the expectations for the attenuation in the accretion curtain model need to be re-assessed in terms of this latter parameter. The concept of a varying covering fraction can be understood in terms of fragmentation of the accreting material, and the expected correlation of fragment size (Section 1.2.2) along the accretion arc. Simple packing theory dictates that the smaller the radius of a set of spheres the greater the number of such spheres that can be packed into a given volume and the smaller the volume unoccupied by such spheres. Hence, one would expect that the phases of the spin cycle with the greatest covering fraction are associated with the the smallest fragments or "blobs" of material. Even so, it is to be expected that the viewing aspect to the curtain will effect the projected cross sectional area of the "blobs". In other words, those phases which give the longest path through the accretion curtain would also give the highest covering fraction for a given fragment size. Therefore, some correlation between optical depth effects and the covering fraction is to be expected.

A homogeneous distribution of material in the accretion curtain to the upper pole in an axisymmetric system (Figure 1.5) would result in a symmetric variation in the absorption about the midpoint so that its maximum and that of the normalisation of the optically thin hard X-ray emission would coincide. However, examination of the results, Figure 4.5, shows this not to be the case for PQ Gem, but rather the variation in the covering fraction (absorption) is asymmetric about a maximum at phase 0.0 whereas the maximum of the normalisation occurs between phase 0.1–0.4. This result reinforces the arguments for an oblique rotator accretion model.

The rapid increase in the absorption covering fraction between phase 0.9–1.0 can be equated to the appearance of the accretion material over the limb of the white dwarf (Figure 4.6). The strong magnetic field would ensure that the shock height is diminished by the efficient cooling afforded by cyclotron radiation(Section 1.2.2.1). The possible enhanced accretion rate at the leading edge of the accretion arc (Figure 4.6) implies that the quantity of absorbing material could also be augmented here. This would serve to further lower the height of the shock in this region together with a corresponding lengthening of the column of cool gas above the shock. In addition, the twisted magnetic field lines (Section 2.2.4) would serve to shift the occultation of the emission region by cool preshock gas by bringing the magnetic field lines more nearly along the line of sight (maximum attenuation) earlier in the spin cycle (Figure 2.3). Hence the absorption, at its maximum, could be contributed to by more absorbing material (both greater accretion rate and longer column of cool preshock gas) at the leading edge of the accretion arc together with considerations of the line of sight to this material. As the relative position of the upper accretion arc moves across the visible hemisphere of the white dwarf (Figure 4.6) phases 0.1–0.4, the covering fraction (Figure 4.5) decreases which is consistent with the diminishing accretion rate.

The twisted magnetic field line scenario put forward by Mason (1997) also required that the accretion curtain should clear the emission region by phase 0.1–0.2. The variation in the absorption, Figure 4.5, shows that this criterion is not met. On the other hand, Potter et al. (1997) argued that the field lines ahead of those directly below the magnetic pole are more favourably presented to the material threading them at the edge of the disc. Hence, the case for the twisted magnetic field lines is contentious, thereby throwing the viewing angle aspect into doubt. It could be that so long as the accretion rate is sufficiently augmented at the leading edge of the accretion curtain then the presentation of the magnetic field lines to the line of sight (within a few degrees) becomes of secondary importance. Allan et al. (1996) suggest that the larger and wider accretion areas of the IPs with lower magnetic field strengths do lead to a greater horizontal than vertical optical depth. However, though PQ Gem demonstrates the prerequiste double-peaked light curve (Norton et al. 1999), the observational evidence for circular polarisation belies a low magnetic field strength. Nevertheless, even if the magnetic field strength was lower than that deduced, the lack of variation in the column density and/or the profile and phasing of the modulation in the covering fraction (Table 4.5 & Figure 4.5) contravenes the expectations of the low magnetic field/fast rotator model.

Crucially, it is the covering fraction rather than the optical depth which is shown to vary over the spin cycle. Therefore, it is certainly conceivable that it is not the accretion rate, but the size of the "blobs" of material in the accretion curtain that is responsible for the structured accretion arc in Figure 4.6 and the observed variation in the covering fraction. In which case, its reduction during phases 0.1–0.4 would be accounted for by the increasing size of the "blobs" along the accretion arc. Hence, the approximate co-incidence of the maxima of the covering fraction and the normalisation (phase 0.0–0.2) may be accounted for by a partial transparency of accretion curtain ("blobby" accretion) which allows the emission from the upper accretion region to penetrate the veil of accreting material. The lack of a second maximum in the normalisation, 0.5 of the spin cycle later, may be due to the system geometry; Figure 4.6 suggests that the lower accretion arc is much less visible.

The timing of the increase in the covering fraction (Figure 4.5) at phase 0.6 is coincident with the emergence of the lower accretion arc (Figure 4.6), hence it may be due to the leading edge of the accretion curtain to the lower emission site appearing over the limb of the white dwarf. An alternative to this suggestion is the possibility that the emission is viewed through the strong photoelectric absorption from cool material in the preshock region. However, it is hard to visualize the feasibility of this suggestion given the oblique rotator geometry of this system.

4.5.4 Occultation by the Accretion Disc?

A further option for the increase in the covering fraction at phase 0.6 could be the interception of the inner edge of the truncated accretion disc, r_A (Figure 1.5), between the lower emission region and the line of sight of the observer. This possibility is now explored.

Using the Ghosh & Lamb formulation (Li, Wickramasinghe and Rudiger 1996) the radius to the truncated inner edge of the accretion disc is given by

$$r_A = .52\mu_{WD}^{4/7}(2GM)^{-1/7}\dot{M}^{-2/7}$$

where μ_{WD} is the magnetic moment of the white dwarf.

The magnetic moment can be estimated from the approximate relationship $B \sim \mu/r^3$ (spherical accretion). The mass of the white dwarf is estimated to be $1.21M_\odot$ (Section 4.4.2) which by using the mass/radius relationship of (Naurenberg 1972) leads to an estimated white dwarf radius, R_{WD}, of 3.8×10^8 cm. Hence by taking a value of 15MG (Section 2.2.1.3) as the magnetic field strength, B_{WD},

$$\mu_{WD} = B_{WD}R_{WD}^3 = 9.6 \times 10^{32} Gcm^3.$$

The accretion luminosity, L_{acc}, relationship (Frank, King and Raine 1992)

$$L_{acc} = GM\dot{M}/R_{WD}$$

where M is the mass of the white dwarf and L_{acc} is emitted mostly in the X-ray energy band, enables estimation of the accretion rate, $\dot{M}$.

The unabsorbed spectral model from the analysis of the integrated spectrum (Section 4.3.1) permits estimation of the X-ray flux at 1.24×10^{-10} erg cm^{-2} s^{-1} which, taking the distance of PQ Gem to be 400pc (Patterson 1994), gives a luminosity of 2.4erg s^{-1} and hence an accretion rate of 5.5×10^{15}g s^{-1}. Therefore $r_A = 1.7 \times 10^{10}$ cm or, in other words $\sim 45R_{WD}$. Hence, in a system with an angle of inclination of 60°, the line of sight to the white dwarf surface is clear of the accretion disc at all spin phases.

4.5.5 Disc Overflow?

Previous simulations of IPs generated light curves from a series of accretion models which included disc-fed (non-truncated disc), disc-fed (truncated disc), disc overflow and discless accretion (Norton 1993). Electron scattering, photoelectric absorption and self-occultation of the emission area were all included as contributors to the light curve modulation. Light curves were generated for both a filled circle and accretion arc geometry for a range of inclination (i) and magnetic axis offset (β) angles (Figure 1.7). The simulated light curve most closely resembling that of PQ Gem was generated from a disc overflow model (Section 1.2.2.2) for a high energy system ($\geq$ 20keV) with a system geometry of i=60° and β=30° (Section 2.2.1.5) in which electron scattering dominated. A disc overflow model has knowledge of both the binary and the white dwarf rotation frames. Hence a strong diagnostic for this type of accretion is the presence of a beat pulse in the power spectra, in particular the 2ω-Ω component (Wynn & King 1992). Such a signal was not found in the power spectra from either the *RXTE* or *ASCA* data which, thus, makes disc overflow unlikely. This conclusion is lent further weight by the lack of detection of a beat pulse in either the *ROSAT* or *Ginga* data (Mason et al. 1992, Duck et al. 1994). In Section 4.5.3 it was concluded that an accretion curtain model was the most likely and hence, it would appear that accretion via an accretion disc without disc overflow is the most probably sequence of events.

4.6 Finale

The analysis in this chapter has shown that the only periodic signal in X-ray data of PQ Gem is that of the spin period of the white dwarf plus its 1st and 2nd harmonics (*ASCA* data), thus indicating that the most probable accretion model is that of accretion through a truncated disc rather than disc overflow (Wynn & King 1992).

The outcome from the spectral analysis when coupled to the indications from the hard X-ray light curves and to previous results (Mason 1997; Potter et al. 1997) is strongly indicative that the light curve modulation is due to variation in both the emission and absorption components around the spin cycle and that the accretion is notably inhomogeneous. The profile of the absorption modulation is highly supportive of an accretion curtain model. The difference in this case to that proposed by Rosen et al. (1988) for Ex Hya is that the emission region points towards the observer with the interception of the accretion curtain along the line of sight at the light curve maximum. The asymmetry in the upper accretion curtain is probably due to the oblique rotator geometry of the system with an augmented accretion rate (perhaps assisted by twisted magnetic field lines) and/or reduced "blob" size at its leading edge. It is this inhomogeneity, with the proposed increase in "blob" size from a minimum at the leading edge of the accretion curtain, which facilitates the visibility of the upper emission region through a partially transparent curtain, for the majority of the first half of the spin cycle.

The general necessity for an inhomogeneous absorber component in models used for spectral fitting of X-ray data from IPs (Norton & Watson 1989) raises the question as to whether a similar variation in the covering fraction over the spin cycle is seen in all IPs. In the next two chapters data on two further IPs are analysed with the aim to make a preliminary assessment of the answer to this question.

Chapter 5

X-ray Analysis of V405 Aur

5.1 Preamble

The IP V405 Aur (RX J0558-53) was introduced in Section 2.3. It has been observed twice by *ASCA* (Table 3.2) and once by *RXTE* (Table 3.4). Details pertaining to the data reduction are given in sections 3.1.3 and 3.2.3 respectively; whereas, section 3.3 discusses the data analysis techniques.

The spin ephemeris of Allan et al. (1996) was used throughout the data analysis of V405 Aur (Section 2.3.1, Equation 2.2). Nevertheless the accuracy of this ephemeris is insufficient to retain consistency in phasing between the *ASCA* and *RXTE* observations.

5.2 The Light Curves

5.2.1 Period Analysis

Period analysis was carried out on both *ASCA* and the *RXTE* light curves data using the same methodology as that used for PQ Gem (Sections 3.3.1, 4.2.1). Equation 3.3 (Section 3.3.1) with p_0 set to 0.1, i.e. 90% confidence, was used to determine the signal-to-noise level below which the amplitude of a power peak was judged to be

satellite	instrument	Date	passband keV	frequency mHz	period s	S/N
ASCA	SIS1	05/10/96	0.5-10.0	$1.833750 \pm 2.631 \times 10^{-4}$	545.331±0.078	7.38
RXTE	PCA	26/04/96	2.0-22.0	$1.833990 \pm 5.334 \times 10^{-4}$	545.435±0.148	10.38
			2.0-22.0	$3.666469 \pm 7.121 \times 10^{-4}$	272.742±0.053	10.22

Table 5.1: The details of the statistically significant amplitude peaks found from period analysis of *ASCA* SIS1 data and *RXTE* PCA data. The signal-to-noise ratio was taken as the ratio of amplitude of the peak to the local mean of the prewhitened spectrum. The details of the analysis are given in Section 5.2.1.

insignificant. The noise level of the periodogram was taken to be the mean of the local amplitude spectrum after it had been prewhitened with the significant frequencies. The significant frequencies and their associated periods are presented in Table 5.1 with plots of the amplitude spectra, prewhitened spectra and window functions shown in Figure 5.1, for the *RXTE* (26/04/96) and *ASCA* (05/10/96) observations. The *RXTE* data show a significant amplitude peak at 1.83399mHz and 3.6665mHz; whereas the *ASCA* data show a significant peak only at 1.83375mHz. The frequencies of the amplitude peaks found from the *RXTE* data are entirely consistent with the period given for the spin ephemeris of Allan et al. (1996) (Section 2.3.1) and its first harmonic; but that calculated from the *ASCA* data gives a period which is shorter by comparison. The *ASCA* data from 21/03/99 showed no significant peaks to the 90% confidence level, though there was sufficient amplitude corresponding to a period of 545.15±0.26s to give a detection at the 68% confidence level.

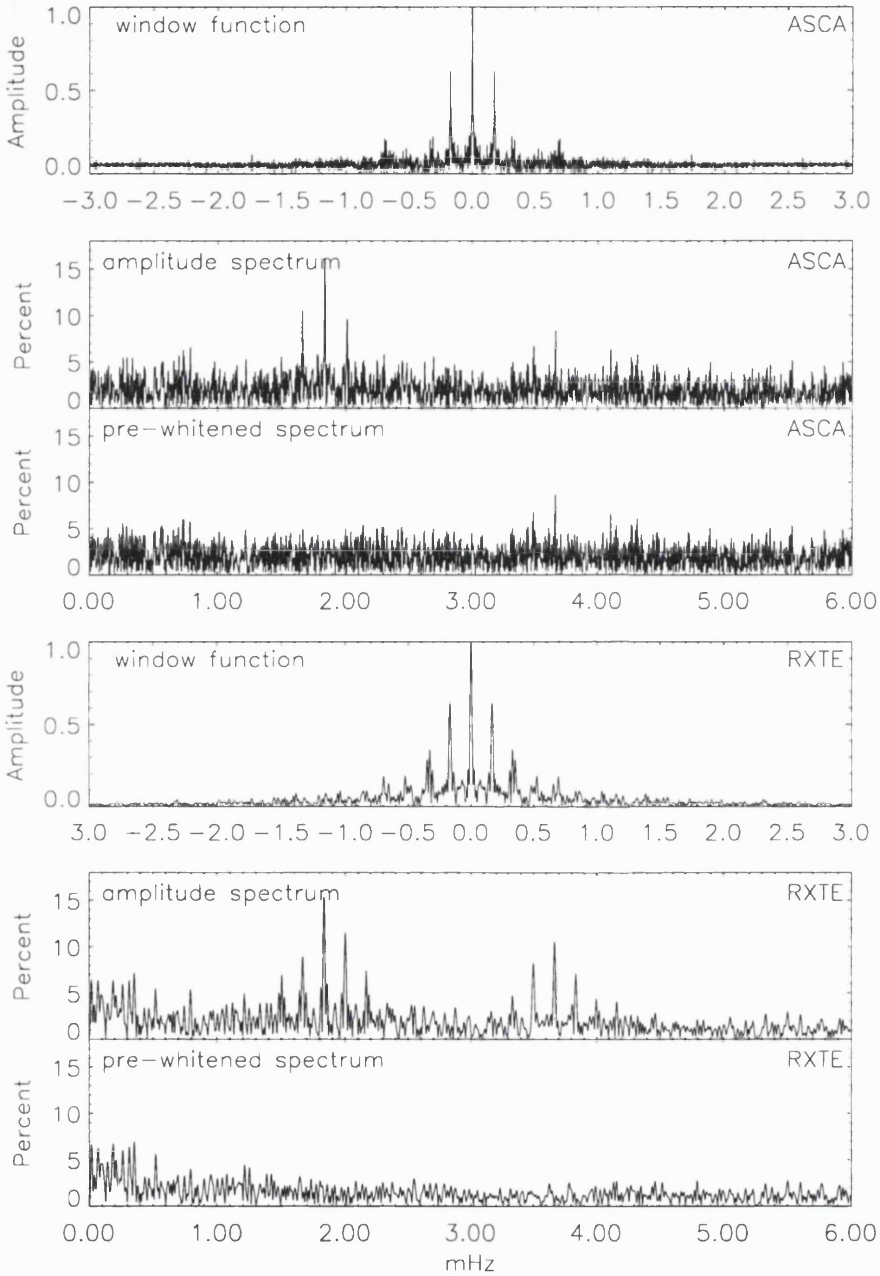

Figure 5.1: Periodograms of V405 Aur; the top 3 plots pertain to *ASCA* SIS1 data from observation 05/10/96 and the bottom 3 plots to the *RXTE* PCA data. In each group the top plot is the window function, the middle plot is the amplitude spectrum and the bottom plot is the amplitude spectrum prewhitened by the significant amplitude peaks given in Table 5.1.

5.2.2 Modulation

Light curves were extracted from both of the *ASCA* observations for the energy bands 0.7–1.0keV, 1.0–2.0keV, 2.0–4.0keV, 4.0–10.0keV and 0.5–10keV (in line with the analysis of the PQ Gem *ASCA* data, Section 4.2.2.1) and folded on the spin ephemeris (Section 2.3.1, Equation 2.2) as detailed in Section 3.1.3. The countrates and profiles from the two observations were very similar with only a meagre demonstration of the double pulse so prominent in the *ROSAT* soft X-ray light curve (Section 2.3.2), though its presence was slightly more visible in the observation from the 21/03/99. Hence, only the light curves from the longer observation (05/10/96) are presented on the left-hand side of Figure 5.2.

Likewise, light curves for the energy bands 2.0–25.0keV, 2.0–4.0keV, 4.0-10.0 keV and 8.0–25.0keV (in line with the analysis of the PQ Gem *RXTE* data, Section 4.2.2.2) were extracted from the *RXTE* data and folded on the spin ephemeris (Equation 2.2, Section 2.3.1) as detailed in Section 3.2.3. In these, with the possible exception of the 2.0-4.0 energy band, the double pulse is apparent, as is demonstrated on the right-hand side of Figure 5.2.

The hardness ratio, 8.0–25.0keV/2.0-8.0keV, calculated from the *RXTE* data with errors at the 1σ level, shows a minimal modulation with only marginal evidence for the double pulse over the spin cycle, Figure 5.3.

5.3 Spectroscopy

The energy range of the *ASCA* SIS data used in the spectral analysis was limited to >1.0keV due to the reduced low energy performance of the CCDs caused by radiation damage (Section 3.1.3). As already stated, this manifests itself as an apparent increase in absorption for data below 1keV (*ASCA* GOF 2000, Yaqoob et al., 2000) and hence it was considered preferable to exclude these data from the analysis. This restriction was not extended to the *ASCA* GIS.

The *ASCA* countrate of V405 Aur is low (~0.3 c/s) and hence, since the 21/03/99 observation was also of much shorter duration, spectral analysis of this

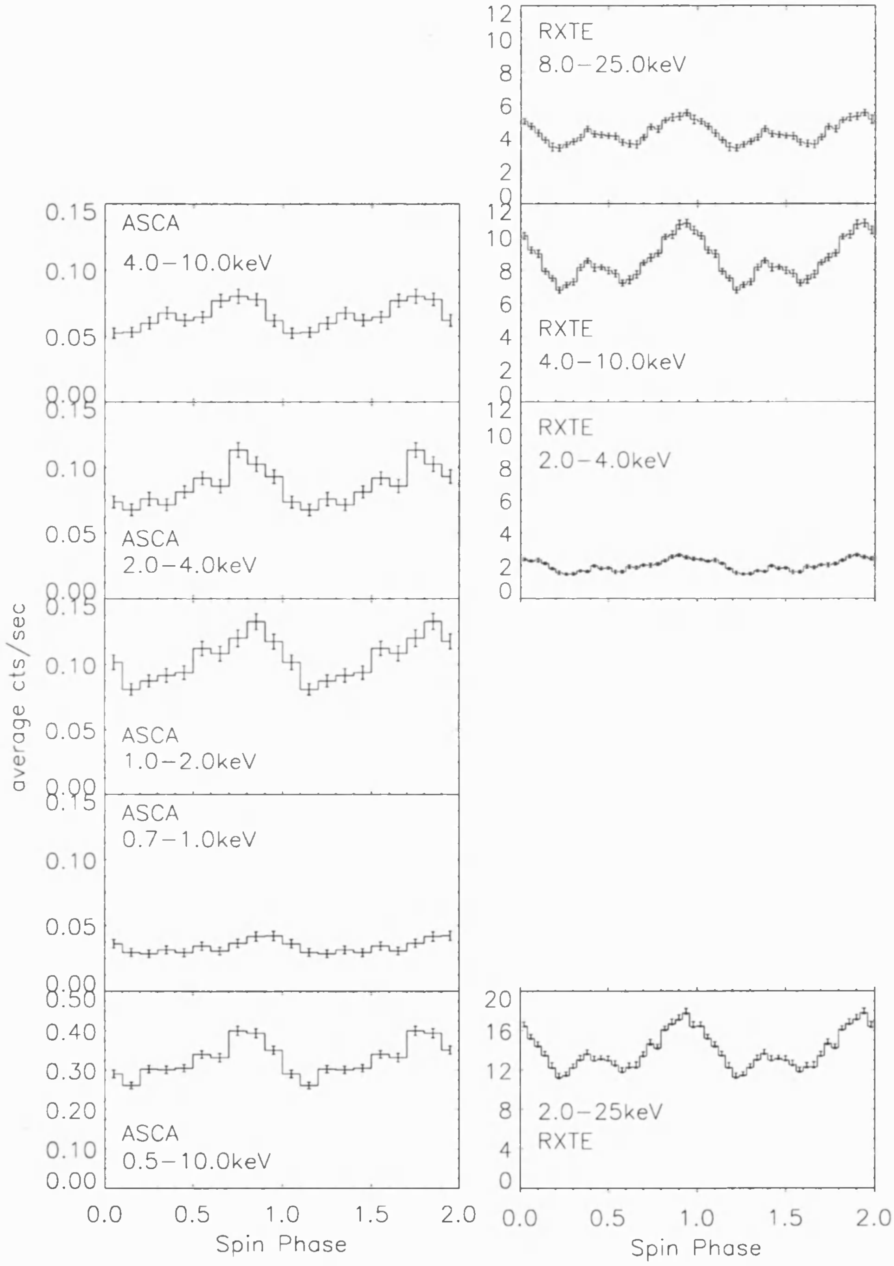

Figure 5.2: Light curves of V405 Aur folded on the spin ephemeris of Allan et al. (1996). Those from *ASCA* data (observation 05/10/96) are shown on the left-hand side; the plots from the bottom up are 0.5–10.0keV, 0.7–1.0keV, 1.0–2.0keV, 2.0–4.0keV, and 4.0-10.0 keV. Those from *RXTE* (26/04/96) data are shown on the right-hand side; the plots from the bottom up are 2.0–25.0keV, 2.0–4.0keV, 4.0-10.0 keV and 8.0–25.0keV. The phasing of the *ASCA* and *RXTE* light curves is not consistent (Section 5.1).

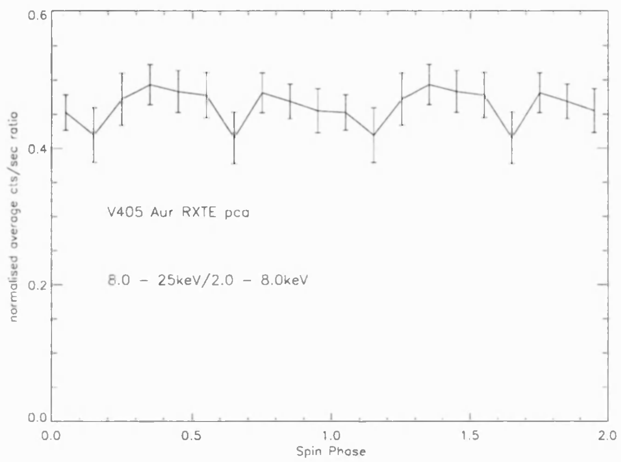

Figure 5.3: Plot of the hardness ratio 8.0–25.0keV/2.0-8.0keV calculated from the *RXTE* data of V405 Aur and marginally showing the double pulsed profile. The errors are calculated to the 1σ level.

observation was omitted.

5.3.1 The Integrated Spectra

5.3.1.1 ASCA

A model which consisted of an optically thin plasma emission (MEKAL code) and a cold photoelectric absorption (wabs) components was fitted simultaneously to *ASCA* data from both of the SIS and the GIS2 instruments using *xspec* (Section 3.3.2.2). The data from the GIS3 instrument were extremely noisy; hence these were excluded from the analysis. It was not possible to constrain the upper limit of the temperature parameter. The shock temperature depends on the mass and the radius of the white dwarf ($kT_s \approx 3\mu G M m_p/8R$); hence, it is assumed to be constant for the *ASCA* and *RXTE* observations. Therefore, the temperature parameter was fixed at 30keV in line with the value obtained from a separate spectral analysis using the *RXTE* data (Section 5.3.1.2).

The model gave a inadequate fit to the data (reduced chi-squared, χ^2_ν=1.57);

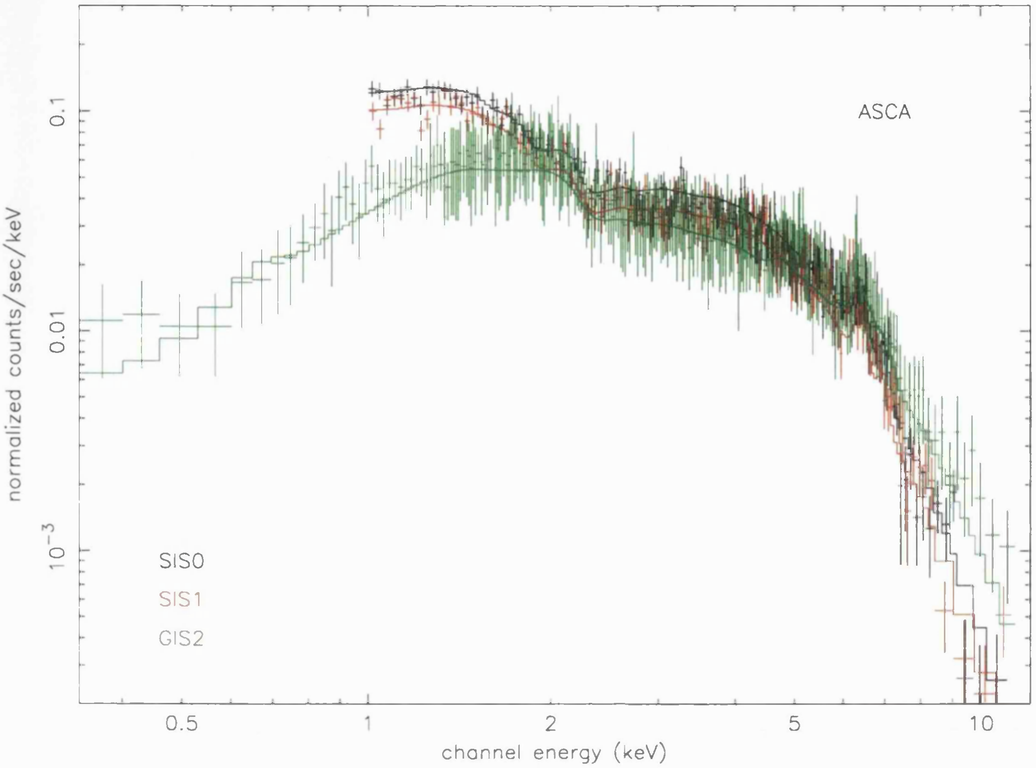

Figure 5.4: Plot of the integrated spectra of V405 Aur from the high bit rate data from the SIS0, SIS1 and GIS2 instruments aboard the *ASCA* satellite together with the fitted model (Table 5.2).

so the homogeneous photoelectric absorber was fixed at 0.06×10^{22} atoms cm^{-2} (in line with previous findings from analysis of the *ROSAT* data, Section 2.3.3) and an inhomogeneous (partial covering) absorption component (Section 3.3.2.2) was added (χ^2_ν=0.99). The fit to the GIS2 data was poor towards the lower energies ($\leq$ 1.0keV), therefore a blackbody component at kT=57eV (in line with analysis of the *ROSAT* data, Section 2.3.3) was included which gave a better visual fit to the data with a χ^2_ν=0.97. The fit was further improved (visually, χ^2_ν=0.87) by the addition of a Gaussian component at 6.4keV with a fixed width of 0.05keV (to model the fluorescent Fe emission line, Section 3.3.2.2); therefore this component was also retained. The best fit model, its unabsorbed flux between 2–10keV and χ^2_ν are given in Table 5.2 (*ASCA*, 1st entry) and plotted, together with the integrated spectra, in Figure 5.4.

5.3.1.2 RXTE

A spectral model which was composed of a photoelectric absorber (wabs) and optically thin plasma (MEKAL code) components (Section 3.3.2.2) gave a very poor fit to the data (χ^2_ν >5.0). It was necessary to fix the homogeneous photoelectric absorber at 0.06×10^{22} cm^{-2} (in line with previous findings from the analysis of *ROSAT* data, Section 2.3.3) and to introduce both an inhomogeneous (partial covering, Section 3.3.2.2) absorber, a Gaussian of fixed width (0.05keV) at 6.4keV (Section 3.3.2.2) and a second MEKAL component, in order to achieve an acceptable fit with a χ^2_ν ~1. Removal of the Gaussian increased the χ^2_ν to 1.28, therefore this component was retained. The results are presented in Table 5.2.

5.3.2 Phase-Resolved Spectroscopy

As already stated, the *ASCA* countrate of V405 Aur is low (~ 0.3 c/s) and, hence, the photon statistics of the 05/10/96 data were insufficient to enable the data to be split into more than 5 phase bins of equal duration, rather than 10, as in the case of PQ Gem.

The data from the SIS and GIS2 instruments were extracted into 5 phase bins of equal duration and defined on the spin period as described in Section 3.1.3. The reference model was the best fit model from the analysis of the integrated spectrum refitted without the blackbody component (second *ASCA* entry in Table 5.2). This component was removed, because the lack of sensitivity to the soft X-ray spectrum in the *ASCA* instrumentation and the small difference its presence made to the overall fit did not justify the additional complexity it gave to the model.

The reference model was fitted simultaneously to the 5 phase-resolved spectra. Three series of analyses were conducted during which all the parameters of the reference model remained fixed except for those of the normalisation and/or in-

Satellite	N_H (fraction) 10^{22} cm^{-2}	BB norm: 10^{-3}	MEKAL1 kT keV	MEKAL1 norm: 10^{-2}	MEKAL2 kT keV	MEKAL2 norm: 10^{-1}	Gaussian norm: 10^{-5}	unabs: flux 10^{-11}erg cm^{-2} s^{-1}	χ^2_ν (dof)
ASCA	$5.0^{6.1}_{4.1}$ $(0.47^{0.49}_{0.45})$	$9.97^{14.6}_{5.35}$	30 (fixed)	$1.33^{1.38}_{1.28}$	n/a	n/a	$6.6^{8.0}_{5.4}$	2.04	0.87 (655)
	$5.4^{6.4}_{4.4}$ $(0.47^{0.49}_{0.45})$	n/a	30 (fixed)	$1.34^{1.40}_{1.29}$	n/a	n/a	$6.9^{7.9}_{5.3}$	2.06	0.89 (656)
RXTE	15^{18}_{13} $(0.88^{0.94}_{0.83})$	n/a	$29.9^{39.6}_{23.7}$	$2.28^{2.51}_{2.12}$	$1.14^{1.39}_{0.88}$	$1.2^{2.1}_{0.42}$	$5.9^{8.0}_{3.1}$	6.19	1.08 (43)

Table 5.2: Results from spectral analysis of the integrated spectrum including the errors at 90% confidence range. The best fit models are given as 1st entry for the *ASCA* and *RXTE*; the 2nd *ASCA* entry is the reference model used in the phase resolved spectroscopy. The models were fitted simultaneously to the high bitrate data from all 4 instruments on the *ASCA* satellite and to the PCA instrument on the *RXTE* satellite. N_H applies to the partial covering absorber. The metallicity was fixed at solar abundance for the *RXTE* data, but was fitted to give a value of $0.9^{1.3}_{0.6}$ solar abundance for the *ASCA* data. The "unab: flux" column holds the flux calculated on the unabsorbed models for the 2–10keV energy band.

phase	N_H 10^{22} cm^{-2}	fraction	MEKAL norm: 10^{-2}	Gaussian norm: 10^{-5}	flux 2–10keV 10^{-11}erg cm^{-2}s^{-1}	χ^2_ν (dof)
0.0-0.2	$10^{15}_{6.9}$	$0.47^{0.53}_{0.42}$	$1.30^{1.47}_{1.17}$	$9.1^{12}_{6.4}$	1.64	1.04 (194)
0.2-0.4	$5.2^{7.7}_{3.6}$	$0.54^{0.57}_{0.50}$	$1.34^{1.48}_{1.24}$	$9.6^{17}_{6.0}$	1.79	1.11 (204)
0.4-0.6	$3.4^{5.1}_{2.2}$	$0.45^{0.48}_{0.41}$	$1.23^{1.32}_{1.15}$	$7.0^{9.5}_{4.2}$	1.73	1.20 (202)
0.6-0.8	$5.0^{6.8}_{3.8}$	$0.52^{0.55}_{0.49}$	$1.59^{1.71}_{1.50}$	$7.4^{11}_{5.0}$	2.11	1.32 (235)
0.8-1.0	$4.9^{7.5}_{3.3}$	$0.43^{0.47}_{0.38}$	$1.30^{1.41}_{1.21}$	$10^{12}_{6.3}$	1.81	1.25 (214)

Table 5.3: Results from spin phase-resolved spectral analysis of V405 Aur during which the reference model (Table 5.2) was simultaneously fitted to the high bitrate data from the two SIS and the GIS2 instruments on the *ASCA* satellite. Only the normalisation and inhomogeneous absorption parameters of the reference model were allowed to vary during the spectral fitting. Errors at the 90% confidence range are given for these parameters, with the χ^2_ν and flux (uncorrected for absorption) for the 5 phases also included.

homogeneous (partial covering, Section 3.3.2.2) absorption. The results from these analyses are presented in Tables 5.3–5.5 respectively with those of Table 5.3 plotted in Figure 5.4. The χ^2_ν in Tables 5.3–5.5 show that any of the three scenarios fit the data equally well.

Although analysis on the *RXTE* integrated spectrum was carried out, so as to ascertain the temperature of the hard X-ray emission and the unabsorbed flux, this was not extended to phase-resolved spectroscopy. This was in line with the approach taken to the analysis of the PQ Gem data, because the energy resolution of the *RXTE* PCA data (18% @ 6.0keV) is much poorer than that of the *ASCA* SIS (2%).

phase	N_H 10^{22} cm^{-2}	fraction	flux 2–10keV 10^{-11}erg cm^{-2} s^{-1}	χ^2_ν (dof)
0.0-0.2	$11^{14}_{9.1}$	$0.49^{0.51}_{0.47}$	1.64	1.04 (196)
0.2-0.4	$5.1^{6.2}_{4.2}$	$0.53^{0.56}_{0.51}$	1.76	1.11 (206)
0.4-0.6	$5.3^{6.8}_{4.1}$	$0.47^{0.50}_{0.45}$	1.79	1.21 (204)
0.6-0.8	$2.8^{3.5}_{2.3}$	$0.45^{0.48}_{0.42}$	1.89	1.43 (237)
0.8-1.0	$5.5^{7.0}_{4.4}$	$0.44^{0.47}_{0.42}$	1.80	1.25 (216)

Table 5.4: Results from spin phase-resolved spectral analysis of V405 Aur during which the reference model (Table 5.2) was simultaneously fitted to the high bitrate data from the two SIS and the GIS2 instruments on the *ASCA* satellite. Only the partial covering absorber parameters of the reference model were allowed to vary during the spectral fitting. Errors at the 90% confidence range are given for these parameters, with the χ^2_ν and the flux (uncorrected for absorption) for the 5 phases also included.

phase	MEKAL norm: 10^{-2}	Gaussian norm: 10^{-5}	flux 2–10keV 10^{-11}erg cm^{-2} s^{-1}	χ^2_ν (dof)
0.0-0.21	$1.20^{1.23}_{1.17}$	$10^{12}_{6.7}$	1.64	1.09 (196)
0.2-0.4	$1.25^{1.28}_{1.21}$	$11^{13}_{7.0}$	1.71	1.15 (206)
0.4-0.6	$1.32^{1.36}_{1.29}$	$5.9^{8.7}_{3.5}$	1.77	1.20 (204)
0.4-0.8	$1.53^{1.56}_{1.49}$	$9.4^{11}_{5.6}$	2.06	1.34 (237)
0.8-1.0	$1.37^{1.40}_{1.33}$	$9.4^{11}_{5.8}$	1.86	1.25 (216)

Table 5.5: Results from spin phase-resolved spectral analysis of V405 Aur during which the reference model (Table 5.2) was simultaneously fitted to the high bitrate data from the two SIS and the GIS2 instruments on the *ASCA* satellite. Only the normalisation parameters of the reference model were allowed to vary during the spectral fitting. Errors at the 90% confidence range are given for these parameters, with the χ^2_ν and flux (uncorrected for absorption) for the 5 phases also included.

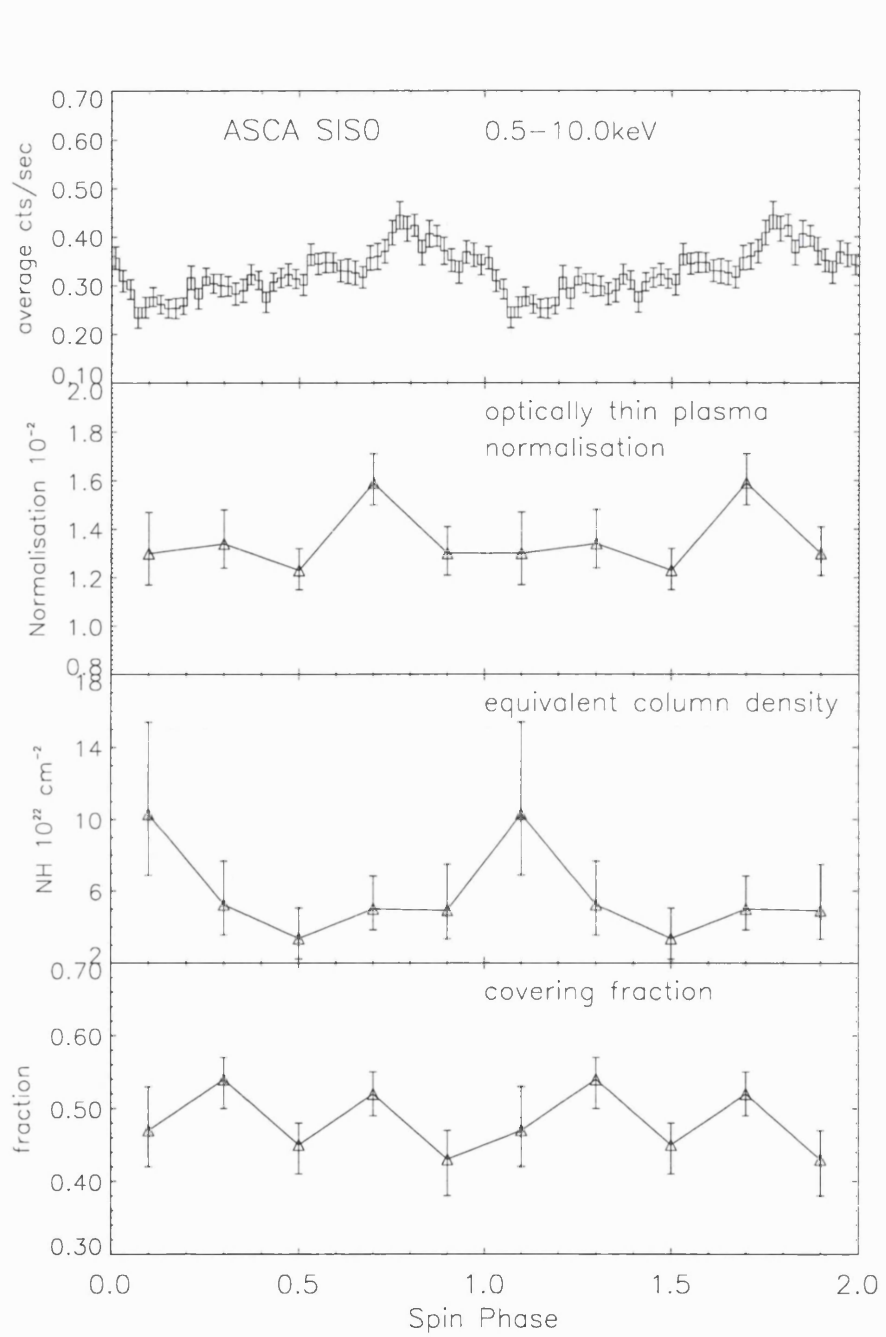

Figure 5.5: Plots of results from spin phase-resolved spectroscopy of V405 Aur (Table 5.3) in which all parameters of the reference model (middle entry, Table 5.2), except those for the normalisations and partial covering absorption, were fixed during the spectral fitting. The plots from the top are the *ASCA* 0.5–10.0keV light curve (included for clarity), the normalisation of the optically thin plasma emission code, the equivalent neutral hydrogen column density (absorption) and the covering fraction (absorption). The phasing of the light curve and the spectroscopy results are consistent.

5.4 Discussion

5.4.1 Interpretation of the Results

The light curves of V405 Aur indicate that the X-ray emission is very much more variable across observations than previously thought (Section 2.3.2) and in comparison to those of PQ Gem (Section 4.1.2.1). For instance, neither the *ROSAT* 0.7–2.0keV light curve (Figure 2.4) nor the light curves from *ASCA* observation of the 05/10/96 (Figure 5.2, left-hand side) show the double pulse which is so clearly demonstrated in the *ROSAT* 0.1–0.5keV light curve (Figure 2.4); whereas, the light curves from *RXTE* (Figure 5.2, right-hand side) show a well defined though asymmetrical double pulse. The presence of this feature in the 8.0-25keV *RXTE* light curve is indicative that, in the hard X-rays, at least, it originates from the changing visibility of the emission regions rather than a superimposed absorption effect.

It is very difficult to explain the changing visibility of the double pulse. There are two IPs, GK Per and XY Ari, which only exhibit the double pulsed emission in quiescence. Hellier et al. (1997) suggest that in the latter during outburst, the increased accretion rate causes the truncated accretion disc to more closely approach the surface of the white dwarf and thus to obscure the second emission region from sight. This phenomenon can be consistent with either the weak magnetic field/fast rotator or the hybrid occultation/absorption models (Section 1.3.4). However, an increase in the accretion rate is unacceptable as an explanation for the absence of the double pulse in the *ASCA* data (05/10/96) since the unabsorbed flux (2.0–10.0keV) (Table 5.2) from the spectral fitting of the *ASCA* data is less than that for the *RXTE* spectral model.

I suggest an alternative proposition to that of Hellier et al. (1997): at times of lower flux, when the inner edge of the disc is farther from the surface of the white dwarf, the boundary region (Figure 1.5) is threaded by a particular set of magnetic field lines, the footprint of which, in the hemisphere pointing away from the observer, is obscured from the line of sight. At times of increased flux, when the inner edge of the disc moves closer to the surface, the disc is threaded by a different set of magnetic field which allows for their footprint (lower hemisphere) to become visible along the line of sight.

It is also possible to explain the presence of the double pulse in the soft *ROSAT* (0.1–0.5keV), at a time when it is absent from the hard *ROSAT* (0.7–2.5keV) (Figure 2.4), in terms of this alternative proposition. The inhomogeneous accretion model (Section 1.2.2.1) allows for those emission regions which produce the soft X-rays to surround the hard X-ray emission areas (Figure 1.2). In this case, the footprint of magnetic field lines associated with the production of hard X-rays could be occulted, even though a portion, at least, of the surrounding soft X-ray emission regions are visible. Haberl et al. (1994) did suggest that a possible cause for their estimate of a small blackbody emission area could be due to its restricted visibility (Section 2.3.3).

Additionally, the results from the phase-resolved spectroscopy, Table 5.3 & Figure 5.5, are consistent with the aforementioned alternative suggestion since the normalisation of the optically thin plasma does show a solitary peak at phase 0.6–0.8 (Figure 5.5). The phasing of the absorption (equivalent HI column density) maximum at 0.0–0.2 (Figure 5.5), is also compatible with this interpretation, since it can be attributed to the interception of the inner edge of the accretion disc along the line of sight. By means of similar analysis to that of Section 4.5.4, the radius of the inner edge of the accretion is $\sim 14R_{WD}$ which implies that the minimum angle of inclination to allow the disc to intercept along the line of sight is $\sim 86°$. This is much greater than the low to moderate inclination suggested by Allan et al. (1996) (Section 2.3.4) for this system. But, the calculation of the accretion luminosity was limited to consideration of 2–10keV unabsorbed flux and hence the estimate of the $\dot{M}$ is very approximate. Therefore, interception of the inner edge of the disc along the line of sight at some spin phases can not be ruled out.

The presence of a marginal double maxima in the covering fraction of the absorption (phase-resolved spectroscopy results, Figure 5.5) is consistent with the weak magnetic field/fast rotator model (Section 1.3.4), though ideally one would expect these to be offset by 0.25 phase with respect to the two emission regions. Nevertheless, the co-incidence of one of these maxima with that of the normalisation of the optically thin plasma could be due to the width of the phase bins used.

5.4.2 Comparison to PQ Gem

V405 Aur and PQ Gem share the property of a well-defined soft X-ray component (Sections 2.2.3 & 2.3.3) which was borne out by the requirement for a blackbody component in the spectral analysis of the *ASCA* data in both IPs. Period analysis shows the dominant amplitude to be at the spin frequency in both systems. The absence of a peak at the beat frequency is indicative of disc accretion without disc overflow (Wynn & King 1992), as in the case of PQ Gem, though, this may be a variable feature of V405 Aur (Section 2.3.4).

Similarly, they both exhibit double peaked light curves, but the double peak in V405 Aur was absent from the *ASCA* data and the *ROSAT* 0.7–2.4keV data. In the case of PQ Gem, the double maxima owe their origin to a combination of varying absorption effects and changing visibility of the hard X-ray emission over the spin cycle which leads to the suggestion of an adaptation of the accretion curtain model (Section 4.4.3). On the other hand, in V405 Aur there is a lack of strong cyclic absorption variation and the analysis of the *ASCA* data is consistent with the weak magnetic field/fast rotator model combined with absorption by the accretion disc when viewing the lower emission region. However, overall the results from the analysis for this thesis (especially when interpreted in conjunction with the previous findings of Allan et al. (1996)) indicate that the accretion pattern may well be transient due, perhaps, to variability in the accretion rate which causes the accretion disc to be threaded by different magnetic fields lines.

The variation in the covering fraction of the partial covering absorber in PQ Gem strongly resembles the modulation in its hardness ratio. However, there is only a very minimal modulation shown in the hardness ratio of V405 Aur; even so, this is consistent with the marginal variation displayed in the covering fraction of the absorber. This may well signify that inhomogeneous accretion is a feature of both systems and that a varying covering fraction of the absorber is a reasonable model of this property.

Chapter 6

X-ray Analysis of RX J1712.6-2414

6.1 Preamble

The relevant historical aspects of the IP RX J1712.6-2414 were introduced in Section 2.4. It was observed in 1996 by both *ASCA* (Table 3.2) and *RXTE* (Table 3.4). Details of the data reduction are provided in Sections 3.1.3 and 3.2.4; whereas Section 3.3 covers the data analysis techniques.

6.2 The Light Curves

6.2.1 Period Analysis

The variability in the *ASCA* and *RXTE* light curves of RX J1712.6-2414 was analysed by the same method as for PQ Gem and V405 Aur (Sections 3.3.1, 4.1.1, 5.2.1). Equation 3.3 (Section 3.3.1) with p_0 set to 0.1, (i.e. a 90% confidence level that the signal is genuine) was used as the criterion to judge the significance of the amplitude of the peak. The noise level of the periodogram was taken to be the mean of the amplitude spectrum after it had been prewhitened with the significant frequencies. The considerable "red noise" present at lower frequencies (amplitude and prewhitened spectra, Figure 6.1) tended to mask power peaks at the orbital (Ω), beat (ω-Ω) and spin (ω) frequencies so that significant power peaks were not determined. Detrending of the data was applied to the individual datasets in order to reduce this effect, but this had the effect of also removing power at the required frequencies. Figure 6.1 shows the window function, power spectra and the power spectra prewhitened with the frequencies which correspond to the beat (1003.299±0.003s, Section 2.4.1), spin (927.66±0.41s, Section 2.4.1), and the orbital (3.42h±0.02h, Section 2.4.1) periods. Only the removal of the 1003s period from the *RXTE* power spectra made a notable difference in the associated prewhitened spectra. Buckley et al. (1995) attributed the presence of similar "red noise" in their CCD photometry to the ubiquitous CV property of aperiodic flickering.

6.2.2 Modulation

The *ASCA* and *RXTE* light curves were folded on the 927.66±0.41s spin period and the 1003.299±0.003s beat period (Section 2.4.1) as described in Sections 3.1.3 & 3.2.3 respectively. The *ASCA* folded light curves for energy bands 0.7–1.0keV, 1.0–2.0keV, 2.0–4.0kev, 4.0–10keV, and 0.5–10keV are shown in Figure 6.2 and the *RXTE* folded light curves for energy bands 2.0–4.0keV, 4.0–10.0keV, 8.0–25.0keV and 2.0–25.0keV are shown in Figure 6.3. Both the *ASCA* (0.5–10.0keV) and *RXTE* (2.0–25.0keV) light curves show modulations of $\sim$ 18% and $\sim$19% respectively when folded over the beat pulse; whereas they show only marginal variation over the spin period.

Hardness ratios calculated from the beat folded *RXTE* light curves for energy bands 8.0–25.0keV/2.0–8.0keV and *ASCA* light curves for energy bands 4.0–10.0keV/1.0–4.0keV (Figures 6.4 and 6.5, respectively) showed no modulation except for a marginal increment at phase 0.5-0.6 in the case of the latter. This effect was unassociated with any obvious feature in the light curves or the results from the phase-resolved spectroscopy (Figure 6.7) at this timing.

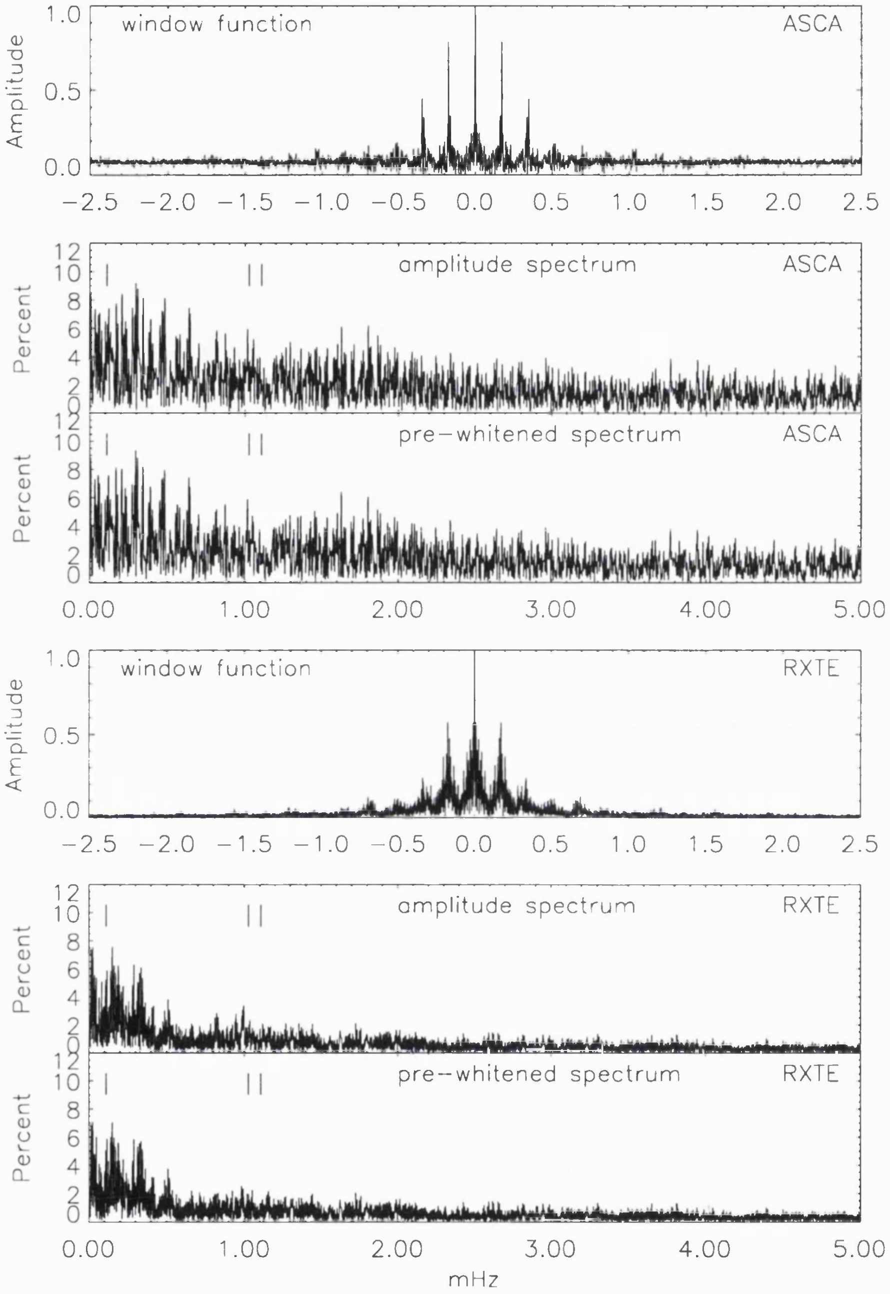

Figure 6.1: Periodograms of RX J1712.6-2414 calculated from *ASCA* SIS0 data (top 3 plots) and *RXTE* PCA data (bottom 3 plots). In each group, the window function is shown in the top plot and the amplitude function in the middle plot. This latter, prewhitened with the orbital, beat and spin frequencies (Section 6.2.1) is displayed in the bottom plot of each group. The position of these frequencies respectively (from left to right) are indicated by the vertical bars.

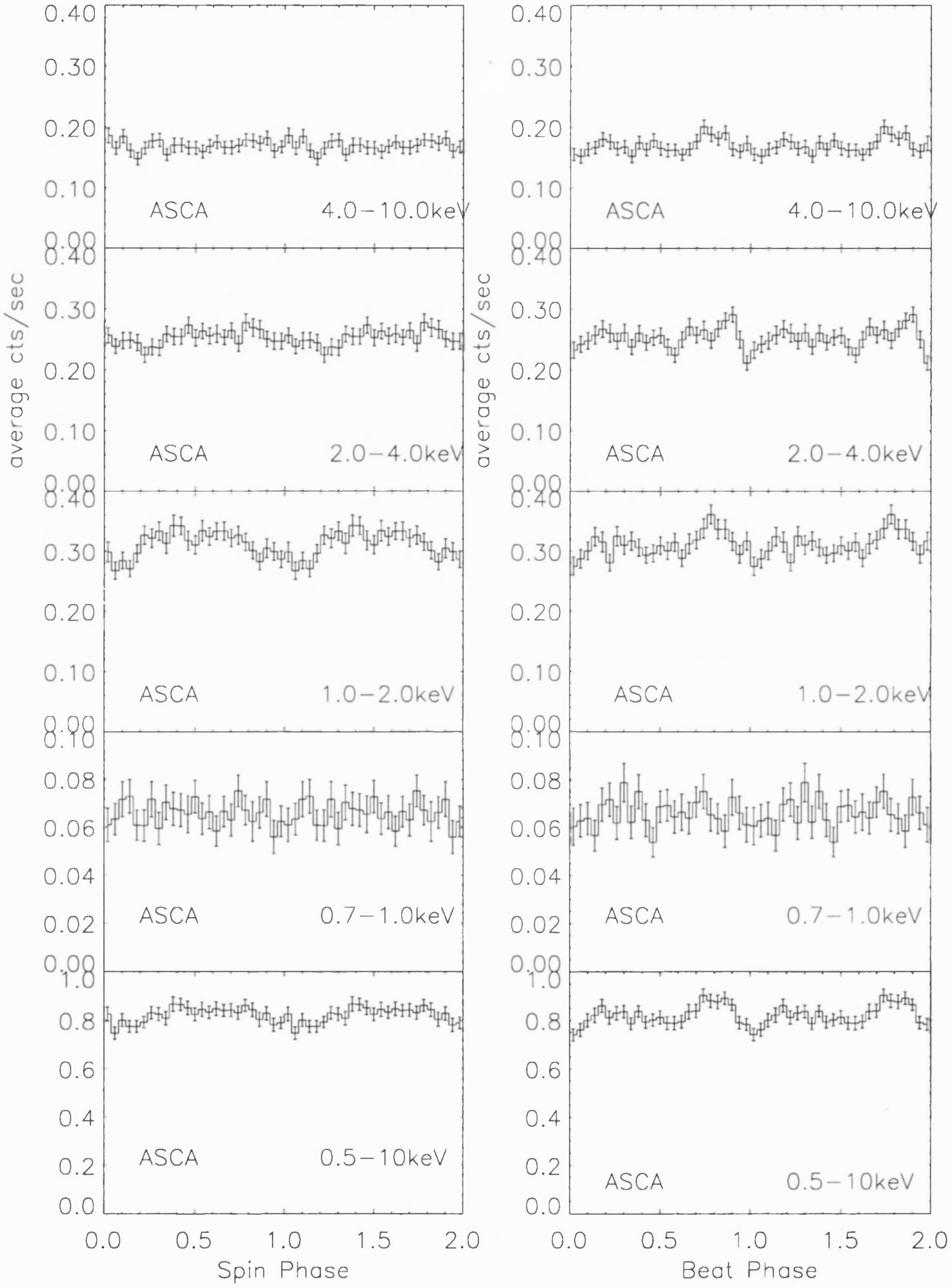

Figure 6.2: Light curves of RX J1712.6-2414 taken from *ASCA* SIS0 data folded on the 927.66s spin period (left-hand column) and on the 1003.299s, beat period (right-hand column). The energy bands from the top down are 4.0–10.0keV, 2.0–4.0keV, 1.0–2.0keV, 0.7–1.0keV and 0.5–10keV.

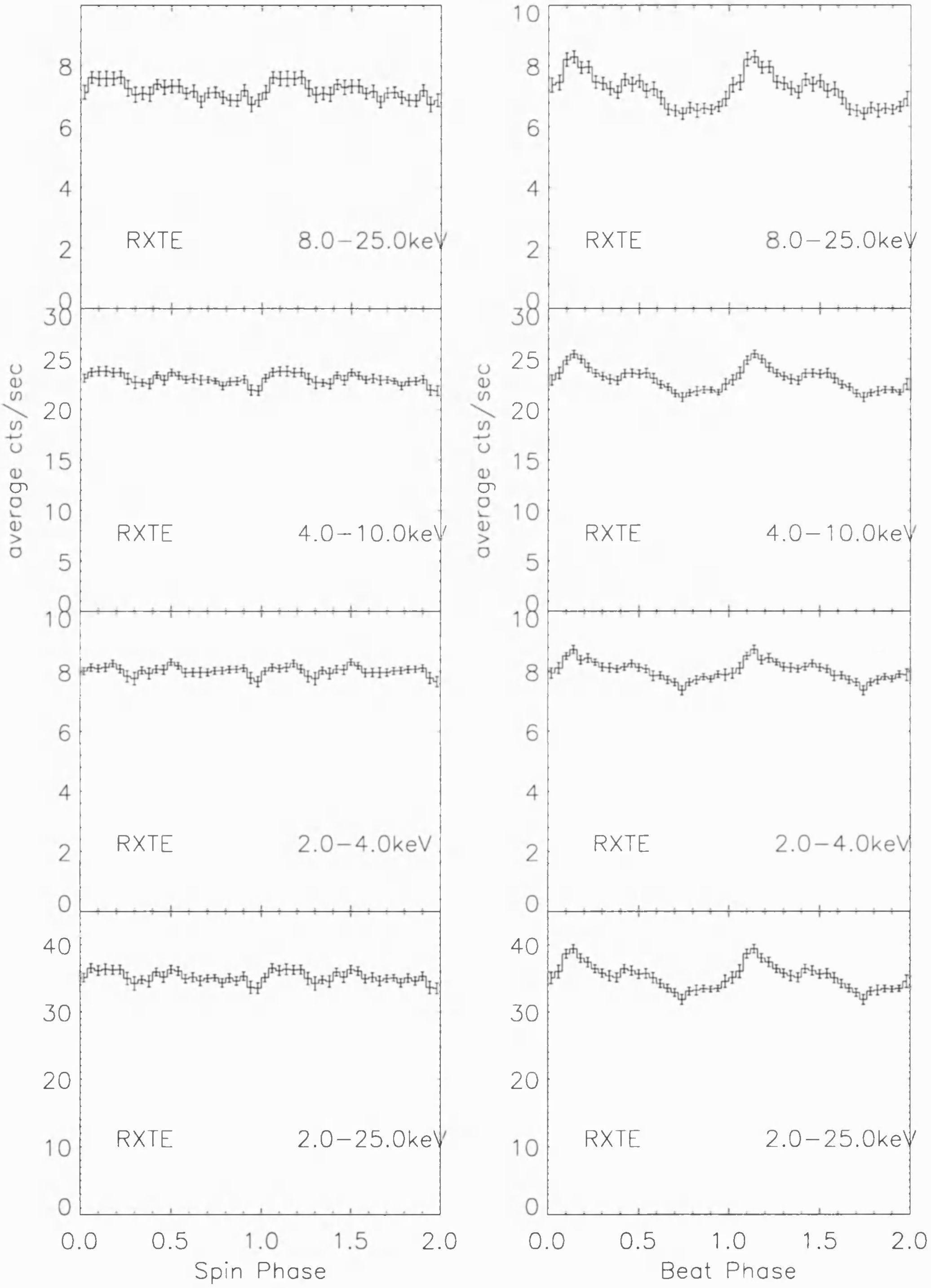

Figure 6.3: Light curves of RX J1712.6-2414 taken from *RXTE* PCA data folded on the 927.66s spin period (left-hand column) and on the 1003.299s, beat period (right-hand column). The energy bands from the top down are 8.0–25.0keV, 4.0–10.0keV, 2.0–4.0keV and 2.0–25.0keV.

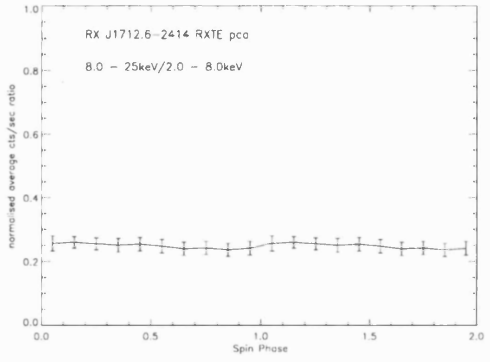

Figure 6.4: 8.0–25.0keV/2.0–8.0keV *RXTE* hardness ratio of RX J1712.6-2414.

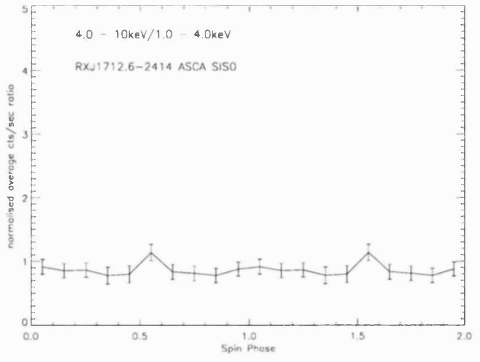

Figure 6.5: 4.0–10.0keV/1.0–4.0keV *ASCA* hardness ratio of RX J1712.6-2414.

6.3 Spectral Analysis

At the end of Chapter 4 the question was posed as to whether the IPs V405 Aur and RX J1712.6-2414 demonstrate a similar correspondence between the modulation of the absorption covering fraction and the 8.0-25.0keV/0.2-8.0keV *RXTE* hardness ratio as that demonstrated for PQ Gem. Therefore, the scope of the spectral analysis was matched to that undertaken for PQ Gem; i.e. it was limited to the *ASCA* data. Details of the *xspec* models used in this analysis are discussed in Section 3.3.2.2.

The *ASCA* data used in the spectral analysis of RX J1712.6-2414 were limited to energies > 1.0keV due to the recognised deterioration of the CCDs at lower energies (Sections 3.1.3, 5.3).

6.3.1 The Integrated Spectrum

The integrated spectrum was analysed using a model which comprised of a MEKAL code component for the emission spectrum and photo-electric absorption for the attenuation, which was split between homogeneous (wabs) and partial covering components. This model was simultaneously fitted to the high bit-rate data from all four instruments to give a $\chi^2_\nu = 1.13$. This was improved to $\chi^2_\nu = 1.04$ by the addition of

N_{H_1} 10^{22} cm^{-2}	N_{H_2} (covering) 10^{22} cm^{-2} (%)	MEKAL *kT* keV	MEKAL norm: 10^{-2}	Gaussian norm: 10^{-4}	flux(obs) 2-10keV 10^{-11}erg cm^{-2} s^{-1}	χ^2_ν (dof)
$0.24^{0.26}_{0.21}$	$9.8^{13}_{6.6}$ (28^{31}_{24})	22^{30}_{18}	$3.3^{3.5}_{3.2}$	$1.2^{1.4}_{1.0}$	4.5	1.04 (1235)

Table 6.1: Results from spectral analysis of the integrated spectrum including the error range at 90% confidence level. The model was fitted simultaneously to the high bit-rate data from all 4 instruments on the *ASCA* satellite. N_{H_1} corresponds to the homogeneous photoelectric absorber; whereas N_{H_2} applies to the partial covering absorber. The normalisations are as the standard for the MEKAL and Gaussian *xspec* models used (Section 3.3.2.2) and the metallicity was fixed at solar abundance.

a Gaussian component of fixed width of 0.05keV at 6.4keV (Section 1.3.3), to model the fluorescent iron line. The results from fitting the integrated spectrum are given in Table 6.1; the models and integrated spectra are plotted in Figure 6.6.

6.3.2 Phase-resolved Spectroscopy

The photon statistics of the *ASCA* data of RX J1712.6-2414 were sufficient to subdivide the data into ten equal time bins on either the spin (927s) or the beat (1003s) period. The light curves from the *ASCA* data of RX J1712.6-2414 show very little modulation on the spin period, in comparison to that present on the beat period (Section 6.2.2); therefore, beat phase-resolved spectral analysis was performed on the *ASCA* data. This is contrary to the similar analysis carried out on the *ASCA* data from PQ Gem which was based on the spin period.

Ten phase-resolved spectra were extracted from the *ASCA* data using the 1003.299s beat period (Section 2.4.1) and the same arbitrary epoch as for folding the light curves (Sections 3.1.3 and 3.2.3). Hence the phasing of the results is consistent with that of the beat folded light curves (Figure 6.2). Three series of analyses were

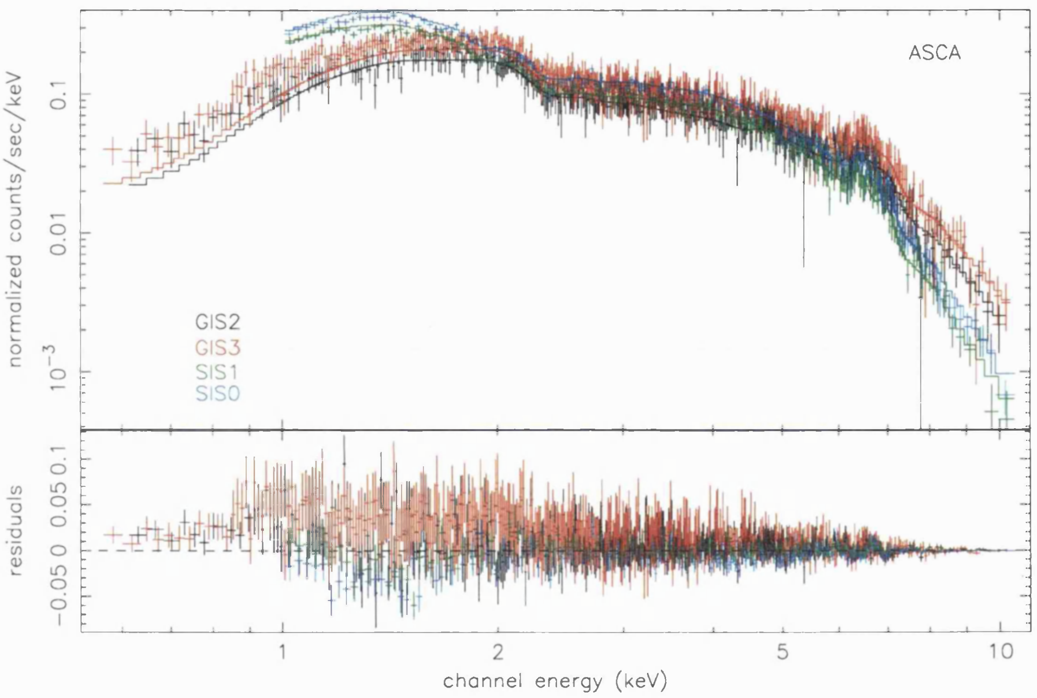

Figure 6.6: Integrated spectra of RX J1712.6-24 data from the SIS and GIS instruments on the *ASCA* satellite, together with the model (documented in Table 6.1) and residuals derived from fitting to all 4 spectra simultaneously.

performed on these spectra during which the absorption and/or the normalisation parameters were allowed to vary from the reference model. The reference model was taken as the best fit from the spectral analysis of the integrated spectrum (Section 6.3.1 and Table 6.1). The homogeneous absorption component in this model was assumed to originate from the ISM; hence it was fixed throughout the subsequent analysis. The results are documented in Tables 6.2–6.4 and those pertaining to Table 6.2 are plotted in Figure 6.7. It can be seen from the respective χ^2_ν in the results, Tables 6.2–6.4, that the modulation in the light curve can be equally well accounted for by differences in the emission, the attenuation or a combination of both over the beat period. Nonetheless, in the last case, only the normalisation parameter shows a marginal variation beyond the error bounds, since the absorption parameters for this model completely lack such a variation. In other words, in this case the modulation can be accounted for solely by changes in the fraction of the emitting area visible over the beat cycle.

6.4 Discussion

Supported by the simulations of Garlick (1996), Buckley et al. (1997) suggest that the light curve modulation in RX J1712.6-2414 is due to a 30%-40% difference in the accretion rate between the two poles, one of which is always hidden due to the low inclination. As already stated in Section 4.4.3, an increase in the accretion rate implies a corresponding decrease in the height of the accretion column accompanied by an increase in the length of the column of cool gas above the shock. In the case of RX J1712.6-2414, the observer's line of sight must be approximately parallel to the magnetic field lines at all times due to the low inclination of the system and the small dipole offset angle thought to pertain to this system (Section 2.4.1). Hence, evidence of an increase in the column density and/or the covering fraction might accompany the augmented accretion rate. However, in the results from the phase-resolved spectroscopy, it is demonstrated that the only modulation is a marginal variation in the emission normalisation (Table 6.2 and Figure 6.7). This, together

phase	N_{H_2} 10^{22} cm^{-2}	fraction	MEKAL norm: 10^{-2}	Gaussian norm: 10^{-5}	flux 2–10keV 10^{-11}erg cm^{-2}s^{-1}	χ^2_ν (dof)
0.0-0.1	$4.7^{12}_{2.3}$	$0.25^{0.32}_{0.19}$	$2.64^{2.98}_{2.46}$	$18.2^{23.5}_{9.50}$	3.84	1.16 (173)
0.1-0.2	$12^{23}_{4.5}$	$0.29^{0.39}_{0.20}$	$3.27^{3.84}_{2.89}$	$20.2^{25.6}_{9.68}$	4.41	0.90 (190)
0.2-0.3	$30^{68}_{9.1}$	$0.40^{0.63}_{0.23}$	$3.96^{6.63}_{3.07}$	$6.20^{14.3}_{0.00}$	4.42	0.98 (190)
0.3-0.4	$10^{22}_{4.7}$	$0.32^{0.42}_{0.24}$	$3.24^{3.89}_{2.89}$	$18.7^{22.3}_{9.92}$	4.34	1.01 (194)
0.4-0.5	$8.1^{30}_{3.5}$	$0.32^{0.50}_{0.25}$	$3.06^{4.30}_{2.76}$	$11.8^{17.8}_{4.84}$	4.13	0.95 (201)
0.5-0.6	$16^{42}_{4.0}$	$0.32^{0.51}_{0.20}$	$3.27^{4.50}_{2.73}$	$10.2^{16.7}_{3.25}$	4.14	0.98 (198)
0.6-0.7	$5.0^{12}_{1.8}$	$0.27^{0.34}_{0.21}$	$3.03^{3.42}_{2.78}$	$10.0^{15.2}_{2.39}$	4.25	1.14 (199)
0.7-0.8	$14^{25}_{7.2}$	$0.33^{0.42}_{0.24}$	$3.67^{4.25}_{3.25}$	$13.7^{22.9}_{8.07}$	4.71	0.86 (206)
0.8-0.9	$11^{18}_{6.4}$	$0.35^{0.41}_{0.28}$	$3.85^{4.35}_{3.49}$	$10.2^{16.2}_{1.68}$	4.94	0.93 (211)
0.9-1.0	$4.4^{9.9}_{1.7}$	$0.29^{0.35}_{0.23}$	$3.01^{3.39}_{2.78}$	$7.59^{13.1}_{0.00}$	4.22	0.91 (180)

Table 6.2: Results from 10-bin beat phase-resolved spectral analysis of RX J1712.6-2414 during which the high bit-rate data from both SIS instruments on the *ASCA* satellite were simultaneously fitted to the reference model (Table 6.1). During the fitting the normalisation and partial covering absorption parameters of the reference model were allowed to vary. The error ranges at the 90% confidence level are given for these parameters, with the χ^2_ν and observed flux (uncorrected for absorption) for the 10 phases also included.

phase	N_{H_2} 10^{22} cm^{-2}	fraction	flux 2–10keV 10^{-11}erg cm^{-2} s^{-1}	χ^2_ν (dof)
0.0-0.1	20^{30}_{14}	$0.39^{0.41}_{0.37}$	3.98	1.18 (175)
0.1-0.2	$12^{18}_{8.7}$	$0.31^{0.33}_{0.29}$	4.37	0.90 (192)
0.2-0.3	17^{27}_{11}	$0.28^{0.31}_{0.26}$	4.33	0.98 (194)
0.3-0.4	$12^{17}_{8.3}$	$0.34^{0.37}_{0.32}$	4.32	1.01 (196)
0.4-0.5	$13^{19}_{9.6}$	$0.37^{0.39}_{0.35}$	4.21	0.95 (203)
0.5-0.6	18^{27}_{13}	$0.33^{0.36}_{0.31}$	4.16	0.97 (200)
0.6-0.7	$10^{15}_{7.2}$	$0.33^{0.35}_{0.30}$	4.40	1.15 (201)
0.7-0.8	$9.2^{14}_{6.3}$	$0.26^{0.29}_{0.24}$	4.56	0.87 (208)
0.8-0.9	$5.9^{8.8}_{4.0}$	$0.26^{0.29}_{0.24}$	4.68	0.95 (213)
0.9-1.0	$9.7^{14}_{6.6}$	$0.34^{0.37}_{0.32}$	4.39	0.93 (182)

Table 6.3: Results from 10-bin beat phase-resolved spectral analysis of RX J1712.6-2414 during which the high bit-rate data from both SIS instruments on the *ASCA* satellite were simultaneously fitted to the reference model (Table 6.1). During the fitting only the inhomogeneous absorption parameters of the reference model were allowed to vary. The error ranges at the 90% confidence level are given for these parameters, with the χ^2_ν and observed flux (uncorrected for absorption) for the 10 phases also included.

phase	MEKAL norm: 10^{-2}	Gaussian norm: 10^{-5}	flux 2–10keV 10^{-11}erg cm^{-2} s^{-1}	χ^2_ν (dof)
0.0-0.1	$2.82^{2.90}_{2.74}$	$17.7^{23.0}_{8.93}$	3.88	1.16 (175)
0.1-0.2	$3.21^{3.29}_{3.13}$	$19.4^{25.2}_{10.5}$	4.40	0.90 (192)
0.2-0.3	$3.26^{3.35}_{3.18}$	$10.5^{14.8}_{0.56}$	4.38	0.99 (192)
0.3-0.4	$3.10^{3.18}_{3.02}$	$19.6^{24.9}_{11.3}$	4.26	1.01 (196)
0.4-0.5	$2.98^{3.06}_{2.91}$	$14.2^{18.7}_{6.26}$	4.05	0.96 (203)
0.5-0.6	$3.05^{3.12}_{2.98}$	$10.8^{16.7}_{4.94}$	4.11	0.97 (200)
0.6-0.7	$3.17^{3.25}_{3.09}$	$10.8^{15.0}_{1.85}$	4.27	1.14 (201)
0.7-0.8	$3.43^{3.51}_{3.35}$	$17.9^{23.2}_{9.42}$	4.67	0.86 (208)
0.8-0.9	$3.53^{3.62}_{3.45}$	$9.61^{17.9}_{4.29}$	4.73	0.94 (213)
0.9-1.0	$3.13^{3.24}_{3.03}$	$11.0^{14.3}_{0.00}$	4.22	0.92 (183)

Table 6.4: Results from 10-bin beat phase-resolved spectral analysis of RX J1712.6-2414 during which the high bit-rate data from both SIS instruments on the *ASCA* satellite were simultaneously fitted to the reference model (Table 6.1). During the fitting only the normalisation parameters of the reference model were allowed to vary. The error ranges at the 90% confidence level are given for these parameters, with the χ^2_ν and observed flux (uncorrected for absorption) for the 10 phases also included.

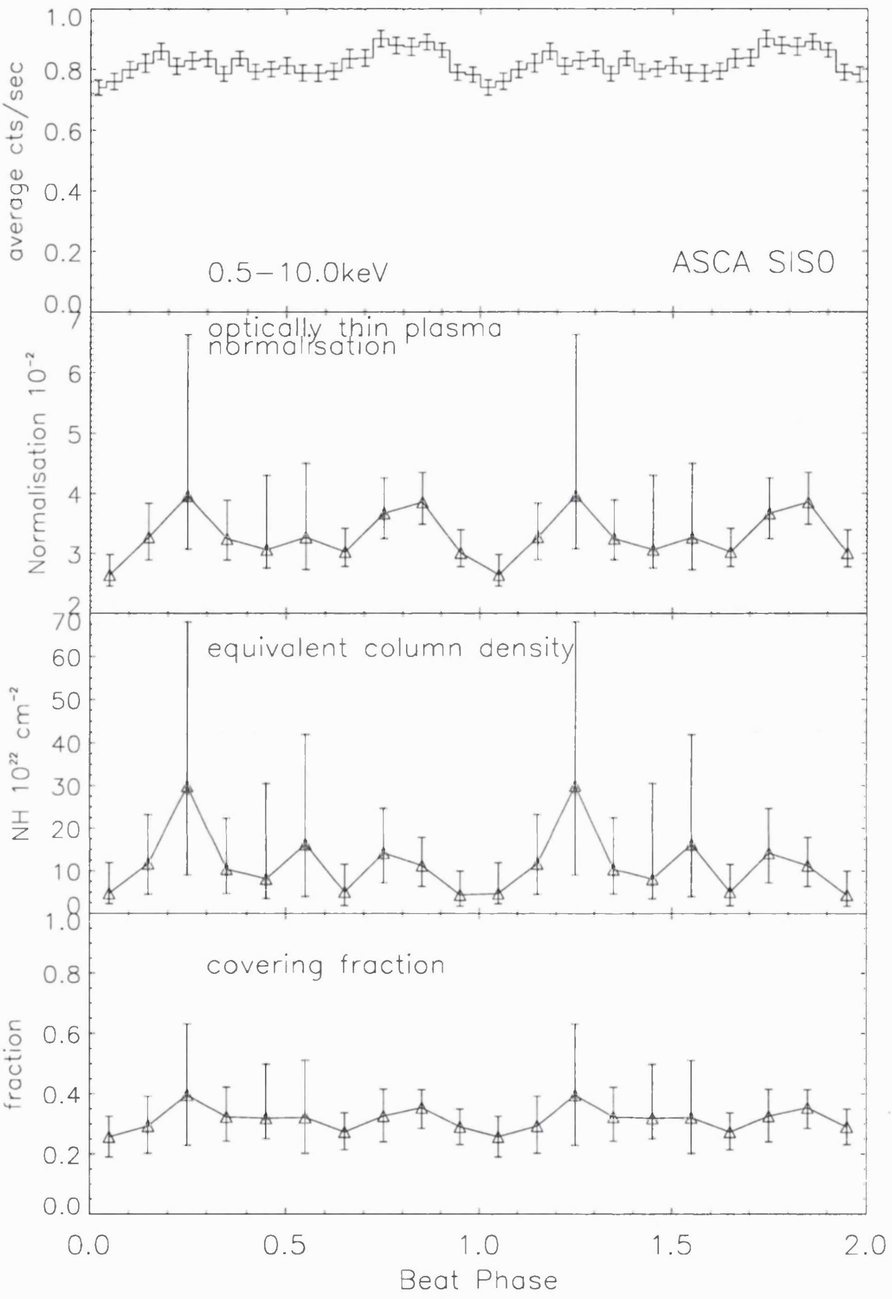

Figure 6.7: Plots of the results from phase-resolved spectroscopy of RX J1712.6-24 showing the variation in normalisation and absorption over the beat period when these parameters were varied from the reference model (Table 6.1) during the spectral fitting to the *ASCA* data. The plots from the top are the beat folded light curve of the *ASCA* data (included for clarity), the variation in the normalisation of the optically thin plasma model, the column density and the covering fraction of the partial covering absorber.

with the lack of modulation demonstrated in the hardness ratios, indicate that the most probable cause for the periodic variation in the light curves is due to differences in the visibility of optically thin hard X-ray emission over the beat period (the amplitude of which are also very small, Figure 6.2).

These results differ in several respects from those of PQ Gem (Chapter 4), despite the fact that the two objects have common properties of a relatively high magnetic field with spin modulated circular polarisation. RX J1712.6-24 shows modulation of the light curves which is more pronounced on the beat period than on the spin period (Figures 6.1 and 6.2); whereas for PQ Gem this modulation is restricted to the spin period. The cause of the beat modulation in RX J1712.6-24 may well be gating of the accretion stream between the two poles during its discless accretion (Section 2.4.1). In Section 4.4.3, the "dip" in PQ Gem is accounted for by an increase in the covering fraction of the partial covering absorber which, it is suggested, is due to the structured nature of the intercepting accretion curtain. However, there is no observational evidence for increased attenuation due to the interception of the accretion stream along the line sight in RX J1712.6-24. This variance may well be due to the different inclination of the two systems as well as to the contrast between disc and discless accretion. Certainly, the correspondence between the modulation in the 8.0–25.0keV/2.0–8keV *RXTE* hardness ratio and the covering fraction of the absorption is consistent with PQ Gem. In addition, unlike PQ Gem or V405 Aur, it was possible to constrain the upper limit of the temperature parameter for RX J1712.6-2414 during the spectral fitting, which also suggests a less complex absorption profile for this IP (Section 1.3.3). The lack of necessity for a blackbody component in the spectral analysis is consistent with the analysis of the *ROSAT* data (Section 2.4.2).

In conclusion, the light curve and spectral analysis indicate that the light curve modulation on the beat pulse for RX J1712.6-2414 is due to changing visibility of the emission region without an observable contribution from intra-system absorption.

Chapter 7

Summary and Conclusions

The results from the analysis of each of the IPs, PQ Gem, V405 Aur and RX J1712.6-2414 have been examined in the "Discussions" at the end of each analysis chapter (Sections 4.5, 5.4.1 and 6.4); in the case of PQ Gem, the main conclusions are summarized in Section 4.6. Comparison of the findings from the analyses of V405 Aur and RX J1712.6-2414 with those of PQ Gem have also been made in Sections 5.4.2 and 6.4. The reader is referred to these Sections for such assessments.

This final Chapter expands on the penultimate sentence of Section 4.6, i.e. whether a similar variation in the covering fraction of the partial absorber demonstrated in PQ Gem is to be seen in all IPs.

In the first instance, the results pertaining to this component are revisited for each object. PQ Gem showed a distinct variation in the covering fraction parameter of the partial absorber component with a well-defined maximum at phase 0.0 of the spin cycle (Figure 4.5). The 8.0–25.0keV/2.0–8.0keV hardness ratio (*RXTE*) showed a similar profile (Figure 4.3). The phase-resolved spectroscopy of V405 Aur had half the phase resolution of that carried out for PQ Gem and demonstrated a very much more marginal variation in the absorption fraction component. Two possible maxima were shown at phases 0.2–0.4 and 0.6–0.8 (Figure 5.5) and the hardness ratio (Figure 5.3) also followed a similar pattern. In the case of RX J1712.6-2414, modulation of the light curves was found on the beat period and neither the covering fraction parameter (Figure 6.7) nor the hardness ratio 8.0–25.0keV/2.0–8.0keV hardness ratio (*RXTE*, Figure 6.4) demonstrated variation over this period. V405 Aur, at phase 0.0–0.2 (Figure 5.5), was the only one of the three systems to show variation in the absorption column density.

It is obvious that the profiles of the modulation of the covering fraction in PQ Gem and V405 Aur are very different. However, the suggested accretion models are also different, i.e. accretion curtain model (tall and thin curtain) and low magnetic field/fast rotator model (wide and short curtain), respectively.

The amplitude of the modulation also varies from a maximum in PQ Gem to complete absence in RX J1712.6-2414. This could be attributed to the different geometries of the 3 systems since PQ Gem is thought to have the greatest angle of inclination at 60° and RX J1712.6-2414 the least, at $\sim 0°$. However, this latter is also thought to accrete directly from the accretion stream (discless accretion) which implies the absence of an accretion curtain. On the other hand, it would appear that the gas in the accretion curtain of PQ Gem is very inhomogeneous (Section 4.5.3). Correlation of such inhomogeneities along the accretion arc must lead to an augmentation of the amplitude of the modulation. Hence, the difference in the amplitude of the modulation may equally be a function of the degree of inhomogeneity in the accretion curtain. However, it is not possible to judge the degree of clumpiness in the accretion curtain of V405 Aur, since cyclotron modelling results are not available for this object.

The lack of modulation in the column density of PQ Gem (Figure 4.5), which has an estimated radius of the inner edge of the accretion disc, $r_A = \sim 45R_{WD}$ (Figure 1.5), and the presence of such a modulation in V405 Aur (phase 0.0–0.2) where $\mathrm{r}_A = \sim 10R_{WD}$, indicate the possibility that the column density is modulated, because of attenuation by a changing path length through relatively homogeneous material e.g. the accretion disc.

In essence, the indications are that the covering fraction of the partial absorber models the attenuation conditions of the accretion curtain of IPs reasonably well to a first order; whereas attenuation due to the accretion disc is more realistically modelled by the column density. However, the sample size of IPs investigated here is insufficient to draw firm conclusions on this, or on the relative importance of system geometry and inhomogeneities in the accretion curtain with respect to the amplitude of the modulation of the covering fraction. A much larger survey of IPs would need to be undertaken before such an assertion could be made. Nevertheless, it is reasonable to suggest, on the basis of the difference demonstrated between PQ Gem and V405 Aur, that the profile of the modulation of the covering fraction does depend on the mode of accretion of the IP in question.

Acknowledgments

First and foremost I would like to express my gratitude to Jeff who has been a real stalwart in the face of my ill-humour when the going got tough. I also appreciate the support I have received from my children, Andrew and Pauline, over many years of study and the forbearance of my grandchildren, Kei and Alex, whom I have so neglected in recent months.

I would like to thank the following people at MSSL who in one way or another have helped the wheels go round.

Prof. Keith Mason who gave me the opportunity to study here, in the first instance. My supervisor, Dr. Graziella Branduardi-Raymont, for her support and painstaking attention to detail. And to my second supervisor, Dr. Mark Cropper, for his guidance on MCVs and scientific content. Also to Gav for helpful discussions and technical know-how.

To Mat for his unstinting moral support and to Roger for the many discussions on matters photographic, both of whom have helped to keep me sane. To Encarni, Steve, Kerry, Kate, Jenni, Tracey, Lucy, Nikita, Rhaana and many others for their frienship. Not forgetting the lunchtime fun had with the small core of hardy swimmers in the MSSL pool during the summer months.

I would like to thank BT for granting me "voluntary redundancy" without which I would not have had the finances to undertake this course of study; and also the Graduate School for its financial assistance towards travel and attendance at the MCV 2nd Workshop in Annapolis, USA. My thanks also go to Paul Lamb for allowing me to help with the backups and printer support which further eased the financial situation.

References

Allan, A., Horne, K., Hellier, C., Mukai, K., Barwig, H., Bennie, P.J., Hilditch, R.W., 1996, mnras, 279, 1345.

Anzer, U., Börner, G., 1980, A&A, 83, 133.

Anzer, U., Börner, G., 1983, A&A, 203, 183.

Arnaud, K.A. 1996, in Astronomical Data Analysis Software and Systems V ASP Conference Series, Vol 101.

Arons, J., Lea, S.M., 1980, ApJ, 235, 1016.

ASCA GOF, 2000, URL http://heasarc.gsfc.nasa.gov/docs/asca/watchout.html.

Bath, G.T., Edwards, A.C., Mantle, V.J., 1983, Int. Astr. Union Colloq 72, 55.

Bevington, P.R., Robinson, D.K., 1992, Data Reduction and Error Analysis for the Physical Sciences, 2nd edition, McGraw-Hill Inc., New York.

Buckley, D.A.H., Harberl, F., Motch, C., Pollard, K., Schwarzenberg-Czerny, A., Sekiguchi, K., 1997, 287, 117.

Buckley, D.A.H., Sekiguchi, K., Motch, C., O'Donoghue, D., Chen, A.-L., Schwararzenberg-Czerny, A., Pietsch, W., Harrop-Allin, M.K., 1995, mnras, 275, 1028.

Burnard, D.J., Lea, S.M., Arons, J., 1983, ApJ, 266, 175.

Cash, J.L., Howell, S.B., Rosen, S.R., 1998, ApJ, 500, L21.

Cropper, M., 1988, mnras, 231, 597.

Cropper, M., 1989, mnras, 236, 935.

Cropper, M., 1990, Space Science Review, 54, 195.

Cropper, M., Harrop-Allin, M.K., Mason, K.O., Mittaz, J.P.D., Potter, S.B., Ramsay, G., 1998a, mnras, 293, L57.

Cropper, M., Ramsay, G., Wu, K., 1998b, mnras, 293, 222.

Cropper, M., Ramsay, G., Wu, K., 1999a, in Annapolis Workshop on Magnetic Cataclysmic

Variables ASP Conference Series, Vol 157, p. 325.

Cropper, M., Wu, K., Ramsay, G., Kocabiyik, A., 1999b, mnras, 306, 684.

Deeming, T.J., 1975, Ap & SS, 36, 137.

Done, C., Mulchaey, J.S., Arnaud, K.A., 1992, ApJ, 395, 275.

Duck, S.R., Rosen, S.R., Ponman, T.J., Norton, A.J., Watson, M.G., Mason, K.O., 1994, mnras, 271, 372.

Ezuka, H., Ishida, M., ApJS, 120, 277.

Fabian, A.C., Pringle, J.E., Rees, M.J., 1976, mnras, 173, 43.

Ferrario, L., 1996, pasa, 13, 87.

Ferrario, L., Wickramasinghe, D.T, Tuohy, I.R., 1989, ApJ, 341, 327.

Frank, J., King, A., Raine, D., 1992, Accretion Power in Astrophysics, Cambridge University Press, Cambridge.

Garlick, M.A., 1996, mnras, 279, 940.

Ghosh, P., Lamb, F., 1978, ApJ, 223, L83.

Ghosh, P., Lamb, F.K, 1979a, ApJ, 232, 259.

Ghosh, P., Lamb, F.K, 1979b, ApJ, 234, 296.

Haberl, F., Motch, C., 1995, A&A, 297, L37.

Haberl, F., Thorstensen, J.R., Motch, C., Schwarzenberg-Czerny, A., Pakull, M. Shambrook, A. Pietsch, 1994, A&A, 291, 171.

Hameury, J.-M., King, A.R., Lasota, J.-P., 1986a, 162, 71.

Hameury, J.-M., King, A.R., Lasota, J.-P., 1986b, 218, 695.

Harlaftis, E.T, Horne, K., 1999, mnras, 305, 437.

Hellier, C., 1991, mnras, 251, 693.

Hellier, C., 1997, mnras, 288, 817.

Hellier, C., Cropper, M., Mason, K.O., 1991, mnras, 248, 233.

Hellier, C., Garlick, M.A., Mason, K.O., 1993, mnras, 260, 299.

Hellier, C., Mukai, K., Beardmore, A.P., 1997, mnras, 292, 397.

Hellier, C., Ramseyer, T.F., Jablonski, F.J., 1994, mnras, 271, L25.

Hilditch, R.W., Bell, S.A., 1994, mnras, 266, 703.

Hirose, M., Osaki, Y., Mineshige, S., 1991, pasj, 43, 809.

Hoshi, R. 1973, Prog. Theor. Physics, 49, 776.

Howell, S.B., Sirk, M.M., Ramsay, G., Cropper, M., Potter, S.B., Rosen, S., 1997, ApJ, 485, 333.

Imamura, J.N., Durisen, R.H., 1983, ApJ, 268, 291.

Imamura, J.N., Durisen, R.H., Lamb, D.Q., Weast, G.J., 1987, ApJ, 313, 298.

Ishida, M., PhD Thesis, University of Tokyo, 1991.

James, C.H., Branduardi-Raymont, G., Cropper, M., Ramsay, G., 1998, in Proceedings of the First XMM Workshop, "Science with XMM", held at Noordwijk in the Netherlands, Dahlem, M. (ed.), URL http://xmm.vilspa.esa.es/news/ws1/ws1_papers.html.

James, C.H., Ramsay, G., Cropper, M., Branduardi-Raymont, G., in preparation.

King, A.R., 1995, Cape Workshop on Magnetic Cataclysmic Variables, ASP Conference Series, Vol.85.

King, A.R., Lasota, J.-P., 1991, ApJ, 378, 674.

King, A.R., Shaviv, G., 1984, mnras, 211, 883.

Kuijpers, J., Pringle, J.E., 1982, A&A, 114, L4.

Kurtz, D.W., 1985, mnras, 213, 773.

Lamb, D.Q., Masters, A.R., 1979, ApJ, 234, L117.

Lamb, D.Q., Melia, F., 1986, in The Physics of Accretion onto Compact Objects, eds Mason, K.O. et al., Springer-Verlag, Berlin, p. 113.

Lamb, D.Q., Melia, F., 1987, Ap & SS, 131, 511.

Lamb, D.Q., Melia, F., 1988, in Polarized Radiation of Circumstellar Origin, eds Coyne, G.V. et al., Obs., Vatican, Vatican, p. 45.

Lanzafame, G., Belvedere, G., Molteni, D., 1992, mnras, 258, 152.

Lanzafame, G., Belvedere, G., Molteni, D., 1993, mnras, 263, 839.

Li, J., Wickramasinghe, D.T., Rudiger, G., 1996, ApJ, 469, 765.

Liebert, J., Stockman, H.S., 1985, in Cataclysmic Variables and Low-Mass X-ray Binaries, eds. Lamb, D.Q., Patterson, J., Reidel, Dordrecht, p. 151.

Livio, M., Pringle, J.E., 1992, mnras, 259, 23.

Livio, M., Soker, N., Dgani, R., 1986, ApJ, 305, 267.

Lubow, S.H., 1989, ApJ, 340, 1064.

Lubow, S.H., Shu, F.H., 1975, ApJ, 198, 383.

Mason, K.O., 1995, Cape Workshop on Magnetic Cataclysmic Variables, ASP Conference Series, Vol. 85, p. 225.

Mason, K.O., 1997, mnras, 285, 493.

Mason, K.O., Rosen, S.R., Hellier, C., 1988, (COSPAR and IAU, Symposium on the Physics of Compact Objects, Sofia, Bulgaria, July 13-18, 1987) Advances in Space Research vol. 8, no.2–3, p. 293.

Mason, K.O., Watson, M.G., Ponman, T.J. Charles, P.A., Duck, S.R., Hassal, B.J.M., Howell, Ishda, M., Jones, D.H.P., Mittaz, J.P.D., 1992, mnras, 258, 749.

Masters, A.R., 1978, PhD Thesis, University of Illinois.

Masters, A.R., Fabian, A.C., Pringle, J.E., Rees, M.J., 1977, mnras, 178, 501.

Meggitt, S.M.A., Wickramasinghe, D.T., 1982, mnras, 198, 71.

Mewe, R., Kaastra, J.S., Liedahl, D.A. 1995, Legacy, 6, 16.

Milgrom, M., Salpeter, E.E., 1975, ApJ, 196, 583.

Mukai, K., 1988, mnras, 232, 175.

Naurenberg, M., 1972, ApJ, 175, 417.

Norton, A.J., 1993, mnras, 265, 316.

Norton, A.J., Beardmore, A.P., Allan, A., Hellier, C., 1999, A&A, 347, 203.

Norton, A.J., Watson, M.G., 1989, mnras, 237, 853.

Osborne, J.P., mmsai, 59, 117.

Patterson, J., 1994, pasp, 106, 209.

Piirola, V., Hakala, P., Coyne, G.V., 1993, ApJ, 410, L107.

Potter, S.B., Cropper, M., Mason, K.O., Hough, J.H., Bailey, J.A., 1997, mnras, 285, 82.

Pringle, J.E., 1985, in Interacting Binaries, eds. Pringle, J.E., Wade, R.A., Cambridge Universty Press, Cambridge, p. 1.

Ramsay, G., 2000, mnras, 314, 403.

Ramsay, G., Cropper, M., Hellier, C., Wu, K., 1998, mnras, 297, 1269.

Ramsay, G., Cropper, M., Wu, K., Mason, K.O., Hakala, P., 2000, mnras, 311, 75.

Ramsay, G., Mason, K.O., Cropper, M., Watson, M.G., Clayton, K.L., 1994, mnras, 270, 692.

Rosen, S.R., Mittaz, J.P.D., Hakala, P.J., 1993, mnras, 264, 171.

Rosen, S.R., Mason, K. O., Cordova, F. A., 1988, 231, 549.

Rozyczka, M., Schwarzenberg-Czerny, A., 1987, Acta Astronomica, 37, 141.

Rozyczka, M., 1988, Acta Astronomica, 38, 175.

Ryter, C., Cesarsky, C.J., Audouze, J., 1975, ApJ, 198, 103.

Scargle, J.D., 1982, ApJ, 263, 835.

Schneider, D.P., Young, P., 1980a, mnras, 238, 946.

Schneider, D.P., Young, P., 1980b, mnras, 240, 871.

Shakhovskoj, N.M., Kolesnikov, S.V., IAU Circ., 6760, 1 (1997). (Ed.) Green, D.W.E.

Shakura, N.I., Sunyaev, R.A., 1973, A&A, 24, 337.

Spruit, H.C., Taam, R.E., 1990, A&A, 229, 475.

Spruit, H.C., Taam, R.E., 1993, ApJ, 402, 593.

Stavroyiannopoulos, D., Rosen, S.R., Watson, M.G., Mason, K.O., Howell, S.B., 1997, mnras, 288, 891.

Still, M.D., Duck, S.R., Marsh, T.R., 1998, mnras, 299, 759.

Swank, J.H, 1998, The Active X-Ray Sky: Results from BeppoSAX and RXTE. Proceedings of the Active X-ray Sky symposium, 21–24 October, 1997, Rome, Italy, Edited by L. Scarsi, H. Bradt, P. Giommi, and F. Fiore.

Tanaka, Y., Inoue, H., Holt, S.S., 1994, pasj, 46, L37.

Väth, 1997, A&A, 317, 476.

Väth, H., Chanmugam G., Frank, J., 1996, ApJ, 457, 407.

Warner, B., 1995, in Cataclysmic Variables, Cambridge University Press, Cambridge.

Watson, M.G., 1986, Physics of Accretion onto Compact Objects, Springer-Verlag, Berlin, p. 97.

West, S.C. Berriman, G., Schmidt, G.D., 1987, ApJ, 322, L35.

Wickramasinghe, D.T., 1988, Polarized Radiation of Cirmstellar Origin, eds Coyne, G.V. et al. Obs., Vatican, Vatican. p. 1.

Wickramasinghe, D.T., Meggitt, S.M.A., 1985, mnras, 214, 605.

Wickramasinghe, D.T., Wu, K., Ferrario L., 1991 mnras 249, 460.

Williams, G.A., King, A.R., Brooker, J.R.E., mnras, 1987, 266, 725.

Wu, K., Chanmugam, G., Shaviv, G., 1994, ApJ, 426, 664.

Wu, K., Chanmugam, G., Shaviv, G., 1995, ApJ, 455, 260.

Wynn, G.A., King, A.R., 1992, mnras, 255, 83.

Yaqoob, T., ASCATEAM, 2000, ASCA GOF Calibration Memo, ASCA-CAL-00-06-01, v1.0 (06/05/00).

Zdziarski, A.A., Magdziarz, P., 1996, mnras, 279, 212.

Zombeck, M.V., 1990, Handbook of Astronomy and Astrophysics, Second Edition (Cambridge, UK: Cambridge Unversity Press).